Imperial College London
Department of Aeronautics

Modelling of turbulent wakes

Georgios Rigas

October 2014

Submitted in part fulfilment of the requirements for the degree of
Doctor of Philosophy in Aeronautics of Imperial College London
and the Diploma of Imperial College London

Declaration

I herewith certify that all material in this dissertation which is not my own work has been properly acknowledged.

Georgios Rigas

Abstract

The dynamics of the turbulent three-dimensional wake generated by an axisymmetric bluff body with blunt trailing edge are experimentally and theoretically investigated at a diameter based Reynolds number of $188,000$.

A detailed analysis of the base pressure measurements shows that the large scale structures of the turbulent three-dimensional wake retain the structure of the laminar instabilities observed in the transitional regimes, in a statistical sense. These persisting instabilities at the turbulent regime, are associated with spatial and temporal symmetry breaking, giving rise to spatial reflectional symmetry and quasi-periodic vortex shedding. The influence of turbulence recovers the lost temporal and spatial symmetries in the long-time average. It is shown that the turbulent spatial dynamics are reproduced by a simple stochastic model the deterministic part of which accounts for the spatial symmetry breaking and gives rise to steady large scale structures through a supercritical pitchfork bifurcation, and the stochastic part modelling in a phenomenological sense the turbulent fluctuations acting on the large scale structures.

The axisymmetric body wake is further investigated when axisymmetric slot-jet zero-net-mass-flux forcing is applied on the rear base. Landau-like models that capture the weakly nonlinear interaction between the global vortex shedding mode and axisymmetric forcing are derived from the phase-averaged Navier-Stokes equations. The Landau-like models describe accurately the forced response by means of measured base pressure of the global vortex shedding mode. With the present analysis it is demonstrated that the concept of weakly nonlinear global modes can be extended to a fully turbulent flow, far from the critical bifurcation Reynolds number, and a general framework for the description of systems with broken symmetries—giving rise to global dynamics—and turbulent dynamics is provided. The novel results presented here advance the understanding of the dynamics of three-dimensional turbulent wakes and pave the way for turbulence prediction and control.

Preface

Journal publications during the course of the work:

i) Rigas, G., Oxlade, A. R., Morgans, A. S. & Morrison, J. F. 2014 Low-dimensional dynamics of a turbulent axisymmetric wake. *J. Fluid Mech.* **755 R5**.

ii) Oxlade, A. R., Morrison, J. F., Qubain, A. & Rigas, G. 2014 High-frequency forcing of a turbulent axisymmetric wake. *Accepted, J. Fluid Mech.*

iii) Rigas, G., Morgans, A. S. & Morrison, J. F. 2014 Dynamics of the forced axisymmetric turbulent wake. *In preparation.*

iv) Rigas, G., Morgans, A. S., Brackston R. D. & Morrison, J. F. 2014 Symmetries and stochastic dynamics of three-dimensional turbulent wakes. *In preparation.*

Conference publications during the course of the work:

i) Morrison, J. F., Oxlade, A. R. & Rigas, G. 2014 Open-loop control of a turbulent axisymmetric wake. In *Proceedings of the International Conference on Instability and Control of Massively Separated Flows*.

ii) Rigas, G., Morgans, A. S. & Morrison, J. F. 2014 Stability and coherent structures in the wake of axisymmetric bluff bodies at high Reynolds numbers. In *Proceedings of the International Conference on Instability and Control of Massively Separated Flows*.

The work has been presented in:

i) Rigas, G., Morgans, A. S. & Morrison, J. F. 2014 Symmetries, multistability and stochastic dynamics of turbulent wakes. In *67th Annual Meeting of the American Physical Society's Division of Fluid Dynamics, San Francisco, USA*.

ii) Rigas, G. 2014 Symmetries and stochastic dynamics of turbulent wakes. In *12th ERCOFTAC Osborne Reynolds Research Students Award, University College London*.

iii) Rigas, G., Morgans, A. S. & Morrison, J. F. 2013 Stability and coherent structures in the wake of axisymmetric bluff bodies at high Reynolds numbers. In *International Conference on Instability and Control of Massively Separated Flows, Prato, Italy*.

iv) Rigas, G., Morgans, A. S. & Morrison, J. F. 2013 Model-based framework for feedback control in the wake of axisymmetric bluff bodies. In *10th ERCOFTAC SIG33 Workshop: Progress in Transition, Modeling and Control, Sweden*.

v) Rigas, G., Morgans, A. S. & Morrison, J. F. 2013 Dynamic modeling of a turbulent axisymmetric bluff-body wake. In *66th Annual Meeting of the American Physical Society's Division of Fluid Dynamics, Pittsburgh, USA*.

vi) Rigas, G., Morgans, A. S. & Morrison, J. F. 2012 The response of the wake past a bullet-shaped body to axisymmetric ZNMF forcing at high Reynolds numbers. In *65th Annual Meeting of the American Physical Society's Division of Fluid Dynamics, San Diego, USA*.

Acknowledgements

First and foremost I am grateful to my supervisor Dr. Aimee Morgans and my co-supervisor Prof. Jonathan Morrison for giving me the opportunity to work on this subject. Their guidance, patience and mentoring were more than generous during my PhD. I consider myself incredibly lucky to have such outstanding supervisors.

I extend my gratitude to my exceptional colleagues in the Aeronautics department. In particular I would like to thank Dr. Anthony Oxlade, who supported me from my very first day at Imperial College and introduced me to the subject, designed the flawless axisymmetric bluff body used in this study and shared valuable experimental expertise with me. Furthermore, I specially thank Dr. Marcos Garcia de La Cruz Lopez and Rowan Brackston for numerous technical discussions.

Finally I would like to thank my parents for their support all these years, without which I would not be where I am now. Financial support from the EPSRC is also gratefully acknowledged.

Nomenclature

Acronyms

A/D	Analog-to-digital
CoP	Centre of pressure
CTA	Constant-temperature anemometry
D/A	Digital-to-analog
DNS	Direct numerical simulation
GLSA	Global linear stability analysis
LLSA	Local linear stability analysis
MM	Mixed mode
MSD	Mean square displacement
PDF	Probability density function
PID	Proportional-integral-derivative
PSD	Power spectral density
PSI	Parametric subharmonic instability
POD	Proper orthogonal decomposition
RMS	Root-mean-square
SS	Steady state
SW	Standing wave
VLF	Very low frequency

VS	Vortex shedding	
ZNMF	Zero-net-mass-flux	

Greek symbols

∇	Laplace operator	
ξ	Random forcing term	
ν	Kinematic viscosity	$\mathrm{m^2\,s^{-1}}$
ν_T	Eddy turbulent viscosity	$\mathrm{m^2\,s^{-1}}$
ω	Angular frequency	$\mathrm{rad\,s^{-1}}$
ϕ	Angle in the polar co-ordinate system	degrees
ρ	Fluid density	$\mathrm{kg\,m^{-3}}$
σ	Standard deviation	
θ	Momentum thickness of boundary layer at separation	m

Roman symbols

A	Amplitude of global mode	
C_p	Area weighted pressure coefficient	
D	Diameter of the body	m
D	Diffusion coefficient	
E	Forcing amplitude	
e	Euler's number	
f	Frequency	$\mathrm{s^{-1}}$
i_{in}	Actuator driving current	
L	Length of the body	m
p	Pressure	$\mathrm{kg\,m^{-1}\,s^{-2}}$

p_{cav}	Actuator cavity pressure	$\mathrm{kg\,m^{-1}\,s^{-2}}$
P_m	Modal pressure amplitude	
r	Radius or radial position in the polar/cylindrical co-ordinate system	m
Re_D	Reynolds number based on body diameter	
St	Strouhal number	
$\mathbf{u}$	Velocity components	
U_∞	Freestream velocity	$\mathrm{m\,s^{-1}}$
u_{jet}	Actuator centreline jet velocity	$\mathrm{m\,s^{-1}}$
v_{in}	Actuator driving voltage	
x, y, z	Cartesian co-ordinate system	m
z	Axial position in the cylindrical co-ordinate system	m

Contents

List of Figures

List of Tables

1. Introduction

Turbulent flows are ubiquitous in natural phenomena and engineering applications therefore a mathematically tractable description of them is desirable for their prediction and control. At low Reynolds numbers, corresponding to laminar regimes, hydrodynamic stability and bifurcation theory have aided understanding of the dynamic behaviour of fluid flows. However, departure from the laminar regimes and the critical bifurcating points renders the flow chaotic and finally turbulent, increasing the order of the system and complexity for a mathematical description of it.

In this thesis we focus on flows behind bluff bodies. Bluff-body flows are of fundamental importance to many industries, in particular the transport industry, where the aerodynamic drag arising from such flows can be the dominant source of vehicle fuel-burn and CO_2 emissions (Hucho, 1998). However, flows pertinent to the transport industry involve high Reynolds numbers and turbulent wakes. Despite their turbulence, such wake flows exhibit organisation which manifests as coherent flow structures: these are usually associated with increased noise, structural fatigue and drag. Understanding the underlying wake dynamics in the turbulent regime is of paramount importance for the development of practical control strategies.

This investigation is part of a broader research effort to develop flow control devices that can be deployed on automotive vehicles. Previous work at Imperial College has addressed this challenge through open loop forcing of the wake of an axisymmetric bluff body with a blunt trailing edge, achieving base pressure increases of up to 33% using a pulsed jet (Qubain, 2009; Oxlade, 2013; Oxlade *et al.*, 2014). The question that still remains unanswered is *'can we achieve more efficient turbulence control using feedback control techniques?'*. To answer this question a deep understanding of the underlying turbulent dynamics is required. This understanding can enable the development of mathematical models, based upon which control algorithms can be designed and implemented in turbulent fluid-flow systems with the end goal being the manipulation of these flows at will.

The aim of this thesis is the analysis and modelling of the dynamic behaviour of a turbulent wake behind a bluff three-dimensional axisymmetric body with a blunt trailing edge. We will show, perhaps surprisingly given that $Re_D \sim 2 \times 10^5$, that these dynamics can in fact be linked to the hydrodynamic instabilities observed during the transitional regimes at low Reynolds numbers. Here, $Re_D = U_\infty D/\nu$ is the Reynolds number, U_∞ is the free-stream velocity, D is the diameter of the body and ν is the fluid kinematic viscosity. These observations allow us to develop simple and tractable mathematical models that capture most of the dynamic behaviour of turbulent wakes by extending well-known theories of the laminar flow to the turbulent one.

An important feature of our study is the use of only body-mounted sensing. In real transport flows, full flow-field measurements are impractical, with sensors embedded in/attached to the body being the only feasible option. In the context of drag reduction, only those structures which influence the pressure force on the base of the bluff-body are of importance. We therefore conduct our analysis entirely using pressure measurements on the base of the body.

1.1. Why low dimensional space?

An important theme of this work is that the dynamics of turbulent flows, which span a high-dimensional space, may frequently be captured accurately and efficiently by projection onto a low-dimensional space. To enhance understanding of why this is the case, we begin with the governing equations, taken to be the scaled incompressible Navier-Stokes equations:

$$\partial_t \mathbf{u} + \mathbf{u} \cdot \nabla \mathbf{u} = -\nabla p + \mathrm{Re}^{-1} \nabla^2 \mathbf{u} \quad \text{and} \quad \nabla \cdot \mathbf{u} = 0. \tag{1.1}$$

One can expand the solution of (1.1) as an infinite sum of basis functions that satisfy the boundary conditions, say $\phi_n(\mathbf{x})$. Physically, these typically represent the modes of the flow, each with amplitude A_n,

$$q(\mathbf{x}, t) = \sum_{n=0}^{\infty} A_n(t) \phi_n(\mathbf{x}). \tag{1.2}$$

Upon substitution in (1.1), a set of ordinary differential equations for the amplitudes A_n is obtained:

$$\frac{d\mathbf{A}}{dt} = F(\mathbf{A}). \tag{1.3}$$

Note that this is an infinite-dimensional description, while experimental observations suggest that many flows, including the flows behind bluff bodies, are dominated by small number of modes.

Quite generally, (1.3) can be written as

$$\frac{d\mathbf{A}}{dt} = L\mathbf{A} + N(\mathbf{A}), \tag{1.4}$$

where L is a linear operator and N is the nonlinear part. For small deviations from the steady state, the nonlinear part can be neglected. In a stable stationary state all these states (or modes) are stable in the sense that perturbations off the stationary state decay in time. Then stability implies that all the eigenvalues λ_i of the linear operator L are lying in the left half complex plane (negative real part), since any solution of a linear equation can be expanded in eigenmodes whose time dependence is $e^{\lambda t}$. A mode becomes unstable if it is associated with an eigenvalue that crosses the imaginary axis gaining a positive real part. When a control parameter is changed (in bluff-body flows typical control parameter is the Reynolds number, in the absence of forcing) at a critical value it often happens that at least one eigenvalue crosses the imaginary axis. Whenever this situation occurs, the dynamics can be effectively reduced to a set of differential equations, where the number of variables involved is determined by the number of the unstable modes. Intuitively, the reason for this reduction is a simple separation of timescale. Modes that have just crossed the imaginary axis have a small real part and are evolving on long timescales. All the other modes rapidly adapt themselves to the slow modes (Procaccia, 1988).

Historically the first dynamical systems description of turbulent flows introducing the concept of transition was given by Landau (Landau, 1944; Landau & Lifshitz, 1959). In his conceptual model, turbulence may be produced via an infinite number of oscillatory bifurcations as the Reynolds number of the flow is increased giving rise to a continuous spectrum of temporal frequencies. Ruelle & Takens (1971) revised Landau's theory and showed that chaotic behaviour can be reached only after a finite and small number of bifurcations.

Based on the above, before reaching fully developed turbulence many flows, i.e. bluff-body wakes, pass through an intermediate state in which the time dependence of their state variables is already erratic but only a few modes are appreciably excited. Such a system can be successfully described by mathematical models involving a finite, and even small, number of dynamic variables. In our study, we show that these modes persist even at high Reynolds numbers, manifesting as large-scale coherent structures, and containing most of the dynamic behaviour observed in the near wake behind a bluff body.

1.1.1. Global modes

At low Reynolds numbers, many flows are able to sustain a stable stationary state when perturbed. With increasing Reynolds number, such flows may undergo a change in stability that affects the whole flow field, at a critical Reynolds number, Re_c. The flow is then globally unstable. This change in stability is termed a bifurcation, with Reynolds number being the bifurcation parameter.

Linear stability analysis may be employed to predict accurately the onset of instability in transitional flows. This is accomplished by studying the evolution of perturbations on the fixed point of the governing Navier-Stokes equations (steady equilibrium known as *base-flow*). Specifically, perturbations will grow exponentially, if there exists one unstable eigenvalue associated with the linearised governing equations around the base-flow. Then the flow under investigation is termed linearly and globally unstable.

Flows which exhibit a global instability are known as oscillator flows (Huerre & Monkewitz, 1990; Chomaz, 2005), and bluff-body wake flows are an example. The periodic vortex shedding into the wake of a circular cylinder is one of the most well-known examples of a global fluid instability in an open flow. Such flows initially exhibit a single unstable eigenmode and are linearly unstable. The modal amplitude initially grows exponentially, but is then limited by non-linear effects and settles into limit cycle. This type of bifurcation is known as a supercritical Hopf bifurcation.

The evolution of the amplitude of the global mode with time, starting from the exponential growth characterised by linear instability, and progressing to the non-linear saturation characterised by a stable limit cycle, can be modelled using the Stuart-Landau equation. The Stuart-Landau equation describing the weakly nonlinear evolution of the amplitude A of the global eigenmode close to the threshold of bifurcation ($\varepsilon = Re_c^{-1} - Re^{-1} \ll 1$) is given by

$$\frac{dA}{dt} = \sigma A + \lambda A|A^2|. \tag{1.5}$$

The Stuart Landau equation has been widely used to predict the oscillation amplitude of a flow undergoing single supercritical Hopf bifurcation, such as a cylinder flow (Sipp & Lebedev, 2007). It has to be pointed out that the SL has been successfully used to describe also local flow quantities, i.e. velocity component at a fixed spatial point, and in this case the two unknown complex coefficients can be found experimentally (Provansal *et al.*, 1987; Schumm *et al.*, 1994) or numerically (Dušek *et al.*, 1994) from transient experiments close to the threshold of bifurcation. More recently, coupled Stuart-Landau equations have been shown to apply to more complicated flows in which multiple unstable modes exist and interact. These include flows generatated by three-dimensional axisymmetric bluff bodies such as the disk and the sphere (Fabre *et al.*, 2008; Meliga *et al.*, 2009).

It should be emphasised that the weakly nonlinear analysis is not only relevant to understand the transition process, but also describes the evolution of the whole flow-field during the saturated nonlinear regime. Thus far, modelling of three-dimensional bluff-body flows using the Stuart Landau equations has been limited to laminar, low Reynolds number flows, in which the Reynolds number is close to Re_c. It has not been applied to fully turbulent flow.

1.2. Axisymmetric bluff body wakes

Axisymmetric bluff body wakes are of practical interest since they serve as a generic representation of three-dimensional flows commonly found in engineering applications. These wakes have been widely studied though laboratory and numerical experiments, with the majority of attention focussed on spheres and disks. Another type of axisymmetric body, the bullet-shaped body (typically a cylindrical body with an ellipsoid nose and its axis aligned with the flow) has received considerable attention recently. This type of body has an additional control parameter, the length of the body L, with facilitates control of the boundary layer characteristics—at the fixed separation that occurs at the trailing edge—through its development length. Also, for a fixed L the properties of the boundary layer can be controlled with appropriated conditioning of it (i.e. laminar or turbulent separation). Recent advances in computing power have enabled the study of bluff body flows with direct numerical simulations. However, due to the high computational cost, DNS are limited to low Reynolds numbers, corresponding to transitional and laminar regimes.

1.2.1. Laminar/transitional regime

It has been generally acknowledged that the flow behind axisymmetric bodies is dominated an instability with azimuthal wavenumber $|m| = 1$ (Monkewitz, 1988), which plays an important role during the transition of the laminar wake. Studies based on experimental measurements and direct numerical simulations showed that the wake undergoes successive bifurcations at low Reynolds numbers from an axisymmetric steady state. The results of these studies are summarised in the following sections and a clear understanding of the dynamics of the laminar wake will provide additional insight in the turbulent ones.

Bullet shaped body

The flow past blunt-based axisymmetric bluff bodies has been considered in various direct numerical simulations (Sanmiguel-Rojas *et al.*, 2011; Bohorquez *et al.*, 2011; Bury & Jardin, 2012) and local/global linear stability analyses (Sevilla & Martínez-Bazán, 2004; Sanmiguel-Rojas *et al.*, 2009, 2011; Bohorquez *et al.*, 2011) with or without control. The key characteristics and parameters of these studies are shown in table 1.1. These numerical studies showed that, before the emergence of chaos in the near wake, the flow undergoes two successive bifurcations by increasing the diameter based Reynolds number in the absence of external forcing. These bifurcations are associated with loss of spatial and temporal symmetries, respectively.

Linearly stable flow For axisymmetric bodies in a uniform external flow, the steady separated flow field at low Re consists of an axisymmetric, steady, toroidal recirculation eddy behind the body. In terms of stability the axisymmetric base flow is linearly stable and any small perturbation on this will decay in time. The base flow, which coincides with the mean flow, is rotationally symmetric with respect to the axis of the body (axisymmetric).

	Re	L/D	Analysis	Control
Sevilla & Martínez-Bazán (2004)	3000	9.8	LLSA	base bleed
Sanmiguel-Rojas *et al.* (2009)	≤ 2200	5	GLSA	base bleed
Sanmiguel-Rojas *et al.* (2011)	≤ 700	2	DNS, GLSA	base cavity
Bohorquez *et al.* (2011)	≤ 2000	2	DNS, GLSA	base bleed
Bury & Jardin (2012)	≤ 900	7	DNS	

Table 1.1.: Short survey of numerical investigations of flows behind axisymmetric bodies with blunt trailing edge (bullet shaped bodies).

First bifurcation (steady) The first bifurcation observed in axisymmetric bluff-body wakes is a supercritical steady* one with azimuthal wavenumber $m = 1$ which leads to a double-threaded wake structure; although the flow is still steady, it is no longer axisymmetric but preserves reflectional symmetry about a fixed plane that passes along the axis of the body. Figure 1.1a illustrates that the streamwise vortices behind the bullet shaped body are not aligned with the streamwise direction but exhibit a large eccentricity which becomes more pronounced further downstream of the solid base. The angle of the reflection symmetry plane is determined by the initial conditions. The resulting flow has reduced symmetry due to the loss of stability through the supercritical and steady bifurcation: the rotational symmetry has been replaced by reflectional symmetry.

Second bifurcation (unsteady) For larger Reynolds numbers, a Hopf bifurcation with $m = \pm 1$ leads to unsteady flow characterised by the shedding of streamwise-oriented, alternating hairpin-like vortices. Vorticity contours shown in figure 1.1b provide a clear picture for the structure of the wake where regularly spaced vorticity lobes are shed periodically. The non-dimensional Strouhal frequency is approximately 0.12. At this regime, the flow preserves the reflectional symmetry and vortices are shed eccentrically of the body axis.

The thresholds of the two bifurcations described above depend on the length-to-diameter ratio of the body, L/D. For a body with $L/D = 7$, these regimes were observed at Reynolds numbers close to 450 and 590 (Bury & Jardin, 2012). For a body with a smaller length-to-diameter ratio, $L/D = 2$, the critical Reynolds numbers are 319 and 413 (Bohorquez *et al.*, 2011).

*the frequency of the unstable eigenvalue is zero

Chaotic regime Further departure from the second critical Reynolds number renders the wake chaotic. During the chaotic regime the reflectional symmetry is broken; however, phases of reflectional symmetry whose flow topology resembles that of the reflectional symmetric state are randomly interrupted by dramatic changes of the azimuthal position of the symmetry plane (Bury & Jardin, 2012), as depicted in figure 1.1c. The reflectional symmetry plane exists in an instantaneous sense, but it is randomly and intermittently re-oriented on a very long time scale.

Beyond the second critical Reynolds number, Bury & Jardin (2012) identified a second mode with a frequency lower than the natural shedding frequency and which dominates the drag fluctuations. Bohorquez *et al.* (2011) also reported a second peak appearing in the spectra of the axial velocity component at a frequency approximately one quarter of the shedding. However, no analysis of this observation was given.

Disk and sphere

Similar regimes and bifurcations to the ones described above for the bullet shaped body have been observed mainly through direct numerical simulations in the wake behind a sphere (Tomboulides & Orszag, 2000; Ghidersa & Dušek, 2000; Pier, 2008; Fabre *et al.*, 2008). A steady bifurcation of the $m = 1$ mode at $Re \approx 210$ is responsible for the loss of rotational symmetry (axisymmetry). The resulting wake is characterised by a pair of opposite-sign streamwise vortices which exhibit reflectional symmetry. A second oscillatory bifurcation with $m = \pm 1$ is observed at $Re \approx 270$ and results in periodic vortex shedding. Ormières & Provansal (1999) showed experimentally that the periodic regime, which appears after the transition from steady to unsteady wake, follows a Landau-Hopf scenario. The critical Reynolds number for the onset of periodic velocity oscillations on the wake was found to be 280, which is in close agreement with the above studies. After the second Hopf bifurcation the wake preserves the reflectional symmetry. However, for further departure ($Re \approx 500$) from the second critical Re, the flow becomes chaotic and vortices are shed from the sphere with random orientation. At $Re \approx 1000$ small scale structures appear in the flow because of the Kelvin-Helmholtz instability of the separating shear layer from the sphere (Tomboulides & Orszag, 2000).

The flow behind a disk placed normal to the flow (Natarajan & Acrivos,

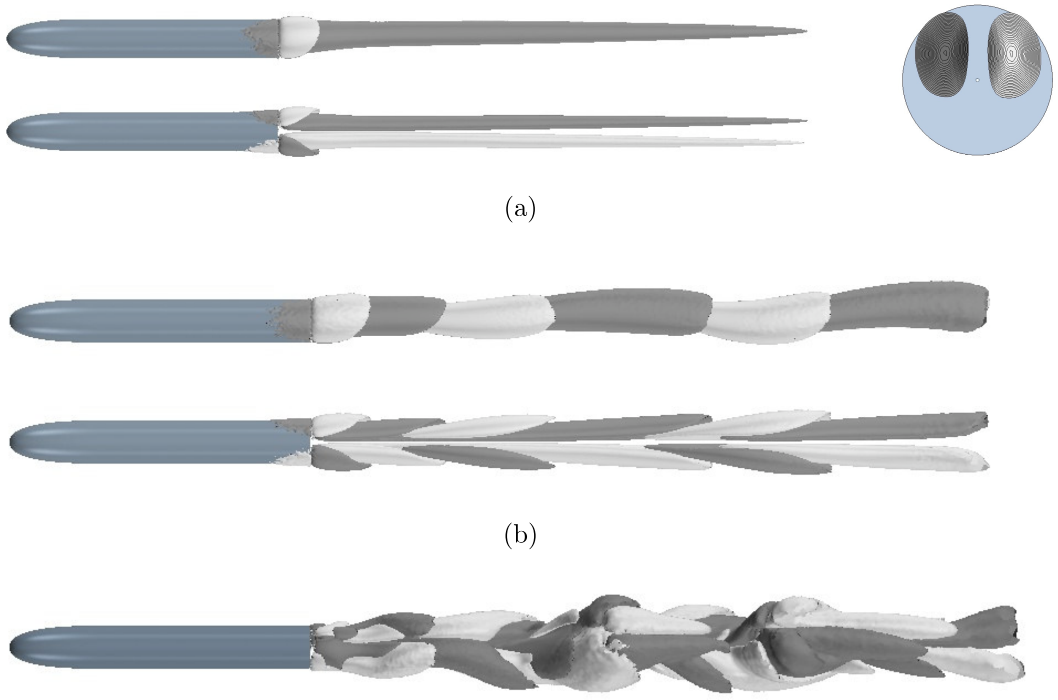

(a)

(b)

(c)

Figure 1.1.: Streamwise vorticity contous behind a bullet shaped axisymmetric bluff body at different regimes and low Reynolds numbers. (a) Left: lower and side view of vorticity iso-surfaces immediately after the first steady bifurcation, $Re = 550$. Right: isolines of vorticity at a location of 14 diameters downstream of the solid base. This regime is characterised by spatial reflectional symmetry due to loss of rotational symmetry. (b) Lower and side view of vorticity iso-surfaces immediately after the second unsteady bifurcation, $Re = 700$. This regime is characterised by loss of temporal symmetry and the emergence of vortex shedding. (c) Side view of vorticity iso-surfaces during the chaotic regime, $Re = 900$. Although this regime is characterised by chaotic dynamics, structures that resemble the ones at earlier stages are distinguishable. After Bury & Jardin (2012).

1993; Fabre *et al.*, 2008; Meliga *et al.*, 2009) shows a slightly different picture. As for the sphere and the bullet shaped body, the first $m = 1$ bifurcation observed at $Re \approx 115$ leads to a steady mode with reflectional symmetry and a subsequent oscillatory one at $Re \approx 121$ to periodic shedding. However, the latter breaks the reflectional symmetry and the vortices appear to be twisted about the disk axis, with no symmetry plane due to the regular rotation of the separated region. Finally, at $Re \approx 140$ a third bifurcation recovers reflectional symmetry and vortices are shed at a constant angle. Similarly to the sphere and the bullet shaped body, for sufficiently high Re, the flow becomes chaotic and no other bifurcation is observed.

1.2.2. Weakly nonlinear modelling

The observations presented above suggest that the transitional behaviour of axisymmetric wakes follows a similar scenario during the initial stages at low Reynolds numbers of $\mathcal{O}(100)$. Using hydrodynamic stability arguments, these studies shed light on the transitional dynamics of axisymmetric wake flows and paved the way to low-order dynamical modelling that captures accurately their transitional dynamics close to the threshold of bifurcations.

Linear stability analysis has been proved to predict accurately the onset of instability for each bifurcated regime for many of the above studies. However, the instabilities grow over time and the underlying small amplitude assumption of the linear stability analysis is no longer valid. Thus, as the flow evolves in time, higher than first order terms (linear) become important and a nonlinear analysis is necessary. Fabre *et al.* (2008), based on symmetry arguments (symmetry group $O(2)$ of the problem), used the normal form of equations truncated at third order which describes the interaction of the three global modes (steady $m = 1$, unsteady $m = \pm 1$) in the wake of a sphere and a disk. Their model, which was initially developed for the Taylor-Couette system, allowed them to explain structural differences observed in the disk and sphere flows and to accurately predict the evolution of lift force. Meliga *et al.* (2009) used a multiple time scale expansion to compute analytically the leading-order equations that describe the nonlinear interaction of the three leading eigenmodes in the wake of a disk. The normal form, which was identical to the normal form proposed by Fabre *et al.* (2008), accurately predicted the sequence of bifurcations, the associated thresholds and symmetry properties observed in the DNS calculations.

For the laminar case, the three leading eigenmodes that are linearly unstable and responsible for the two consecutive bifurcations in axisymmetric body flows are an $m = 1$ stationary mode and $m = \pm 1$ spinning modes. The weakly nonlinear anlysis involves expansion of the three dimensional velocity field and the pressure field $\mathbf{q} = (\mathbf{u}, p)^T$ of the scaled Navier-Stokes equations considering the following asymptotic expansion of the flowfield:

$$\mathbf{q}(\mathbf{x}, t, t1) = \mathbf{q}_0(\mathbf{x}) + \sqrt{\varepsilon}^1 \mathbf{q}_1(\mathbf{x}, t, t1) + \sqrt{\varepsilon}^2 \mathbf{q}_2(\mathbf{x}, t, t1) + \sqrt{\varepsilon}^3 \mathbf{q}_3(\mathbf{x}, t, t1) + \cdots \quad (1.6)$$

Introducing (1.6) into (1.1) and considering departure of order ε from criticality ($Re^{-1} = Re_c^{-1} - \varepsilon$, $\varepsilon \ll 1$), a series of equations is obtained at various orders equating coefficients of the nth power of $\sqrt{\varepsilon}$ to zero. Specifically:

(i) At zero order, a nonlinear equation is obtained specifying that $\mathbf{q}_0$ is a solution of the steady Navier-Stokes equations at the critical Reynolds number, Re_c.

(ii) At first order, an eigenvalue problem is obtained specifying that $\mathbf{q}_1$ may be taken as a superposition of the unstable global modes of the steady flow field $\mathbf{q}_0$:

$$\mathbf{q_1} = A_1 e^{im\phi} + \left(B_{+1} e^{im\phi} + B_{-1} e^{-im\phi}\right) e^{\omega_0 t} + c.c. \quad (1.7)$$

where A_1 is the complex amplitude of the stationary mode and $B_{\pm 1}$ are the amplitudes of the two counter-rotating oscillating modes.

(iii) At second order, inhomogeneous linear non-degenarate equations are obtained which can be readily solved.

(iv) At third order, degenerate linear inhomogeneous equations arise. Hence, compatibility equations are imposed to cancel secular terms which yield coupled Landau-like equations, describing the amplitude evolution of the unstable global modes. More details for the analysis can be found in Meliga *et al.* (2009). The Landau equations that arise are:

$$\dot{A}_1 = A_1 \left(\lambda_A + a_0|A_1|^2 + b_A|B_{+1}|^2 + c_A|B_{-1}|^2\right) + d_A B_{+1} B_{-1}^* A_1^* \quad (1.8a)$$

$$\dot{B}_{+1} = B_{+1} \left(\lambda_B + a_B|A_1|^2 + b_B|B_{+1}|^2 + c_B|B_{-1}|^2\right) + d_B A_1^2 B_{-1} \quad (1.8b)$$

$$\dot{B}_{-1} = B_{-1} \left(\lambda_B + a_B|A_1|^2 + b_B|B_{-1}|^2 + c_B|B_{+1}|^2\right) + d_B A_1^{*2} B_{+1} \quad (1.8c)$$

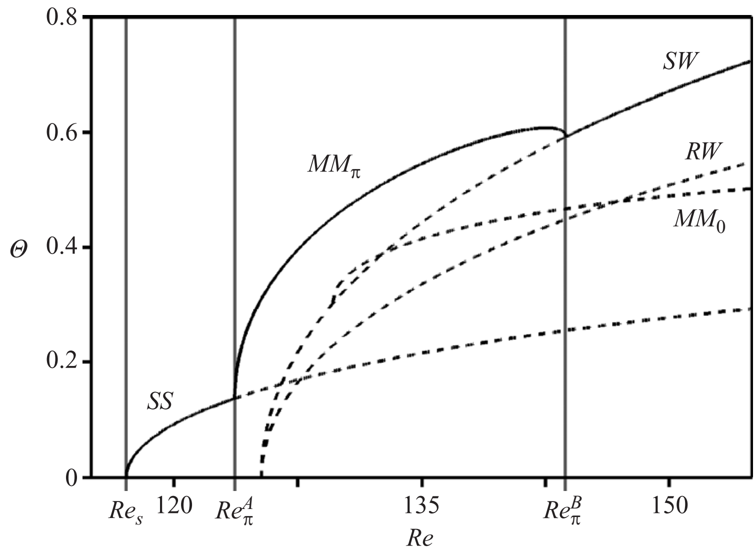

Figure 1.2.: Theoretical bifurcation diagram of the wake of a circular disk associated to the normal form (1.8). The sum of the amplitude of the three global modes is plotted, $\Theta = |A_1| + |B_{+1}| + |B_{-1}|$ as a function of the Reynolds number. Solid (respectively dashed) lines denote stable (respectively unstable) branches. After Meliga *et al.* (2009).

The bifurcation diagram predicted by eq. (1.8) for the disk flow is shown in figure 1.2, where the sum of the amplitude of the three complex modes is plotted. Depending on the values of the coefficients of eq. (1.8), different branches in the bifurcation diagram are selected. This appears to be the case for the sphere explaining the different transition scenario; the mixed mode branches (MM) are unstable and the standing wave (SW) solution is selected after the steady state (SS) solution.

Although the weakly nonlinear analysis has been applied for the disk and sphere wakes in the case of three-dimensional bluff body flows, one could expect the same equations to hold for the bullet shaped body. As the DNS and linear global stabilty results suggest, the transition is similar in these flows, and specifically with the sphere wake.

Recently, the weakly nonlinear analysis was extended by Sipp (2012) taking into account external forcing. The modelling approach was demonstrated on a two-dimensional laminar open-cavity flow which is characterised by a single global oscillatory mode. The derived Landau-like equations included extra terms that arise due to the forcing and predicted accurately the response of the global mode when forcing was applied. It was demonstrated that the global mode could be effectively suppressed with high-frequency forcing or locked on the forcing frequency opening new horizons for open loop control in flows with global modes. It follows naturally that this approach should be applicable on flows with more than one unstable modes, such as axisymmetric bluff body flows, however resulting in more complex equations and more terms due to the combinations of all the possible interactions.

1.2.3. Turbulent regime

A large number of studies has shown that at high Reynolds numbers, the bifurcating oscillatory state observed in the laminar wakes manifests as shedding of large-scale structures. Due to the high computational requirements of DNS of the governing Navier-Stokes equations at high Reynolds numbers, much reliance is still placed on experimentation. Early experiments in the turbulent wake behind axisymmetric bodies, such as disks and spheres, (Achenbach, 1974; Taneda, 1978; Fuchs *et al.*, 1979) showed that the predominant flow structures in the near wake are coherent antisymmetric modes with $|m| = 1$. Visualisations and velocity measurements in the near wake of axisymmetric bodies indicated that these structures are shed in the form of one helix or a pair of counter-rotatating vortices at a constant Strouhal frequency, independent of Reynolds number. Interestingly, the above studies of turbulent wakes showed that the separation point rotates randomly around the body above Reynolds number 1000, approximately. In recent experiments behind blunt-based axisymmetric bodies, Sevilla & Martínez-Bazán (2004) and Grandemange *et al.* (2012*b*) measured a dominant oscillatory antisymmetric mode with $|m| = 1$ at a Strouhal frequency of $St \approx 0.2$.

Using hot-wire measurements, Kim & Durbin (1988) found in the near wake of a sphere two dominant frequencies over a broad range of Re ($500 \leq Re \leq 60000$). The low frequency corresponded to the vortex shedding and remained approximately constant over the Re range they examined, when non-dimensionalised with the diameter of the sphere and the freestream velocity. The high frequency was associated with the separating shear layer instability and they were able to measure it only in the immediate wake. As in the laminar case, the turbulent shear layer acts as an amplifier of disturbances over a relatively broad range of wavenumbers. In the immediate wake the most amplified frequency scales with the momentum thickness of the boundary layer and the most amplified frequency is $St_\theta \approx 0.016$ if the shear layer is laminar, or $St_\theta \approx 0.022 - 0.024$ if the shear layer is turbulent (Ho & Huerre, 1984), when non-diamensionalised with the freestream velocity and the momentum thickness. Kim & Durbin (1988) examined also the response of the wake to acoustic forcing. They found that the base pressure decreased (thus increasing form drag) over a broad range of forcing frequencies, $0 < St < 3$. The same authors also noticed that the frequency of the vortex shedding was locked to half the forcing frequency, when forcing was applied near twice the shedding frequency.

A thorough investigation of the turbulent disk wake performed by Berger *et al.* (1990) revealed three distinct *instability mechanisms*. The first was antisymmetric fluctuations ($|m = 1|$) due to helical vortex shedding at a Strouhal number $St \approx 0.135$. The second was axisymmetric ($m = 0$) pulsation of the recirculation bubble at a $St \approx 0.05$. The third feature was a high frequency instability of the separated shear layer (Kelvin-Helmholtz instability) at $St \approx 1.62$. The structures in the near wake appeared to be coherent in space but random in time. Forcing the disk by nutation at a frequency close to the shedding frequency, it was observed that the shedding locks in and becomes coherent in time and space.

Bigger *et al.* (2009) performed experiments on a disk using pulsed jets and electromechanical tab actuators generating either symmetric or helical (travelling wave) $|m| = 1$ disturbances. The actuators for each disk comprised 6 slots on its circumference, oriented normal to the freestream and the time periodic velocity perturbations were provided either by the pulsed jet, or the motion of an electromechanical tab. Their primary result was the response of the base pressure to both types of forcing over a range of frequencies. The authors found that symmetric actuation for forcing frequencies close to twice the shedding frequency resulted in maximum shortening of the recirculation region with a base pressure decrease of up to 4%, in accordance to the results of Kim & Durbin (1988). On the other hand, helical $m = 1$ forcing at the shedding frequency was shown to be effective, when forcing was applied at the shedding frequency, with a more pronounced shortening of the recirculation length and base pressure decrease of up to 12%. For both types of forcing the mean flow remained axisymmetric in both cases.

Vilaplana *et al.* (2013) examined the global mode modification of the turbu-

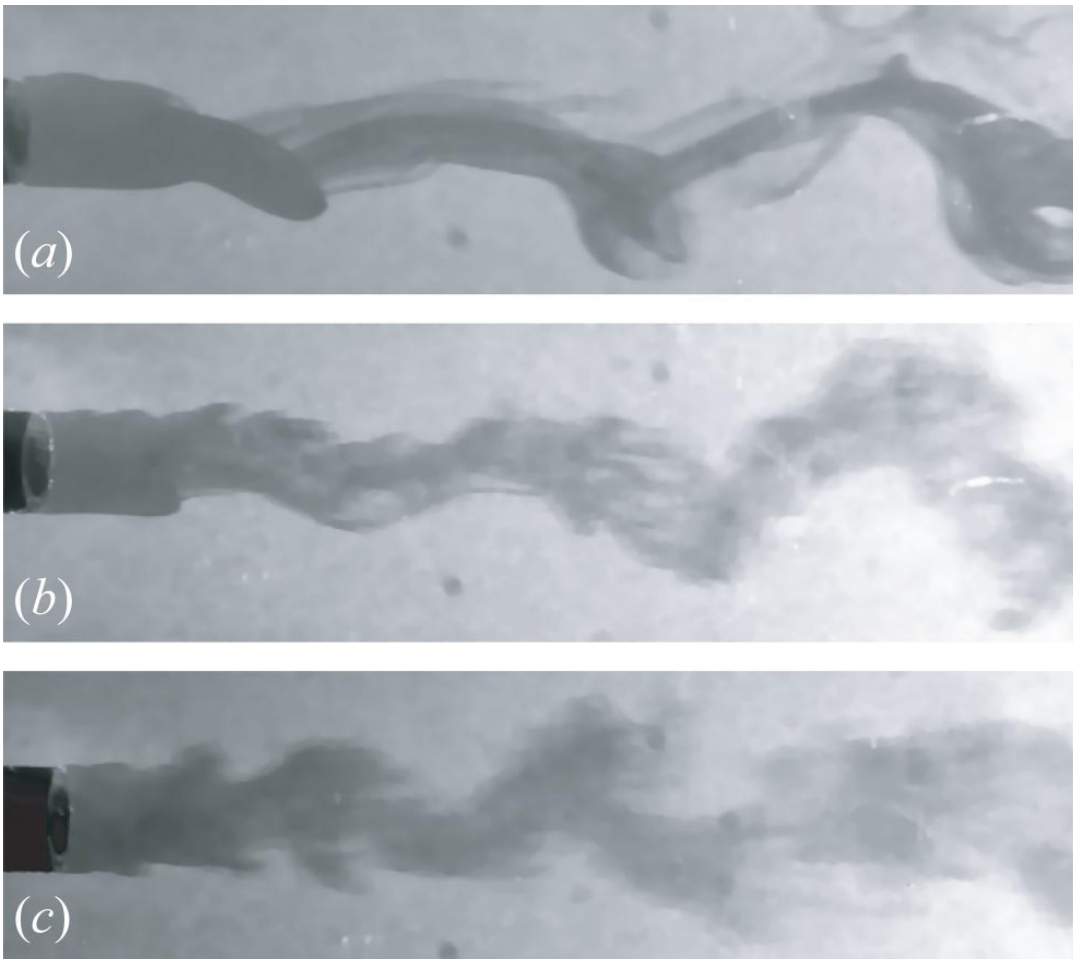

Figure 1.3.: Visualisations of the wake behind an axisymmetric bullet shaped body at various Reynolds numbers: (a) $Re = 1075$; (b) $Re = 1900$, (a) $Re = 2650$. After Sevilla & Martínez-Bazán (2004).

lent sphere wake ($Re = 33000$) and the sensitivity of it due to the presence of a secondary sphere in the near wake. They found that the undisturbed wake was dominated by the shedding of vortex loops (global mode) at $St = 0.19$ which exhibit planar symmetry. Although, the angle of the symmetry plane was random in the reference case, the control sphere was fixing the angle of the symmetry plane. The fixed angle was π radians rotated with respect to the control sphere and the shedding occurred always oposite of the location of disturbance. However the time-averaged flow was not axisymmetric due to the presence of four supporting wires.

Finally, although it is not an axisymmetric body, it is worth mentioning the work of (Grandemange *et al.*, 2012*a*, 2013) on the three-dimensional wake of an Ahmed body. The Ahmed body (Ahmed *et al.*, 1984), which is a box shaped sharp edged body with a rectangular cross section and rounded fore body, generates essential features of a real vehicle flow. Their results provide a clear demonstration of persistence of steady and unsteady laminar instabilities in the turbulent regime of three-dimensional body wakes. At low Re, the flow behind the Ahmed body preserves the spanwise planar symmetry of the geometry and the presence of the ground induces a top-bottom asymmetry of the wake. This state remains stable up to Re = 340, at which the wake undergoes a spatial steady bifurcation resulting in loss of reflectional symmetry; the wake is asymmetric the wake selects randomly one orientation (left-right) and stabilizes to an asymmetric position with respect to the spanwise direction. The steady bifurcation is followed by an unsteady one at $Re = 410$ giving rise to unsteady vortex shedding (Grandemange *et al.*, 2012*a*). These regimes were observed at $Re = 9.2 \times 10^4$ (Grandemange *et al.*, 2013). A detailed investigation though experiments showed that the turbulent recirculation region has two states associated with reflectional symmetry-breaking positions. Due to the equiprobable exploration of these two states, a statistically symmetric wake was observed in the long time-average. The sequence that these two states were explored was random (stationary Markov chain) giving rise to bistable behaviour.

1.3. Dynamic analysis of turbulent flow

Although the recent years a great increase in the understanding of turbulent flows has been gained, a complete predictive theory of them has not yet been established. This encompasses also the turbulent fluid flows generated by bluff obstacles and comes in contrast with the laminar and transitional regimes where hydrodynamic stability theory has been used effectively to describe and model most of the dynamic features of these flows. However, the properties of far wakes have been extensively investigated (Pope, 2000), but there is little hope of devising a complete wake theory until processes in the near wake, where most of the turbulent energy is produced, are more fully understood.

A number of approaches has been suggested for examining the stability of turbulent flow. Since turbulence appears to be characterised by *random* behaviour, a statistical approach sounds appropriate for their description. Using the equations of fluid motion, one can derive equations for the mean velocity

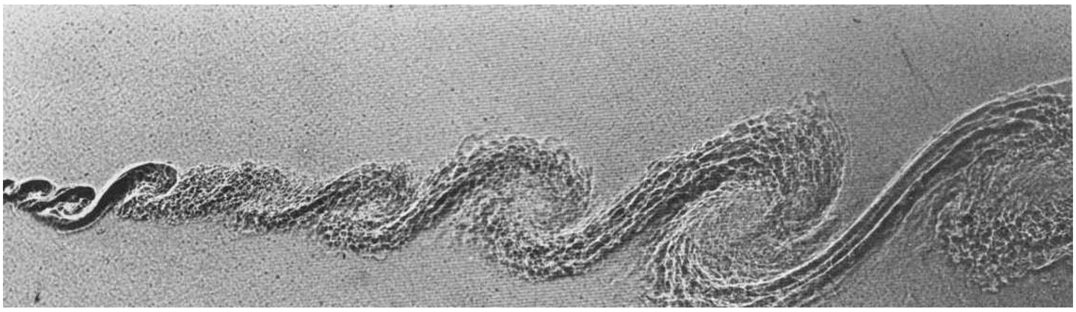

Figure 1.4.: Large scale coherent structures in mixing layers at high Reynolds numbers visualised by Brown & Roshko (1974). After Van Dyke (1982).

and pressure field and other statistical quantities. However, the equations for the statistics of turbulent flow do not form a closed set of predictive equations. For practical calculations of the statistical quantities, usually turbulent models are used yielding questionable results due to the lack of exact closures for the averaged equations.

The presence of coherent structures is a feature observed in many turbulent flows. An important characteristic of the coherent large-scale structures observed in open shear flows is that qualitatively resemble instability waves, see figure 1.4. It seems likely that such persisting macroscopic structure provide structural blocks for turbulent flows, and hence that analysis of the dynamics of these structures provides a basis for improved understanding of some aspects of turbulence. Hence, a significant part of turbulence modelling has been focused on turbulent flows with predominant coherent structures. In flows with pronounced coherent structures, such as wake flows, proper orthogonal decomposition[†] (POD) has been extensively used to to extract from experimental or simulated data empirical eigenfunctions that carry the greatest kinetic energy on average Holmes *et al.* (2012). POD provides basis functions onto which the Navier Stokes equations can be projected by Galerkin's method to yield a set of ordinary differential equations (ODEs). Variations of the method have been proposed by Noack *et al.* (2003) to include shift-modes.

Due to their significance of the coherent structures, their contribution has to be incorporated in the analysis. Reynolds & Hussain (1972) decompose the

[†]also known as Karhunen-Loéve decomposition or principal component analysis

flow quantities $\mathbf{q} = (\mathbf{u}, p)$ as:

$$\mathbf{q}(x,t) = \bar{\mathbf{q}}(\mathbf{x}) + \tilde{\mathbf{q}}(\mathbf{x},t) + \mathbf{q}'(\mathbf{x},t), \tag{1.9}$$

where $\bar{\mathbf{q}}$ is the mean value, $\tilde{\mathbf{q}}$ the contribution of the coherent structures (waves) and $\mathbf{q}'$ the turbulence. The standard Reynolds decomposition can be obtained when the coherent waves and random turbulence are both included in $\mathbf{q}'$.

Substituting the expansion (1.9) into the Navier-Stokes equations and time averaging, one finds that the mean flow $\bar{\mathbf{q}}$ is the steady solution of the equation when forced on the r.h.s by the Reynolds stresses of the organised wave and of the random turbulence. That is

$$\bar{\mathbf{u}} \cdot \nabla \bar{\mathbf{u}} + \nabla \bar{p} - \Delta \bar{\mathbf{u}}/Re = -\nabla \cdot \overline{\tilde{\mathbf{u}}\tilde{\mathbf{u}}} - \nabla \cdot \overline{\mathbf{u}'\mathbf{u}'} \tag{1.10}$$

The dynamical equation for the organised waves $(\tilde{u}, \tilde{p})$ around the turbulent mean flow $(\bar{u}, \bar{p})$ can be found in a similar manner (phase averaging and substracting the mean equation (1.10)), and is given by

$$\tilde{\mathbf{u}}_t + \bar{\mathbf{u}} \cdot \nabla \tilde{\mathbf{u}} + \tilde{\mathbf{u}} \cdot \nabla \bar{\mathbf{u}} + \nabla p - \Delta \tilde{\mathbf{u}}/Re = -(\nabla \cdot \tilde{\mathbf{u}}\tilde{\mathbf{u}} - \nabla \cdot \overline{\tilde{\mathbf{u}}\tilde{\mathbf{u}}}) - (\nabla \cdot \langle \mathbf{u}'\mathbf{u}' \rangle - \nabla \cdot \overline{\mathbf{u}'\mathbf{u}'}) \tag{1.11}$$

For the laminar case, the equation for the mean flow is forced only from the source term $\nabla \cdot \overline{\tilde{\mathbf{u}}\tilde{\mathbf{u}}}$, arising from the large scale structures (global modes). Then the linear stability of the mean flow can be examined based on equation (1.10) by taking the nonlinear forcing constant to a first approximation (Barkley, 2006). However, the mean flow is not a steady equilibrium of the Navier-Stokes equations and, therefore, may not be an appropriate base flow in order to determine its stability. Despite this, the above predicts well the frequency of the vortex shedding in the cylinder flow (Barkley, 2006). Although this approach seems promising it is not general; Sipp & Lebedev (2007) demonstrate that precise conditions must be met, explained from the weakly nonlinear analysis, for a linear stability analysis of a mean flow to be relevant and useful.

The above approach, that is addressing the stability of the mean flow has been used also for turbulent flows. For the turbulent case, however, an extra nonlinear forcing term is present, the Reynolds stresses arising from the turbulent motion $\overline{\mathbf{u}'\mathbf{u}'}$. Probably the simplest model for these terms is the turbulent viscosity model. This involves finding functional relationships between the Reynolds stresses and the mean velocity. Then one examines the evolution of perturbations on the turbulent mean flow. In this framework, Meliga *et al.* (2012) analysed the two-dimensional turbulent flow past a D-shaped cylinder simulated by solving unsteady Reynolds-averaged Navier-Stokes equations with a Spalart-Allmaras turbulence model. A global linear stability analysis of the mean flow, predicted well the frequency of the most unstable mode in the saturation regime.

1.4. Control of bluff body flows

Several methods have been proposed for controlling two- and three-dimensional bluff body flows and their efficiency has been been demonstrated in laminar and turbulent regimes. The control approach varies depending on the application and usually the target can be either promotion of instability (i.e. better mixing, delayed separation) or suppresion (i.e. drag, noise, structural load reduction). They can be divided in three categories depending on the type of actuation: passive, active open-loop and active closed-loop[‡] for cases of actuators without power unit, actuators with power input but no sensor, and sensors and actuators with power input, respectively (Gad-el Hak, 2000). Furthermore, depending on which part of the flow the control aims to modify, control can be classified into boundary-layer control and direct-wake control. In the first, control changes the boundary-layer flow characteristics and thus delays the main separation. This control method is used in bluff bodies having a movable separation point (i.e. sphere, cylinder). Conversely, the second method directly modifies the wake characteristics, and thus can be applied to all kind of bluff bodies having either a fixed or movable separation point. An extensive review of the methods used to control flow around bluff bodies has been given Choi *et al.* (2008).

Passive techniques generally involve geometrical modifications or additions to the main body. Mair (1965) and Weickgenannt & Monkewitz (2000) showed that a control disk mounted concentrically on the rear of a bullet-shaped body at high Reynolds numbers ($3 \times 10^3 \leq Re \leq 5 \times 10^4$) can alter significantly the drag exerted on the body and the vortex shedding activity in the near wake. A parametric analysis of the mounting separation distance of the disk from the base of the body revealed that significant drag reduction of up to 5% and

[‡]also known as feedback control

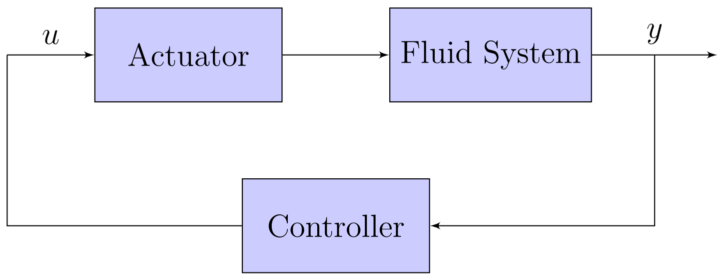

Figure 1.5.: Typical feedback control block diagram: a controller senses the state of the system y, computes corrective actions u and actuates the system to achieve the desired change.

attenuation of the vortex shedding can be achieved when the disk is positioned at a broad downstream distance $0.4D \leq x \leq 0.7D$. Decrease in the drag was observed also by Sanmiguel-Rojas *et al.* (2011) using a cylindrical base cavity on a bullet-shaped body at transitional regimes ($Re \leq 700$).

Application of feedback control methods on bluff bodies with fixed separation point is limited and there are only a few closed-loop control studies, using mainly-two-dimensional geometries. One example is the experimental work of Pastoor *et al.* (2008), who used feedback information to drive a zero-net-mass-flux actuator in order to control the flow around two-dimensional D-shaped body. The natural flow around these bodies is characterized by a short dead water region and alternating eddies in the vicinity of the base. Both are responsible for a low base pressure and thus for a high drag. The authors derived a reduced order vortex model for the flow (physics-based model) that resolved the coherent structures and the effects of the actuation. Based on this model, the proposed controller synchronizes upper and lower shear layer evolution, thus postponing vortex formation, as shown in figure fig:Pastoor. This resulted in 40% base pressure increase associated with 15% drag reduction.

Due to the present lack of theoretical models that capture effectively the dynamics of three-dimensional turbulent bluff body flows, implementation of successful feedback control strategies has not been demonstrated yet.

1.5. Outline

The objective of this work is twofold. Firstly, to contribute towards the understanding of the origin and the dynamics of coherent structures in turbulent wakes behind three-dimensional bluff bodies. Secondly, to develop physics-

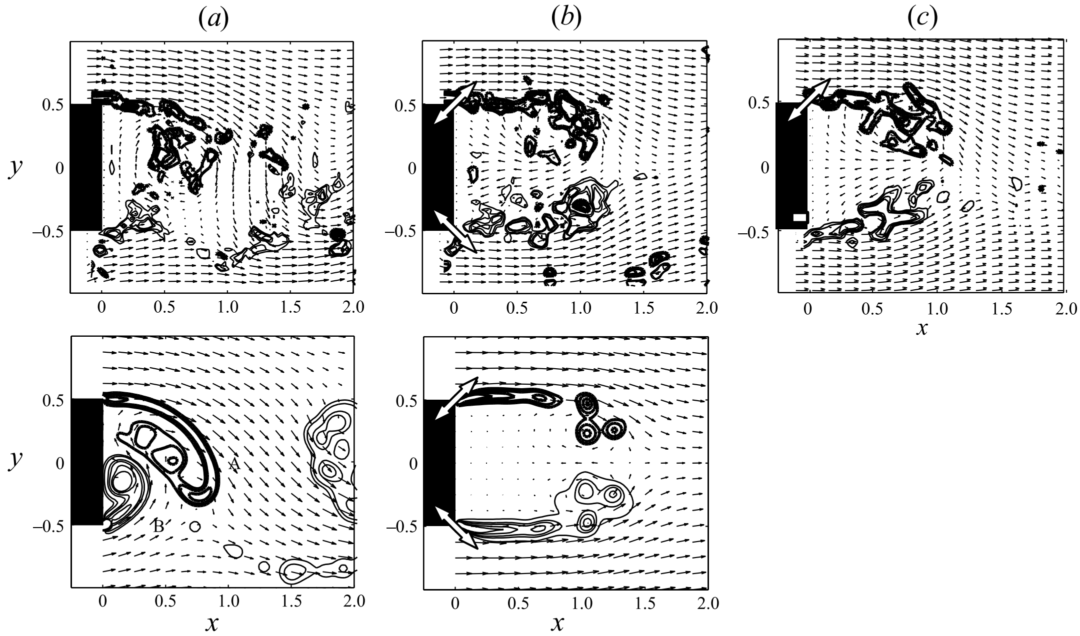

Figure 1.6.: Shear layer control behind a D-shaped body. Instantaneous flow fields are shown from the natural flow obtained from experiment (top) and vortex model (bottom): (a) Natural flow; (b) open loop in-phase forcing of top and bottom shear layers with forcing frequency being close to the shedding frequency ; (c) feedback control using only top actuator to synchronise both shear layers sensing the base pressure. After Pastoor *et al.* (2008).

based simple models that capture the observed turbulent dynamics. These models could be potentially used in feedback control strategies in order to manipulate at will the flow dynamics (i.e. drag exerted on the bluff bodies). The remainder of this thesis is presented as follows.

In chapter 2, the details of the experimental setup, sensors and actuators are discussed. This includes also the derivation of simple linear model for the actuator dynamics, and the assessment of the measurement equipment. Chapter 3 provides a detailed characterisation of the turbulent dynamics of the natural flow generated by a three dimensional bluff body. The dynamics of the turbulent wake are addressed and linked to the ones observed in the laminar and transitional regimes. In chapter 4 a simple stochastic model is proposed that captures important dynamic features of the baseline flow. In chapter 5, a detailed characterisation of the turbulent dynamics in the presence of external forcing is presented. In chapter 6, a weakly nonlinear model that describes the forced response of the turbulent wake is derived, extending the weakly nonlinear analysis of laminar flows in the turbulent regime. Conclusions and key findings, followed by recommendations for future work, are presented in chapter 7.

2. Experimental setup

2.1. Wind tunnel facility

Experiments were conducted in a closed circuit wind tunnel, the working section of which measures 0.91 m $\times$ 0.91 m $\times$ 4.8 m. The contraction ratio is 9 : 1 and the free-stream turbulence intensity is less than 0.1%. The free-stream velocity was computed from measurements of dynamic head, temperature of the flow and atmospheric pressure, which are sampled at 2.5 Hz by a Furness Controls micro-manometer model FCO510. A PID feedback controller with a set-point variation of less than 0.2% is used to maintain the free-stream velocity, $U_\infty = 15$ ms^{-1}.

2.2. The axisymmetric model

The wake is generated by an axisymmetric bluff-body with blunt trailing edge, a schematic of which is shown in figure 2.1. The body diameter, D, is 196.5 mm and the length-to-diameter ratio, L/D, is 6.48. The nose employs a modified super ellipse profile (Lin *et al.*, 1992) with an aspect ratio of 2.5. The boundary layer is conditioned by a 2 mm wide strip of 120 grit emery paper located at $z/L = -0.884$ (approximately the point of minimum pressure) followed by a 25 mm wide strip at $z/L = -0.784$. The axisymmetric body is supported in the centre of the wind tunnel test section using a NACA 0015/0030 blended aerofoil, such that a constant thickness of 11 mm was maintained throughout (Qubain, 2009). More details for the model are given by Oxlade (2013). The Reynolds number based on diameter and boundary layer momentum thickness at separation is $Re_D = 1.88 \times 10^5$ and $Re_\theta = 2050$ respectively, corresponding to turbulent wake and a turbulent boundary layer separation. The key experimental parameters are summarised in table 2.1.

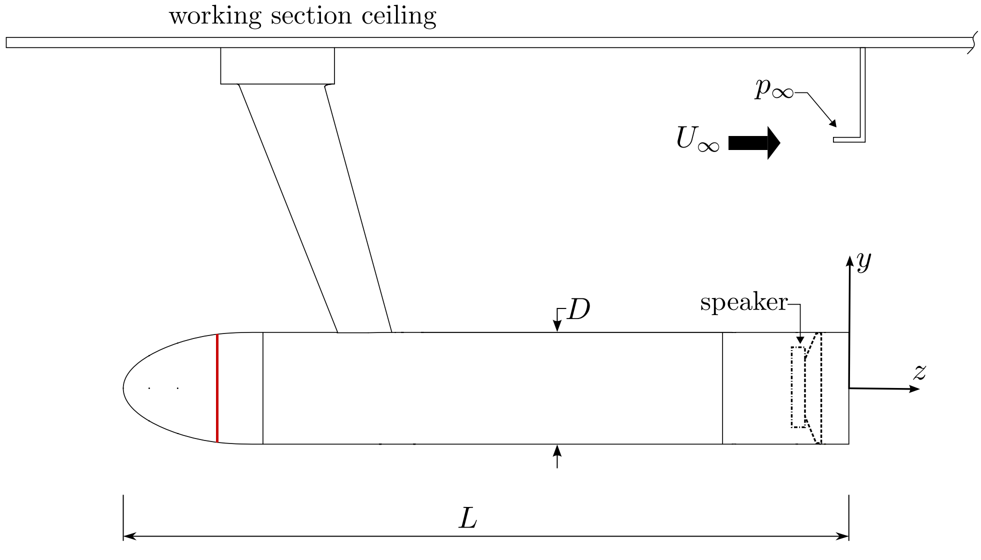

Figure 2.1.: Schematic of experimental set-up.

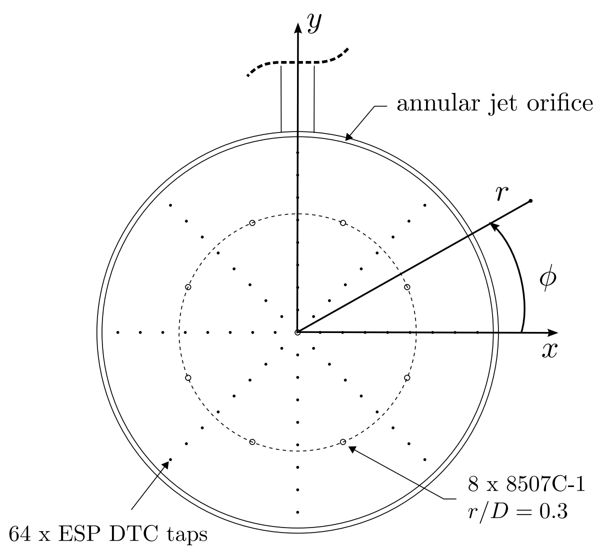

Figure 2.2.: Schematic of axisymmetric bluff-body base (rear view).

D [mm]	U_∞ [m/s]	L/D	Re_D	D/θ
196.5	15	6.48	1.88×10^5	89.3

Table 2.1.: Experimental parameters.

2.3. Body-mounted sensors

The base of the body is instrumented with: (i) 64 static pressure taps and (ii) 8 Endevco pressure sensors. All pressure measurements are differential measurements referenced to free-stream Pitot-static located at $z = 0$.

The 64 static pressure taps are equi-spaced on a uniform polar grid with $\delta r = 0.056D$ and $\delta\phi = 45°$ in the radial and azimuthal directions, respectively (figure 2.2). The pressure tappings have a diameter of 1.0 mm and depth-to-diameter ratio of 2. Static pressure is measured using an ESP-64HD DTC pressure scanner and a Chell CANdaq 14 bit D/A converter with a sampling frequency of 225 Hz. The scanner is connected to the tappings via 1.5 m lengths of 1 mm i.d. portex tubing. The flow through the portex tube results in attenuation of the pressure signal at high frequencies and for that reason the data obtained from the static taps were corrected using a method described in § 2.3.2.

The 8 Endevco 8507C-1 pressure transducers are azimuthally distributed ($\delta\phi = 45°$) on the base of the body at a radial location $r = 0.3D$. This type of sensor is a piezo-resistive differential pressure transducer with a flat frequency response up to 40 kHz, range of 1 psi, and an active sensing element diameter of 2 mm. The transducers are driven by Endevco Model 136 DC amplifiers with a gain of 1000 and a 10 kHz Butterworth filter.

The measured pressure is expressed in non-dimensional form as pressure coefficient (ratio of differential static pressure to the kinetic energy per unit volume of the approaching flow):

$$C_p = \frac{p - p_\infty}{\frac{1}{2}\rho U_\infty^2}. \tag{2.1}$$

By removing the dependence of pressure on on ρ and U_∞, it allows pressure distributions to be compared across experiments and scaled models, provided that the Reynolds number is kept constant.

2.3.1. Azimuthal Fourier decomposition

An important feature of the dynamic pressure transducers on the rear face of the model is that they allow the pressure distribution to be decomposed into azimuthal modes. Due to the 2π periodicity in the azimuthal coordinate, the signal obtained from the 8 dynamic pressure transducers can be expressed as a Fourier series

$$p(\phi,t) = a_0(t) + \sum_{m=1}^{M} \left[a_m(t)\cos(m\phi) + b_m(t)\sin(m\phi)\right] \tag{2.2}$$

where

$$a_0(t) = \frac{1}{2\pi}\int_0^{2\pi} p(\phi,t)\mathrm{d}\phi \ ; \qquad \begin{pmatrix} a_m(t) \\ b_m(t) \end{pmatrix} = \frac{1}{\pi}\int_0^{2\pi} p(\phi,t) \begin{bmatrix} \cos(m\phi) \\ \sin(m\phi) \end{bmatrix} \mathrm{d}\phi \tag{2.3}$$

Equation (2.2) can be also written as

$$p(\phi,t) = \sum_{m=0}^{M} c_m(t)e^{im\phi} + c.c. \tag{2.4}$$

Then, the Fourier coefficients are related via:

$$c_m = \begin{cases} \frac{1}{2}(a_m - ib_m) & \text{for } m>0 \\ \frac{1}{2}a_0 & \text{for } m=0 \\ \frac{1}{2}(a_{-m} + ib_{-m}) & \text{for } m<0 \end{cases} \tag{2.5}$$

$$\begin{aligned} a_m &= c_m + c_{-m} && \text{for } m = 0,1,2,\dots, \\ b_m &= i(c_m - c_{-m}) && \text{for } m = 1,2,\dots \end{aligned} \tag{2.6}$$

If we also perform a temporal Fourier decomposition, we can write (2.4) as an arbitrary superposition of counter-rotating waves:

$$p(\phi,t) = \sum_{n=0}^{N}\sum_{m=0}^{M} \left(c^{+}_{mn}e^{im\phi} + c^{-}_{mn}e^{-im\phi}\right)e^{\omega_n t} + c.c. \tag{2.7}$$

where c^{+}_{mn} and c^{-}_{mn} are the complex amplitudes of clockwise and counter-clockwise propagating rotating waves. Depending on the amplitude values, the wave can be a travelling/spinning wave, a standing/stationary wave or a

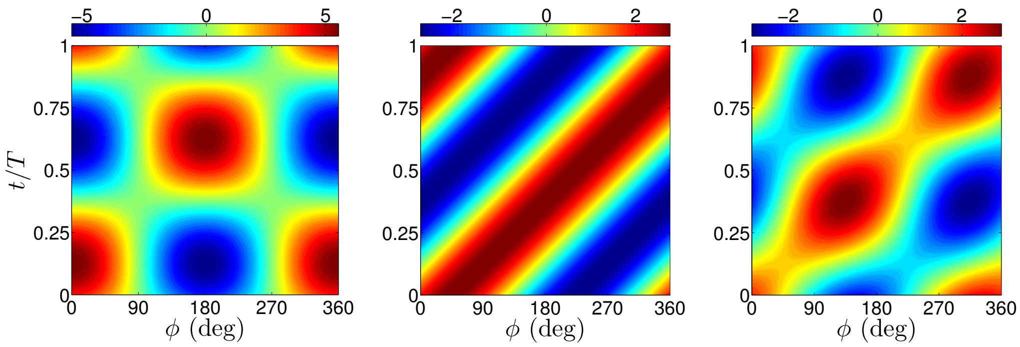

Figure 2.3.: Azimuthal modes evolving in time with azimuthal wavenumber $m = 1$ and frequency $\omega = 2\pi/T$: (a) standing with $c^+_{mn} = 1 + 1i$ and $c^+_{mn} = 1 + 1i$; (b) travelling with $c^+_{mn} = 1 - 1i$ and $c^+_{mn} = 0$; (c) mixed with $c^+_{mn} = 1$ and $c^+_{mn} = -0.5i$.

combination of the last two, which we call a mixed wave, see also figure 2.3. Note that the experimental setup includes eight dynamic pressure transducers, and so up to eight azimuthal mode amplitudes can be resolved experimentally; this limits M in equation (2.2) to 4.

2.3.2. Pressure signal calibration

The signal obtained from the 64 static pressure taps is attenuated due to the tubes connecting the static taps to the ESP sensor. Here, a methodology that corrects the pressure data obtained from the ESP is presented. The error between the true pressure signal at the measurement location p_r and the pressure signal measured with the ESP sensor p_s is due to (i) the attenuation flow through the pipe $h(t)$, and (ii) the sensor noise, $n(t)$.

Based on the above, we can write using time-domain notation:

$$p_s(t) = h(t) * p_r(t) + n(t), \tag{2.8}$$

where $h(t)$ is the impulse response of a filter, $n(t)$ the sensor noise, and $*$ denotes convolution. Equivalently, in the frequency domain equation 2.8 becomes:

$$P_s(\omega) = H(\omega)P_r(\omega) + N(\omega). \tag{2.9}$$

A schematic representation and the corresponding block diagram corresponding to the above filtering process are given in figure 2.4.

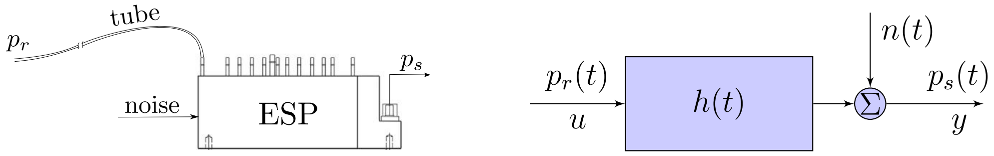

Figure 2.4.: Attenuation of the pressure signal obtained from the ESP sensor due to the connecting pipes. (a) Schematic and (b) block diagram.

System identification experiment

The calibration was performed against a reference signal obtained from Endevco 8507C-1 transducers. A pressure field is generated from a 6 in speaker (Beyma 6P200Nd), located at a distance $l = 10$ mm behind the base of the model. The pressure field is recorded simultaneously from the reference transducer, $p_r(t)$, and static pressure transducer, $p_s(t)$. The frequency-domain description of the system, consisting of the frequency response function $H(\omega)$ and the output noise spectrum $\Phi_n(\omega)$ are estimated using spectral analysis. A Blackman-Tukey approach (Ljung, 1998) is used to estimate

$$H(\omega) = \frac{\Phi_{yu}(\omega)}{\Phi_u(\omega)}, \tag{2.10}$$

from the Fourier transform of the covariance and cross-covariance of the input $u = p_r$ and output $y = p_s$.

The frequency response of $H(\omega)$ and the power spectral density of the noise Φ_n are shown in figure 2.5. A discrete first order filter, H_{fit}, was fit to the frequency response of $H(e^{i\omega})$ for visualisation purposes. The spectral density of is approximately constant (white) in most of the frequency domain. The cut-off frequency (-3 dB) is 18 Hz (approximately the frequency of the vortex shedding mode at $U_\infty = 15$ m/sec , $St = 0.2$).

Correction of the pressure signal

Given the noisy and attenuated (filtered) signal obtained from the static taps $p_s(t)$, an estimate of the true signal, $\hat{p}_r(t)$ can be obtained. The process is carried out in the frequency domain as follows. The amplitude of the noise is subtracted from the static tap signal P_s, and multiplied with the inverse frequency response, $1/H$. Through this process the filtering effect of the pressure signal obtained from the static taps can be eliminated.

In figure 2.7, the spectral density of the reference pressure signal obtained

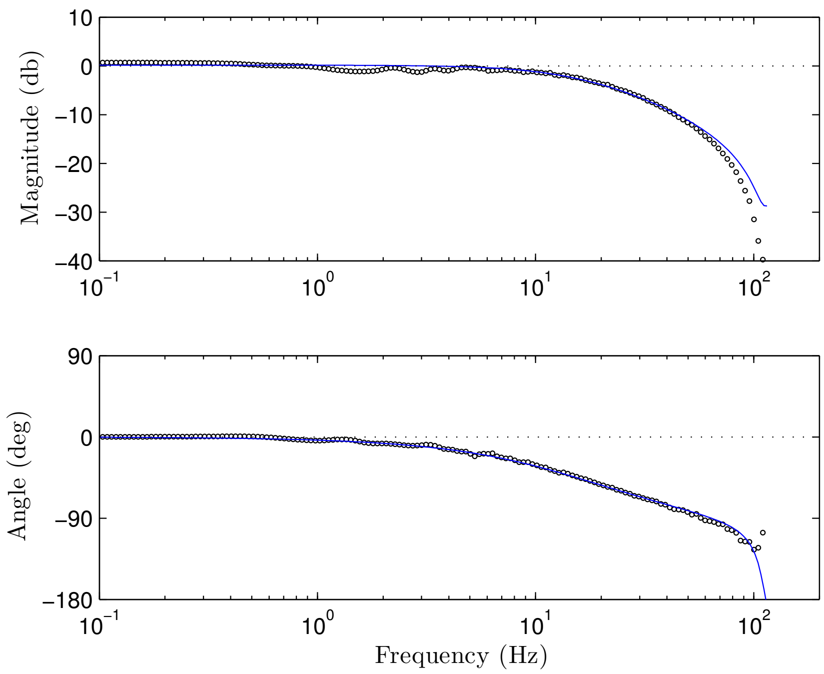

Figure 2.5.: Frequency response of H (symbols) together with a 1st order filter fit (line).

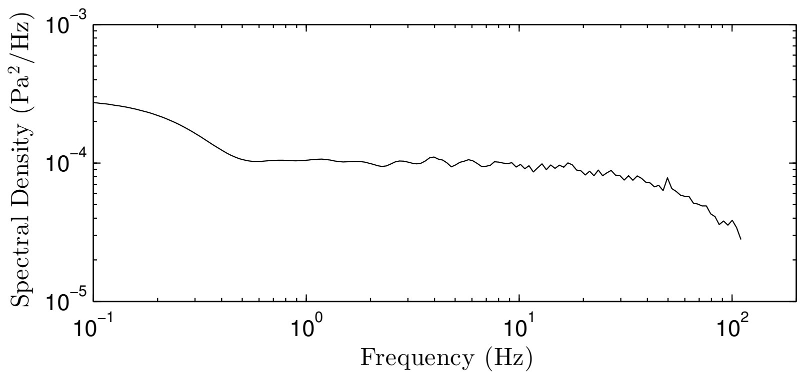

Figure 2.6.: Power spectral density of noise Φ_n.

from the Endevco transducers and the raw pressure signal from the static taps at $r = 0.3D$ during a wind tunnel test are plotted. The filtering process becomes pronounced above the cut-off frequency, approximately at 18 Hz, and results in a deviation of the two curves. Applying the correction procedure described above, the two curves collapse, as expected, validating the correction procedure.

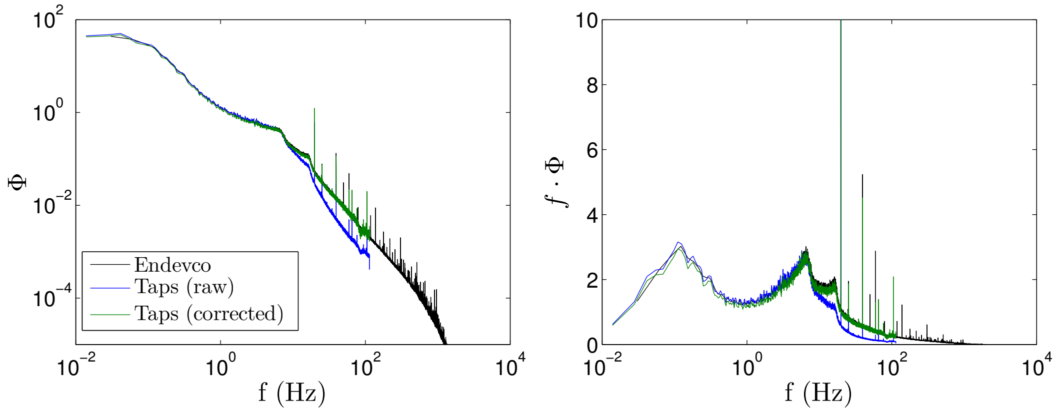

Figure 2.7.: Validation of the pressure calibration procedure. Spectra (left) and pre-multiplied spectra (right) of the pressure signal on the base: reference from Endevco transducers (black), raw (blue) and corrected data from taps (green).

2.3.3. Limitations of the sensors

Mean pressure data are obtained and presented only from the static taps. The Endevco 8507C-1 is not suitable for measurement of small changes in mean pressure due to its inherent drift.

Fluctuating base pressure measurements are presented from both types of sensors. However the frequency resolution of the static taps is limited to 112.5 Hz (Nyquist sampling frequency). Also, an offline correction of the signal is required to compensate for the filtering effect due to the tubing.

Key advantage of the Endevco signal is its potential use for feedback control since the signal can be accurately obtained without jitter in real time. Also, its relatively high sensitivity (approximately 24 mv/kPa) and low noise level (typically 5 μV RMS) make it an excellent choice for measurement of the fluctuating base pressure when frequencies up to 20 kHz are required.

2.4. The ZNMF actuator

Appropriate forcing for interacting with the wake behind the axisymmetric bluff-body was provided by a Zero-Net-Mass-Flux (ZNMF) actuator. The basic components of a ZNMF device are an oscillatory diaphragm (here loudspeaker), a cavity and an orifice. A high-fidelity loudspeaker (Beyma 6P200ND) mounted inside the model is used to generate a pulsed jet of variable frequency and amplitude. A QSC RMX 850 high fidelity power amplifier drives the loudspeaker. The jet issues in the free-stream direction from a 2.0 mm annular slit, located 1.0 mm below the trailing edge, as shown in figure 2.2. The jet velocity is uniform in the azimuthal direction, hence forcing is axisymmetric with azimuthal wavenumber $m = 0$.

2.4.1. Cavity pressure and jet velocity measurements

One Endevco 8507C-2 (2 psi range) transducer is mounted on the interior face of the base for measurement of the actuator cavity pressure.

Measurements of the the centreline jet velocity were performed with single-wire thermal anemometry. A one-component sensor was operated in constant temperature mode by a Dantec miniCTA 54T30 with in-built signal conditioner. The miniCTA's lowpass filter was set to a -3 dB cut-off frequency of 10 kHz, and the analogue signal was sampled at 25 kHz to minimise aliasing. The single-wire probe consisted of a 55P15 Dantec boundary layer probe with a 10% platinum-rhodium Wollaston wire soldered to the prongs. The wire was etched to a sensor diameter and width of 5 and 1000 μm respectively.

The hot-wire was calibrated in the free stream of the wind tunnel, by varying the free stream velocity and recording the raw output voltage obtained from miniCTA. Measurements were performed with the hot-wire positioned at the vertical and streamwise location of the Pitot-probe with a spanwise separation of $\approx$ 200 mm. The hot-wire was calibrated in-situ using an interpolating cubic spline. The calibration velocity range was adjusted to cover the specific range of velocities in the actuator measurements. A typical hot-wire calibration curve is shown in figure 2.8a.

The signal from the hot-wire measurements, when the actuator is driven with a sinusoidal signal, appears similar to a rectified sinusoidal signal, due to the directional ambiguity of the hot-wire. The direction of the velocity

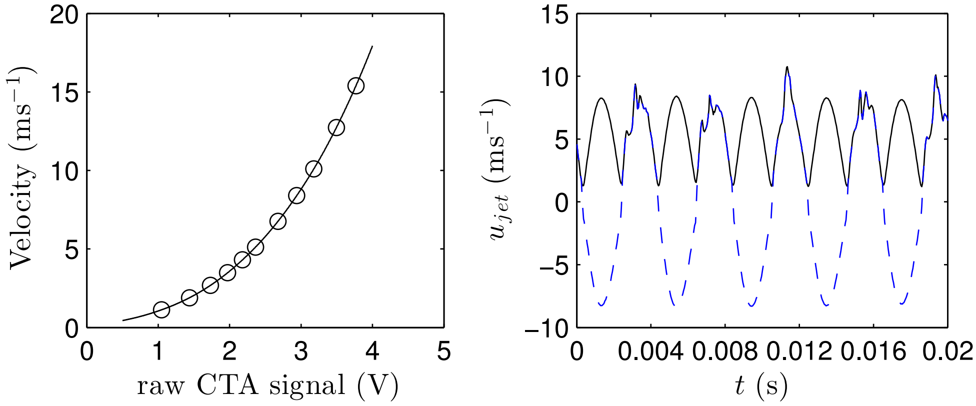

Figure 2.8.: Jet velocity measurements. (a) Typical hot-wire calibration curve; experimental data (symbols) and interpolating spline (line). (b) Derectification of the velocity signal; original (solid line) and derectified signal (dashed line).

cannot be inferred from the hot-wire probe; only the local velocity magnitude is determined. A procedure similar to that used by Chaudhari *et al.* (2009) has been employed to reverse the hot-wire signals. A post-processing code was developed to split the signal into expulsion and ingestion and reverse the latter. It is assumed that expulsion of the fluid is represented by the large peak and ingestion by the smaller one. The result of this procedure is presented in figure 2.8b.

2.4.2. A model for the actuator dynamics

A simple linear model is derived based on first principles to describe the ZNMF actuator dynamics and relate the input (driving voltage) with the output (jet velocity). The model derived here allows us to decouple the dynamics of the flow and the actuator dynamics. *Link this with feedback control diagram.*

Figure 2.9 indicates the relevant nomenclature for the diaphragm (speaker) and synthetic jet actuator. The relations among actuator deflection x_d, cavity pressure p_{cav} and jet velocity u_{jet} are described by the following linear differential equations (Persoons & O'Donovan, 2007; Persoons, 2012):

Conservation of mass in the cavity, combined with ideal gas law and assuming adiavatic compression/expansion:

$$\frac{1}{\gamma p_0}\frac{dp_{cav}}{dt} = \frac{A_d}{V}\frac{dx_d}{dt} - \frac{A_s}{V}u_{jet}. \tag{2.11}$$

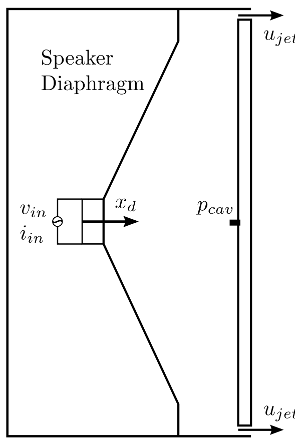

Figure 2.9.: Schematic of ZNMF actuator.

Conservation of momentum in the orifice, assuming linear damping force:

$$m\frac{du_{jet}}{dt} + cu_{jet} = p_{cav}A_s \tag{2.12}$$

The relations linking driving voltage v_{in} and current i_{in} with x_d and p_{cav} are given by the governing equations of the electromechanical system. Speciffically, a force balance of the mechanical system (diaphragm) gives

$$M_d\frac{d^2x_d}{dt^2} + C_d\frac{dx_d}{dt} + K_d x_d = Bli_{in} - p_{cav}A_d, \tag{2.13}$$

where $F_d = Bli_{in}$ is the electromagnetic force produced by the current in the coil. The differential equation describing the electrical system (voice coil) is:

$$v_{in} = Ri_{in} + L\frac{di_{in}}{dt} + Bl\frac{dx_d}{dt}. \tag{2.14}$$

We apply the Laplace transform on the differential equations (2.11)–(2.14) to obtain polynomials in $s = i\omega$, the Laplace variable (time domain to the complex frequency domain). Solving for U_{jet}/V_{in}, we find the following transfer function between output jet velocity and driving voltage:

$$\frac{U_{jet}(s)}{V_{in}(s)} = \frac{K_1\, s}{\underbrace{(s+\omega_3)}_{\text{Coil}}\underbrace{(s^2+2\zeta\omega_2 s+{\omega_2}^2)}_{\text{Helmholtz}}\underbrace{(s^2+2\zeta\omega_1 s+{\omega_1}^2)}_{\text{Diaphragm}}} \tag{2.15}$$

Combining (2.12) and (2.15), it can be easily shown that:

$$\frac{P_{cav}(s)}{V_{cav}(s)} = \frac{P_{cav}(s)}{U_{jet}(s)}\frac{U_{jet}(s)}{V_{in}(s)} = \frac{K_1\, s(ms+c)/A_s}{(s+\omega_3)(s^2+2\zeta\omega_2 s+{\omega_2}^2)(s^2+2\zeta\omega_1 s+{\omega_1}^2)}. \tag{2.16}$$

The parameters of the model were determined based on the geometric characteristics of the cavity and orifice and the loudspeaker specifications (table 2.2). The damping factor of the orifice, c, is the only parameter that was obtained experimentally.

The "true" transfer function was obtained experimentally by exciting the actuator with a broadband frequency signal (white noise) and recording the cavity pressure. On the other hand, monochromatic harmonic signals where used to excite the actuator for the jet velocity measurements, in order to apply the derectification procedure. Estimates of the input and the cross spectrum between input and output, $\Phi_u(\omega)$, $\Phi_{yu}(\omega)$ were formed to estimate the frequency function from output to input as follows:

$$\widehat{G}(i\omega) = \frac{\Phi_{yu}(\omega)}{\Phi_u(\omega)} \tag{2.17}$$

In figure 2.10, the frequency response function between cavity pressure and driving voltage of the ZNMF actuator is plotted. The experimental results are compared with the predictions of the numerical model (equation (2.16)) and a good match is obtained. The same conclusions hold for the frequency response function between jet velocity and cavity pressure plotted in figure 2.11. The full transfer function of the actuator between driving voltage and jet velocity can be obtained as the product of the two above transfer functions.

The above numerical models can be used for direct estimation of the jet velocity directly form the cavity pressure or input voltage signal. The last two can be accurately obtained during the experiment using simple acquisition techniques. The advantage of using the cavity pressure is that some of the time varying dynamics of the actuator related with the electromechanical system (i.e. changes of parameters due to heat) and were not modelled here are decoupled from the estimation process.

Parameter	V	A	γ	c	m	A_d	M_d	C_d	K_d	R_e	L_e	Bl
Value	7.6×10^{-4}	0.0123	1.4	0.0004	2.22×10^{-5}	0.015	0.017	1.81	2.13×10^{3}	5.3	600	10.5
Unit	m^3	m^2	-	kg/s	kg	m^2	kg	kg/s	N/m	Ω	H	N/A
	Cavity volume	Slit area	Heat ratio	Orifice damping coef.	Orifice gas mass	Diaphragm area	Diaphragm mass	Diaphragm damping coef.	Diaphragm stiffness	D.C. voice coil resistance	Voice coil inductance	Electrical-mechanical conversion factor

Table 2.2.: ZNMF model parameters.

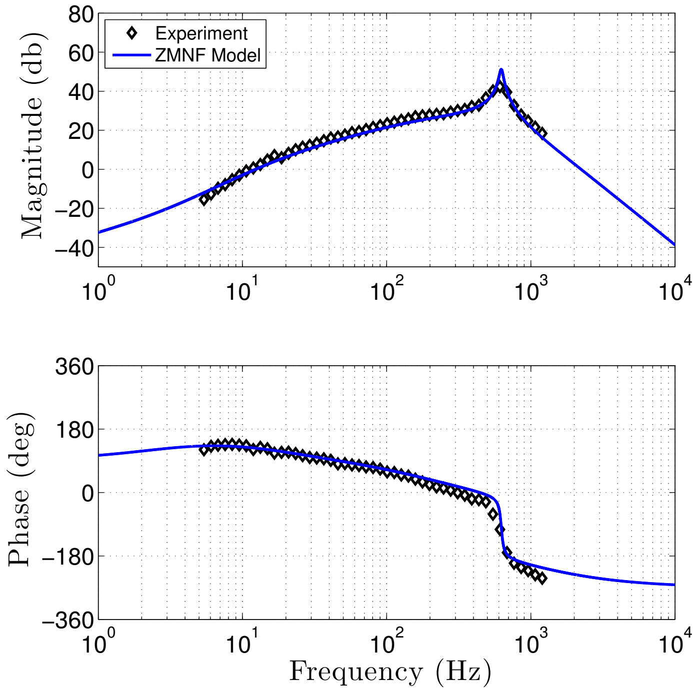

Figure 2.10.: Frequency response function of the ZNMF actuator between cavity pressure and driving voltage: P_{cav}/V_{in}.

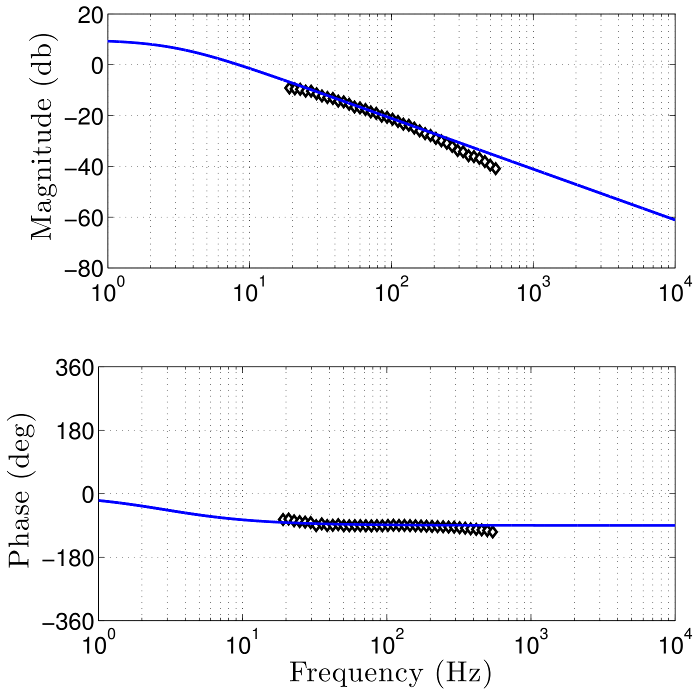

Figure 2.11.: Frequency response function of the ZNMF actuator between jet velocity and cavity pressure: U_{jet}/P_{cav}.

2.5. Acquisition and control system

Acquisition of the sensor data and control of the actuator is performed by a National Instruments PXIe-1078 chassis running a code written in Labview v11.0.The PXI is fitted with a PXIe-8102 controller running Real Time Operating System and a PXIe-6358 module with 4 simultaneous 16-Bit D/A output channels and 16 simultaneous 16-Bit A/D input channels. The components of the acquisition system were chosen such that it can be used for open-loop and closed-loop control.

3. The axisymmetric bluff-body wake

In this chapter, the dynamics of the flow generated behind the three dimensional axisymmetric body are investigated. The analysis is performed based on pressure measurements on the base of the body. Although the wake is highly turbulent ($Re_D \sim 2 \times 10^5$), it is shown that the coherent structures are closely related to the ones observed in the laminar regimes.

3.1. Flow characteristics

Pressure measurements are expressed as a pressure coefficient, non-dimensionalised by the free-stream dynamic head $1/2\rho U_\infty^2$. Frequency spectra are calculated using blocks of 2^{14} data points and a Hanning window with 50% overlap. Frequencies are expressed as Strouhal numbers, $St = fD/U_\infty$.

A total of 19,200 s of data was acquired over sixteen independent experiments, providing approximately 2000 independent measurements with a 95% uncertainty of approximately 0.45% and 1% in time average and rms pressure respectively.

3.1.1. Base pressure distribution

The mean and root-mean-square pressure distribution obtained from the 64 pressure taps on the base of the body are shown in figure 3.1. A region of constant low pressure extends from the body axis up to approximately $r/D = 0.2$, with pressure recovery increasing towards the edge of the body. Conversely, the fluctuating pressure exhibits a maximum at approximately $r/D = 0.15$. Both pressure distributions are axisymmetric to within $\pm 1\%$.

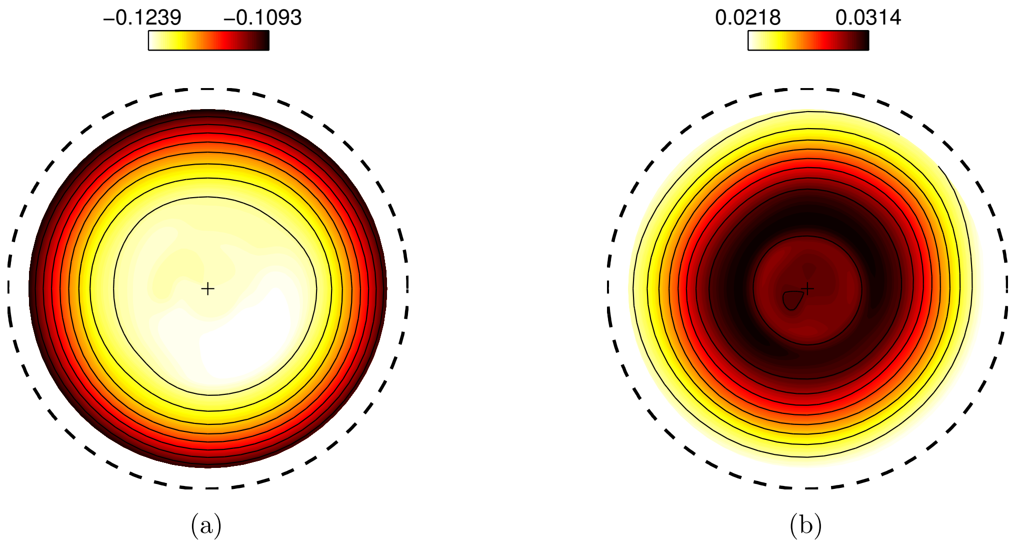

Figure 3.1.: Pressure distribution on the base of the body: (a) mean and (b) root-mean-square of the fluctuating component. The dashed circle indicates the body diameter.

3.1.2. Azimuthal modes

A spatial Fourier decomposition of the pressure signal $p(r, \phi, t)$ in the azimuthal direction gives azimuthal modes,

$$p_m(r, t) = \frac{1}{2\pi} \int_0^{2\pi} p(r, \phi, t) e^{-im\phi} \mathrm{d}\phi. \tag{3.1}$$

A subsequent temporal Fourier transform of the azimuthal modal amplitudes gives

$$\begin{aligned} P_m(f, r) &= \int_0^T p_m(r, t) e^{-2\pi f t} \mathrm{d}\phi \mathrm{d}t \\ &= \frac{1}{2\pi} \int_0^T \int_0^{2\pi} p(r, \phi, t) e^{-i(m\phi + 2\pi f t)} \mathrm{d}\phi \mathrm{d}t. \end{aligned} \tag{3.2}$$

Then, for a double Fourier transform $P_m(f; r)$ of the pressure signal $p(r, \phi, t)$ in the azimuthal direction and in time, the spectral density per mode, m, for a given radius, r, is given by

$$\Phi_m(f, r) = \frac{2}{T} \left| P_m(f; r) \right|^2. \tag{3.3}$$

Coherent structures are identified in figure 3.2 calculating the azimuthal spectral energy $\bar{\Phi}_m(St)$ distributed over $St = fD/U_\infty$, and averaged over the radius, such that

$$\overline{p_m^2} = \frac{8}{D^2}\int_0^{D/2}\int_0^{\infty} St\ \Phi_m(r, St)\mathrm{d}(\log St)r\mathrm{d}r. \tag{3.4}$$

The dominant mode shapes and their associated frequencies are shown in table 3.1.

Spectral peaks at $St \approx 0.2$ (d) are associated with the global oscillatory mode of the wake: vortex shedding with azimuthal wavenumber $m = \pm 1$. The frequency and shape are consistent with previous experimental observations from bodies of similar geometry (Sevilla & Martínez-Bazán, 2004; Grandemange *et al.*, 2012b). The $m = \pm 1$ spectra show also peaks at $St \approx 0.1$ (c), which are close to the subharmonic of the shedding mode. The same frequency is also observed in the modes $m = \pm 2$.

We also observe that the $m = \pm 1$ mode oscillates with a very low frequency (VLF) centred at $St \approx 0.002$ (a), which is approximately two orders of magnitude less than the shedding frequency. A similar timescale, $t \sim 10^3 D/U_\infty$, has been reported recently in the three dimensional wake of an Ahmed body for high Reynolds numbers (Grandemange *et al.*, 2013). For the Ahmed body, this long timescale was linked to the random shifts of the recirculation region between two preferred reflectional-symmetry-breaking positions leading to a statistically symmetric wake. The dynamics of this structure for the axisymmetric wake are investigated in §3.2.

An axisymmetric ($m = 0$) pulsation of the vortex cores, known as "bubble pumping" (Berger *et al.*, 1990), is identified at a low frequency of $St = 0.06$ (b). The intensity of the axisymmetric pulsation increases as the axis of the body is approached. The frequency and shape of this mode is very close to the low frequency oscillation of the wake observed by Bohorquez *et al.* (2011) and Bury & Jardin (2012) for a body of similar geometry in the transitional regime at low Reynolds numbers.

3.1.3. Proper orthogonal decomposition

Proper orthogonal decomposition has been shown to be an effective way to systematically extract coherent structures of turbulent flows based on their energy content (Lumley, 1970; Holmes *et al.*, 2012). Figure 3.3 shows the

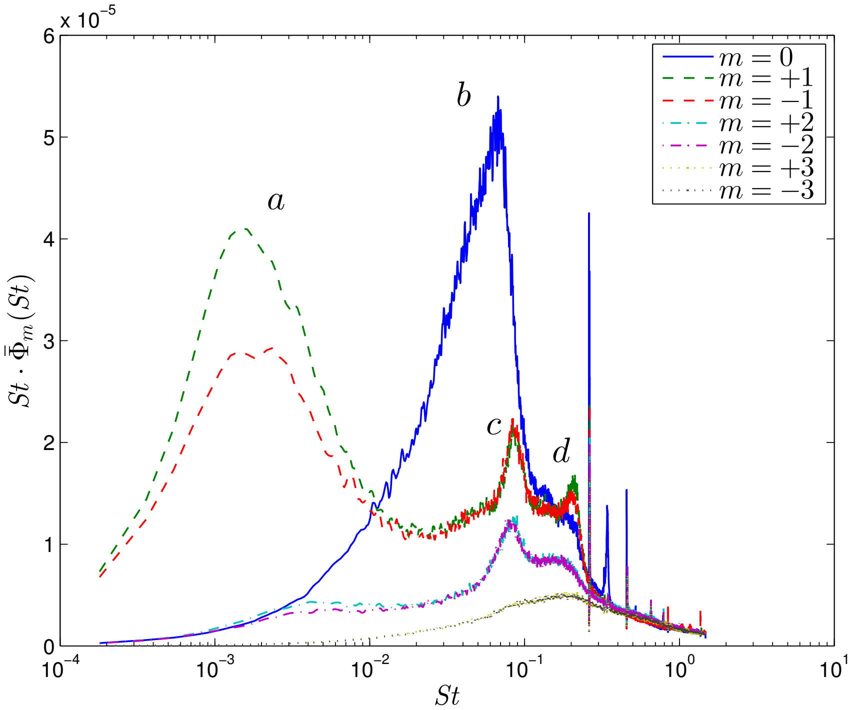

Figure 3.2.: Premultiplied pressure spectra of the azimuthal modes on the base of the axisymmetric body. Spectra are radially averaged and the areas underneath correspond to energies; spectral peaks show where the energy is concentrated.

	a	b	c	d	POD Modes
$m = 0$		0.06			3
$m = \pm 1$	0.002		0.1	0.2	1, 2
$m = \pm 2$			0.1		4, 5

Table 3.1.: Dominant modes and associated Strouhal numbers based on energy content.

energy distribution of the 20 most energetic POD modes of the base pressure. It can be seen that the first three modes carry $\sim 72\%$ of the total energy.

Figure 3.4 shows the first five POD modes of the base pressure and the corresponding premultiplied spectral density Φ of the POD coefficients. The coefficients are computed by projecting each mode onto the instantaneous pressure field (Holmes *et al.*, 2012). The first five POD modes capture all the coherent structures, based on the presence of spectral peaks in figure 3.2; no peaks are

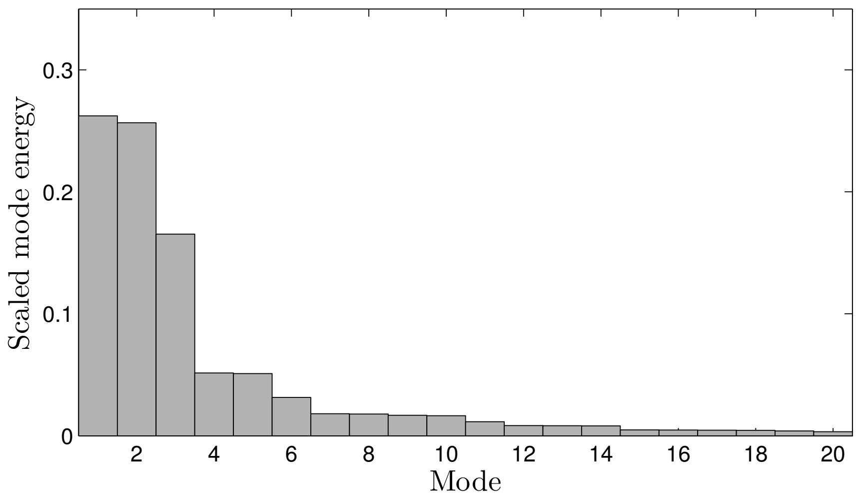

Figure 3.3.: Energy of the first 20 POD modes.

detected in the spectra of the remaining POD amplitudes.

The first two most energetic POD modes (modes 1 and 2) correspond to the modes with azimuthal wavenumber $m = \pm 1$ in table 3.1, the third POD mode to the axisymmetric $m = 0$ pulsation, and the fourth and fifth to $m = \pm 2$ modes.

3.2. Symmetries of the flow

Insight to the symmetry of the wake and its link to the coherent structures of the turbulent wake is given by the Centre-of-Pressure (CoP), calculated from the space-averaged pressure, defined on the Cartesian coordinate system of the base, $\mathbf{x} = (x, y)$, as

$$\mathbf{R}(t) = [R_x(t), R_y(t)] = \frac{1}{\int p(t)dA} \int_A p(t)\mathbf{x}dA, \tag{3.5}$$

where A is the area of the base of the body. The CoP provides a direct way to quantify the magnitude of the asymmetry in the turbulent regime: a zero value (CoP lies on the centre) will correspond to an $\mathcal{R}_\pi$-symmetric flow ($\phi \to -\phi; P \to P$), whereas departure from this value will correspond to an increased asymmetry of the flow.

The temporal evolution and PDF of the radial and azimuthal location of the CoP for the highly turbulent regime are shown in Fig. 3.5. Highly erratic

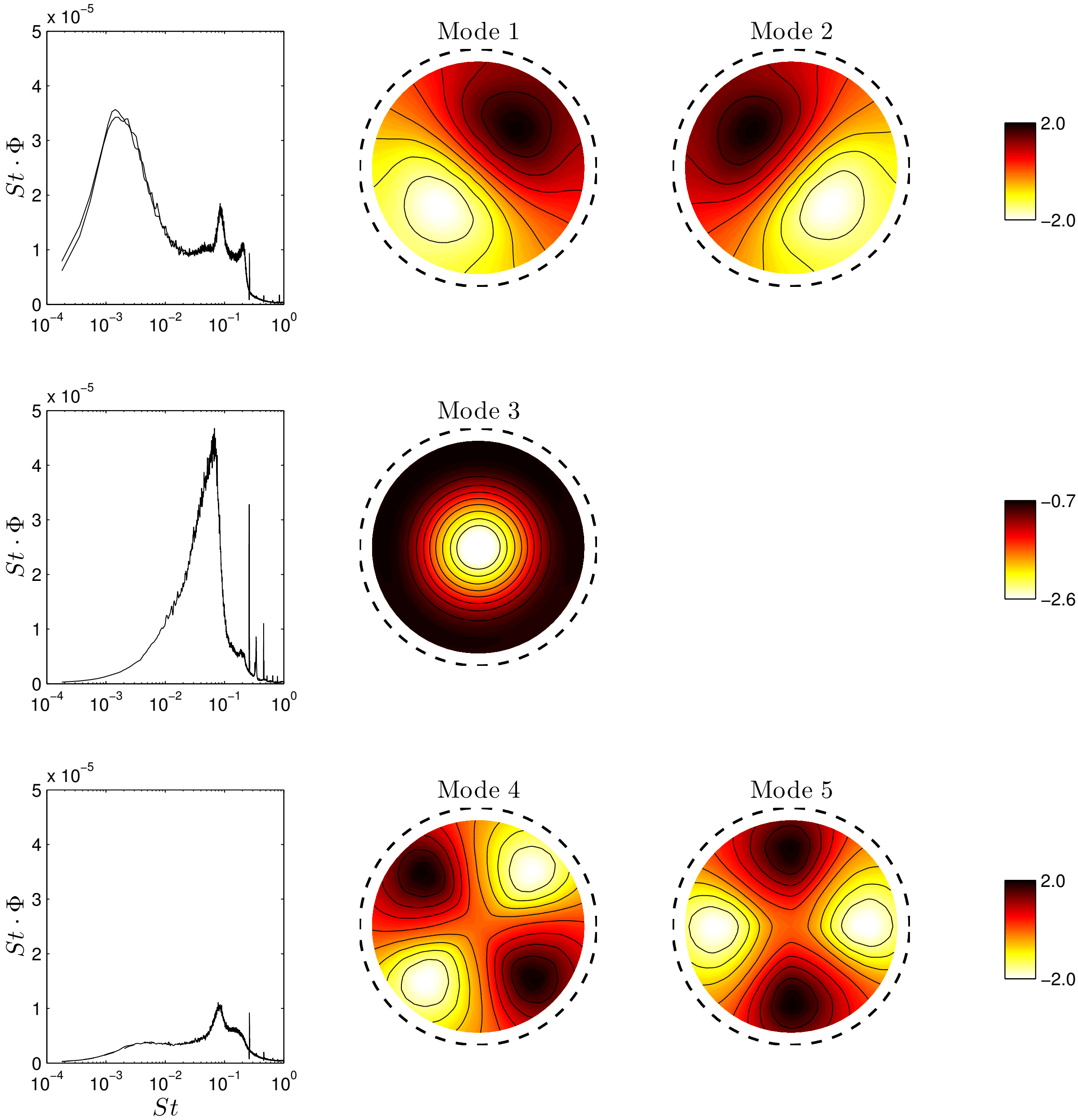

Figure 3.4.: First five POD modes and premultiplied spectra of their amplitudes: (a–c) antisymmetric modes 1–2 with $|m| = 1$; (d–e) axisymmetric mode 3 with $m = 0$ and, (f–h) antisymmetric modes 4–5 with $|m| = 2$.

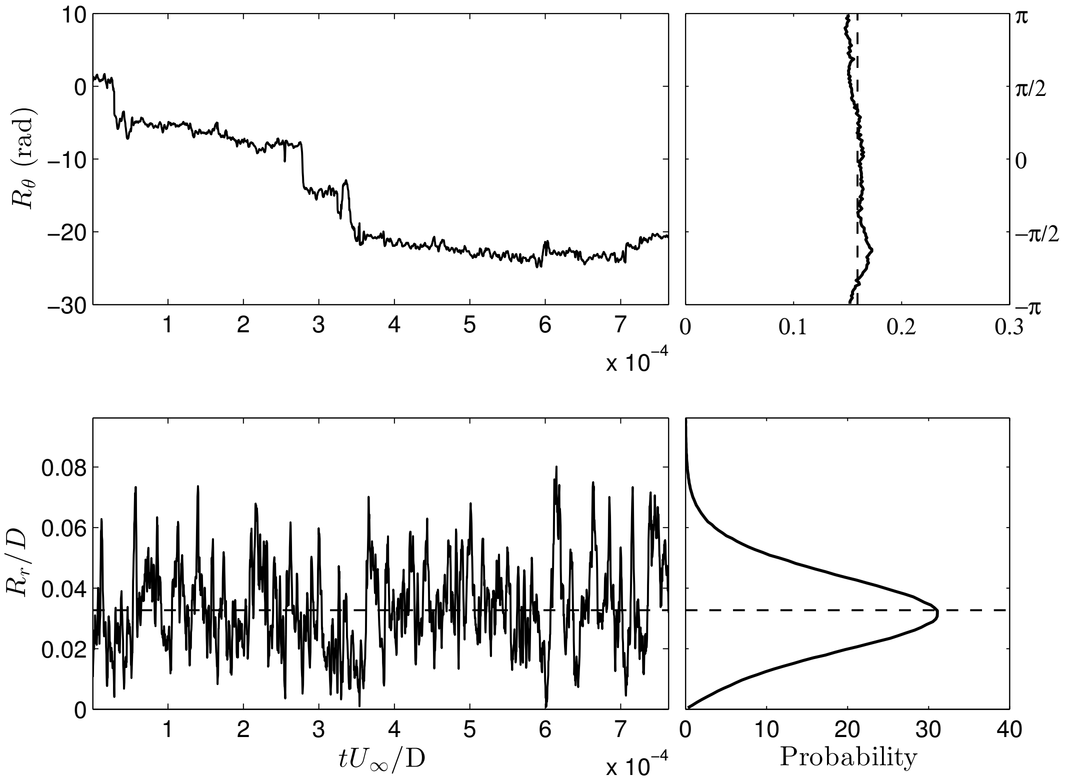

Figure 3.5.: A time series and probability density of the Centre-of-Pressure. Radial (lower) and azimuthal (upper) positions.

motion rapidly varying in time is observed in both components. Statistically, the wake spends most of the time in a non-zero radial location. In the azimuthal direction, it can explore any angle with equal probability and in the long time average the probability distribution function converges to the uniform one.

The two-dimensional probability density function of the CoP is plotted in figure 3.6. It shows that the most probable location of the CoP lies on a circle with $R_r = 0.03D$ centered on the base of the body, indicating a tendency to lock to this value. The probability of the azimuthal position of the CoP is consistent with a uniform distribution within the experimental error (small deviations from the uniform distribution are mainly due to imperfect alignment of the experimental setup, which is also evident in the energy imbalance of the VLF mode in figures 3.2 and 3.3). Due to the uniform distribution, an axisymmetric pressure field is obtained in the long time average. However, the non-zero mean radial value of the CoP provides strong evidence that the wake is asymmetric, for a fixed angle of the CoP, on average.

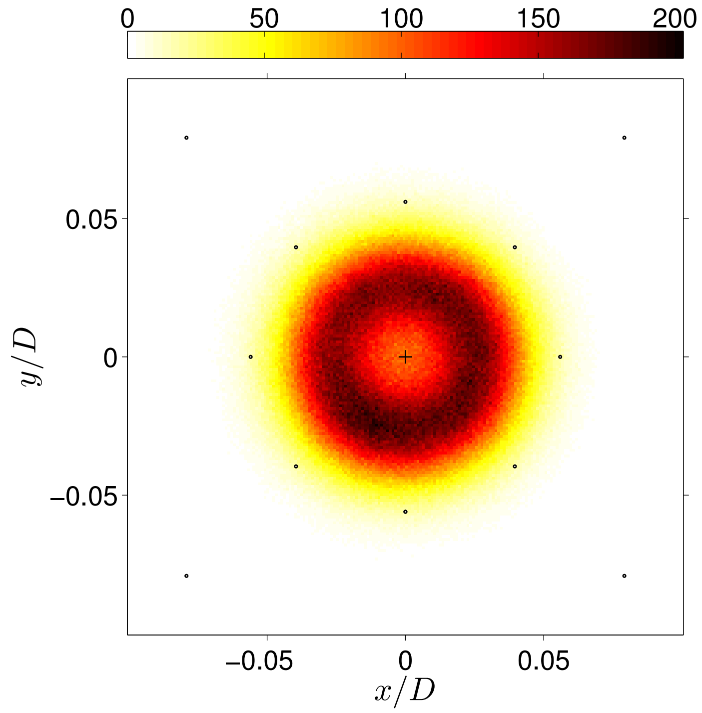

Figure 3.6.: Joint Probability density of Center-of-Pressure position.

Further information on the dynamic behaviour of the coherent structures is provided by examining the spectra of the CoP, plotted in figure 3.7. In the spectrum of the angular component, a power-law with an exponent close to -2 is obtained at very low frequencies (VLF). This is analogous to the results of Grandemange *et al.* (2013), and consistent with Brownian dynamics (Brown & Ahlers, 2006). Hence the VLF oscillation is a *random* rotation of the CoP in the azimuthal direction around the axis of the body. The spectrum of the radial component exhibits a clear peak (d) at the vortex shedding mode, $St \approx 0.2$. Below that frequency, a power-law roll-off is observed, with the radial spectral density saturating at low frequencies. This gradient change in the spectral density plotted on logarithmic scale, manifests as peak (b) in the premultiplied spectrum and coincides with the energy associated with the bubble pumping.

In order to identify the asymmetry of the flow, the mean pressure statistics were calculated in the rotating reference frame of the CoP by rotating the data based on the instantaneous angle of the CoP (Grandemange, 2013). In the rotating frame, the axisymmetry of the mean and root-mean-square pressure observed in the long-time average is lost, as shown in figure 3.8. Both distributions are characterised by reflectional symmetry and an azimuthal modulation

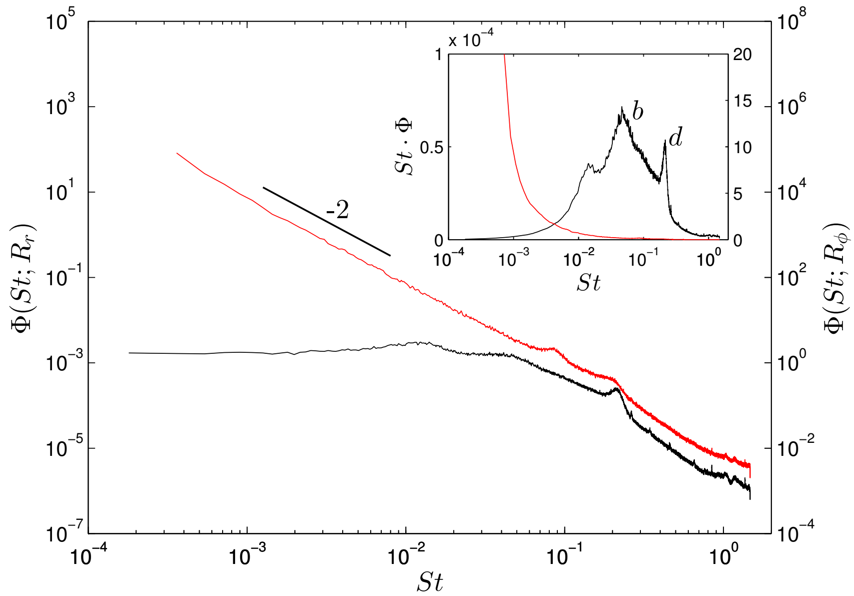

Figure 3.7.: Spectral density of Centre-of-Pressure in polar coordinates: —— , radial R_r; ——, azimuthal R_ϕ. The inset shows premultiplied spectra.

of $m = 1$. The $\mathcal{R}_\pi$ symmetry of the wake is broken: calculation of the radial distance of the CoP from the centre of the body confirms the value of $R_r = 0.03D$ found above for the mean pressure distribution.

The averaging procedure of the base pressure distribution on the rotating reference frame reveals a flow topology that resembles that of the reflectionally symmetric topology observed in the laminar wake, immediately after the second symmetry-breaking bifurcation. In this laminar regime, vortices are shed periodically off-centre of the axis creating a reflectionally symmetric distribution; the angle of the symmetry plane is constant and is determined from the initial conditions. However, for the turbulent regime, the low frequency rotation of the symmetry plane results in an axisymmetric pressure distribution on the base, see figure 3.1, due to the uniform variation in the orientation of the vortex shedding.

Therefore, the turbulent state explores a continuum of metastable symmetry-breaking patterns ($R_r \neq 0$), the angle of which is arbitrary. However, the mean value of the two-dimensional probability density lies on the centre of the body ($R_r = 0$), and the flow recovers $\mathcal{R}_\pi$ symmetry, provided the averaging is performed over sufficiently long time.

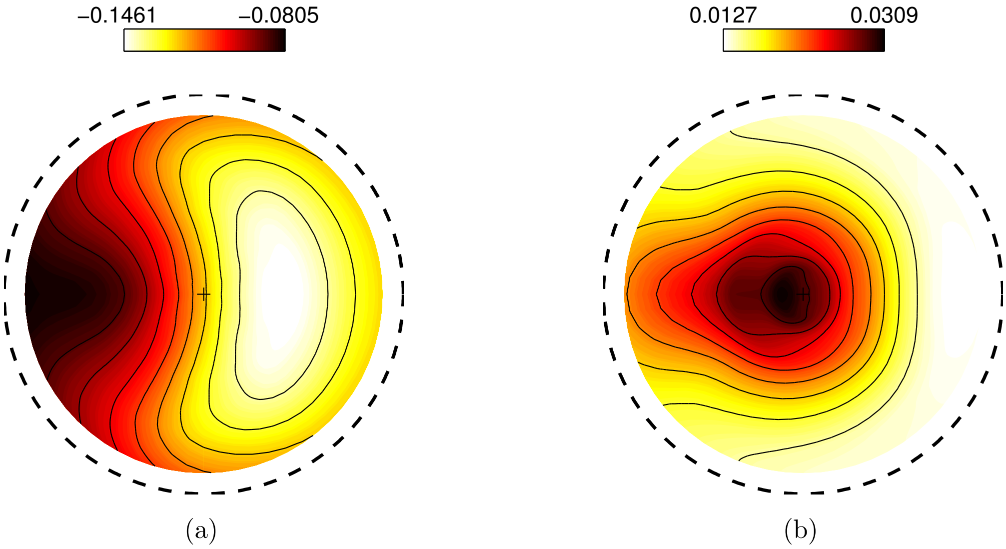

Figure 3.8.: Pressure distribution on the base of the body on the rotating reference frame of the Center-of-Pressure: (a): Mean and (b) root-mean-square.

3.3. Concluding remarks

In this chapter, the coherent structures that describe the large-scale dynamics of a turbulent three-dimensional wake have been characterised in detail from pressure measurements performed on the base of an axisymmetric bluff body.

The symmetry-breaking instabilities of the transitional wake observed at $Re_D < 1000$ (Bohorquez *et al.*, 2011; Bury & Jardin, 2012) before the chaotic regime, persist at high Reynolds numbers (here $Re_D \sim 2 \times 10^5$). Although the wake is turbulent, the large-scale coherent structures associated with it retain the structure of the laminar instabilities in a statistical sense. These are large-scale anti-symmetric oscillations with $m = \pm 1$ at a frequency of $St_D \approx 0.2$, known as vortex shedding, reminiscent of the unsteady bifurcated state observed in laminar flows.

Furthermore, the shedding is asymmetric and it is linked with an asymmetric mean pressure distribution on the base with $m = 1$, which both rotate randomly around the axis of the body at a frequency of $St_D \approx 0.002$. These distributions preserve the reflectional symmetry in the rotating reference frame, and are reminiscent of the steady bifurcated state of the laminar wake. Due to this slow rotation the turbulent wake recovers axisymmetry in the long time average.

The dynamics of these two processes impose two well-separated timescales for the evolution of the flow: a short timescale, $t \sim 5D/U_\infty$, associated with the periodic shedding of vortices and a long one, $t \sim 5 \times 10^2 D/U_\infty$, due to the variation of the shedding angle. These two timescales are in agreement with the ones found in the turbulent wake of a rectilinear three-dimensional body (Grandemange *et al.*, 2013) suggesting universal slow dynamics associated to symmetry-breaking modes of three dimensional turbulent wakes. In contrast with the rectilinear-body wake, which has two possible symmetry-breaking states (bistable wake), the axisymmetric-body wake possesses an infinite number of states depending on the azimuthal angle of shedding (multistable wake).

It is concluded that symmetry considerations are central not only to the study of transitional phenomena but also to fully developed turbulence. Although bifurcations break the symmetries on the way to turbulence, fully developed turbulence restores the possible symmetries in a statistical sense, at very high Reynolds numbers (Frisch, 1996).

4. Diffusive dynamics and stochastic models

A modelling methodology to reproduce the experimental measurements of a turbulent flow under the presence of symmetry is presented. We apply the modelling approach to a three dimensional wake-flow generated by an axisymmetric body, the dynamics of which were investigated in chapter 3.

We show that the dynamics of the turbulent wake-flow can be modelled by a nonlinear two-dimensional Langevin equation, the deterministic part of which accounts for the broken symmetries which occur at the laminar and transitional regimes at low Reynolds numbers and the stochastic part which accounts for the turbulent fluctuations. Comparison between theoretical and experimental results allows the extraction of the model parameters.

4.1. Introduction

The complete solution of a macroscopic system would consist in solving all the microscopic equations of the system (Navier-Stokes equations and boundary conditions). Because we cannot generally do this at very high Reynolds numbers we might use instead a stochastic description, i.e., we describe the system by macroscopic variables which fluctuate in a stochastic way. For a deterministic treatment, the fluctuations of the macroscopic variables is neglected.

A rigorous derivation of stochastic equations would start with microscopic description. The deterministic treatment should then follow from the stochastic treatment by neglecting the fluctuations. Such a rigorous derivation may be very complicated or even impossible. Hence, one may start with the deterministic equation and use heuristic arguments to obtain the stochastic description. In the heuristic treatment one usually adds some Langevin forces to the deterministic equations and thus obtains a stochastic differential equation (Risken, 1984).

For axisymmetric wakes, deterministic solutions (in a weakly nonlinear sense) are already known and tested at laminar regimes close to the threshold of bifurcations (Fabre *et al.*, 2008; Meliga *et al.*, 2009). The premise of using these solutions with the addition of random Langevin forces is the experimental observation that the laminar transitional instabilities (global modes) persist at high Reynods numbers and *only* those manifest as large scale structures, as shown in chapter 3. We will demonstrate that the remaining observed dynamics manifest due to the perturbation of these weakly nonlinear solutions by random noise, which accounts for the unmodelled microscopic dynamics (turbulence). Extension of this approach should be straightforward to a wide range of flows.

4.2. The model

The laminar and linearly stable axisymmetric wake loses spatial $\mathcal{R}_\pi$ symmetry in the azimuthal direction (rotation of angle π around any radial axis passing through the centre of the body) due to a supercritical pitchfork bifurcation (Fabre *et al.*, 2008; Meliga *et al.*, 2009; Bohorquez *et al.*, 2011; Bury & Jardin, 2012; Bobinski *et al.*, 2014), the normal form of which reads

$$\dot{\mathbf{x}} = \alpha\mathbf{x} + \lambda\mathbf{x}|\mathbf{x}|^2 \tag{4.1}$$

($\alpha, \lambda \in \mathbb{R},\ \lambda < 0$). Above the threshold of instability ($\alpha > 0$), (4.1) is associated with symmetry breaking since the states $\mathbf{x} = \pm(-\alpha/\lambda)^{1/2}$ are not invariant under the $\mathbf{x} \to -\mathbf{x}$ symmetry. This model can be directly obtained from the Navier-Stokes equations through a weakly nonlinear expansion around the critical bifurcating point (Meliga *et al.*, 2009) and has been used extensively for the description of laminar flows undergoing supercritical bifurcations (Drazin & Reid, 2004).

Here we extend the modelling approach to the fully turbulent regime, and we show that the derived model captures the dynamic evolution of the turbulent three-dimensional wake. This is achieved by modelling the effect of the turbulent fluctuations acting on the dynamics of the system as stochastic forcing, an approach that has been successfully applied to a wide range of turbulent flows (Sreenivasan *et al.*, 2002; de La Torre & Burguete, 2007; Brown & Ahlers, 2007). Under the stochastic modelling assumption for the turbulent background

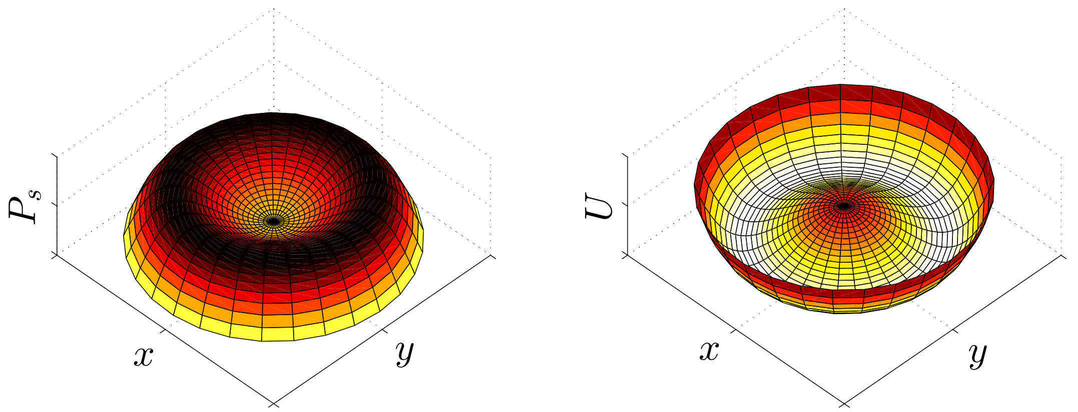

Figure 4.1.: Stationary probability density function (left) and potential (right) of the nonlinear Langevin model.

fluctuations, the deterministic system given by (4.1) with independent additive white noise in Cartesian coordinates, $\mathbf{x} = (x, y)$, becomes

$$
\begin{aligned}
\dot{x} &= \alpha x + \lambda x(x^2 + y^2) + \sigma \xi_x(t), \\
\dot{y} &= \alpha y + \lambda y(x^2 + y^2) + \sigma \xi_y(t),
\end{aligned} \tag{4.2}
$$

where ξ accounts for the random forcing of turbulence and σ^2 the variance of it. Here, $\sigma \equiv \sigma_x = \sigma_y$ and the stochastic process in (4.2) is rotationally symmetric. We transform the system from $(x, y) \to (r, \phi)$, where r is the radial distance from the centre (amplitude) and ϕ the angle (phase), using the Ito interpretation (Gardiner, 1985). In polar variables, the Langevin system given by (4.2) becomes

$$
\dot{r} = ar + \lambda r^3 + \frac{\sigma^2}{2r} + \sigma \xi_r, \quad \dot{\phi} = \frac{\sigma}{r} \xi_\phi, \tag{4.3}
$$

where $r = \sqrt{x^2 + y^2}$ and $\phi = \tan^{-1}(y/x)$. Notice that in polar variables the radial component is independent of the angular position. Details for the transformation from polar to Cartesian coordinates can be found in appendix A (see § A.4.2).

The stationary probability density function (PDF) of the above system can be found from the steady state Fokker-Planck equation and is given by

$$
P_s(r, \phi) = C \exp\left[-\frac{U(r)}{D}\right], \tag{4.4}
$$

where C is a normalization constant, $D = \sigma^2/2$ is the noise intensity and U the potential. Details for the derivation of the steady state solution of the Fokker-Planck can be found also in appendix A (see § A.4.2). The potential U is

$$U(r) = -\left[\frac{\alpha r^2}{2} + \frac{\lambda r^4}{4} + D \ln r\right]. \tag{4.5}$$

The stationary PDF for the angle is uniform, $\int_0^\infty P_s(r, \phi) dr = \frac{1}{2\pi}$. In the case of a rotationally symmetric experimental setup and inflow conditions, the drifts and diffusivities are independent of ϕ. The stationary PDF, see figure 4.1, peaks around the minimum of the Mexican-hat shaped potential.

4.3. Predictions of the model

Let $\mathbf{x}$ of equation (4.1) represent the Centre-of-Pressure (CoP) coordinates. The CoP is used as macroscopic variable quantifying the symmetry of the turbulent wake.

4.3.1. Time series and PDF

The temporal evolution and PDF of the radial and azimuthal location of the CoP for the highly turbulent regime are shown in figure 4.2. Highly erratic motion with time is observed in both components. Statistically, the wake spends most of the time in a non-zero radial location, indicating broken $\mathcal{R}_\pi$ symmetry. Due to the uniform PDF in the azimuthal location, rotational symmetry is recovered in the long time average. For the laminar regime and after the first bifurcation, which is described by equation (4.1), the stable fixed point corresponds to an non-zero CoP, the angle of which is determined from the initial conditions and is unique. During the turbulent regime, the laminar stable fixed point explores a continuum of states around its mean radial value and uniformly distributed in the angular direction: hence, the wake explores an infinite number of metastable states restoring the lost $\mathcal{R}_\pi$ symmetry.

In figure 4.2, the experimentally measured probability density function is compared to the one predicted by the model from equation (4.4). Good agreement is obtained between experimental data and model predictions. Details for the calculation of the unknown coefficients are given in section 4.3.2.

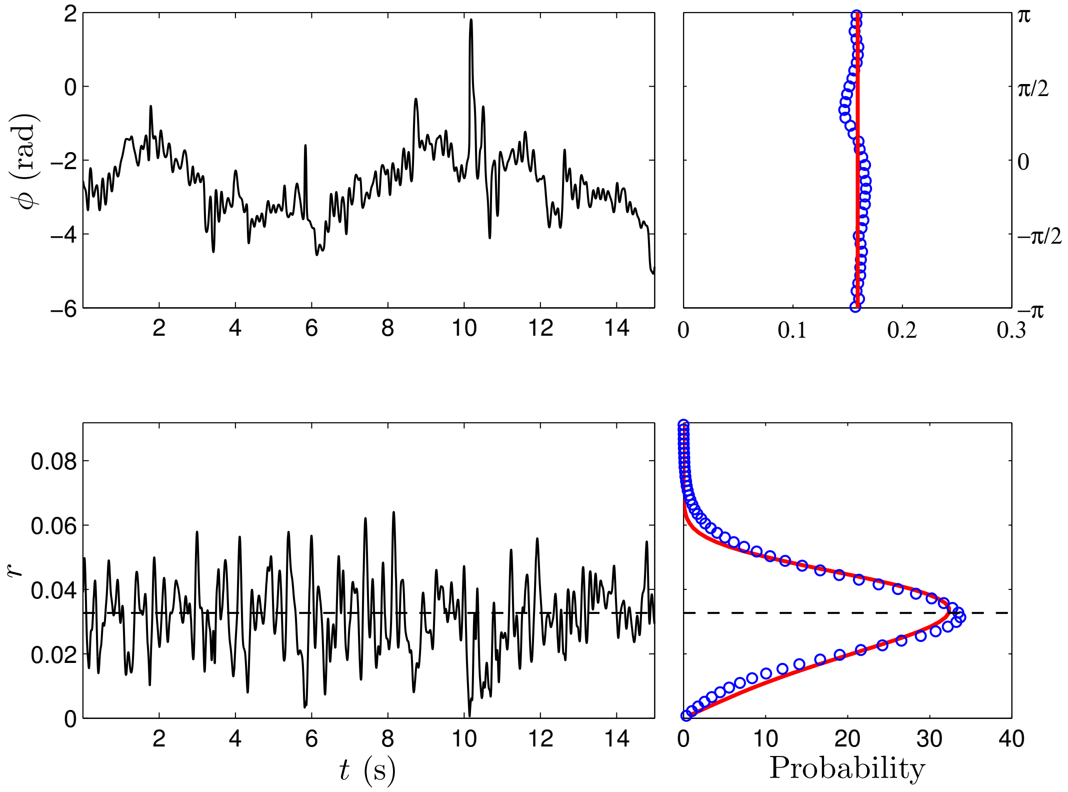

Figure 4.2.: A time series and probability density of the Centre-of-Pressure from the model: angular (upper) and radial (lower) position. Symbols in the probability density (right) correspond to experimental data and solid lines to theoretical model predictions. Dashed line: mean radial value indicating the broken $\mathcal{R}_\pi$ symmetry.

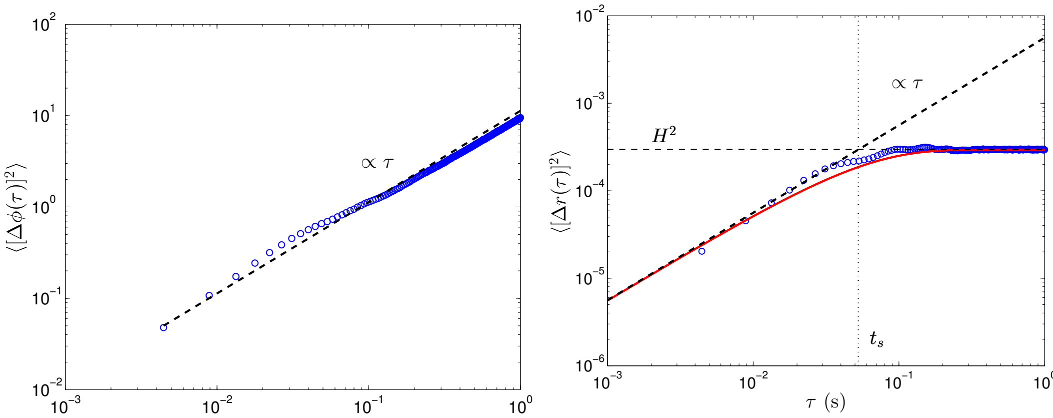

Figure 4.3.: Mean square displacement displacement as a function of the time interval τ. (a) Angular and (b) radial components of the CoP location. Symbols: experimental data. Solid line: model. Thick dashed lines: power-law fits.

4.3.2. Mean square displacement

Insight into the random dynamics of the turbulent wake is provided from the calculation of the time-averaged mean-square displacement (MSD), defined as $\langle[\Delta\mathbf{x}(\tau)]^2\rangle = \langle(\mathbf{x}(t+\tau)-\mathbf{x}(t))^2\rangle$. The experimental MSD of the angular and radial components is plotted in figure 4.3 for different sampling times. In the azimuthal direction, the MSD increases linearly with time, $\langle[\Delta\phi(\tau)]^2\rangle \propto \tau$, consistent with free diffusive motion (Einstein, 1905). In the radial direction, the linear relation holds only for short time scales below a threshold t_s, $\langle[\Delta r(\tau)]^2\rangle \propto \tau,\ \tau < t_s$, and reaches a saturation plateau at larger time scales, $\lim_{\tau\to\infty}\langle[\Delta r(\tau)]^2\rangle = H^2$.

The above results for the CoP are consistent with the predictions of the model given by equation (4.3). The coefficients of the Langevin equation α, λ and D, are obtained from the experimental MSD and PDF. The slope of the radial MSD relation is directly correlated with the diffusion coefficient, which is obtained through linear fitting, $\langle\Delta R_\tau^2\rangle = 2D\tau,\ \tau < t_s$. Knowing the diffusion coefficient D, the model coefficients α, λ are uniquely defined from (4.4) and are obtained through least-square fitting.

A physical explanation of the above results is provided by the potential well shown in figure 4.1. The turbulent wake, the state of which is quantified by the CoP, meanders in the Mexican-hat-shaped potential and explores an infinite number of states through a random walk (diffusive motion). Specifically, in the

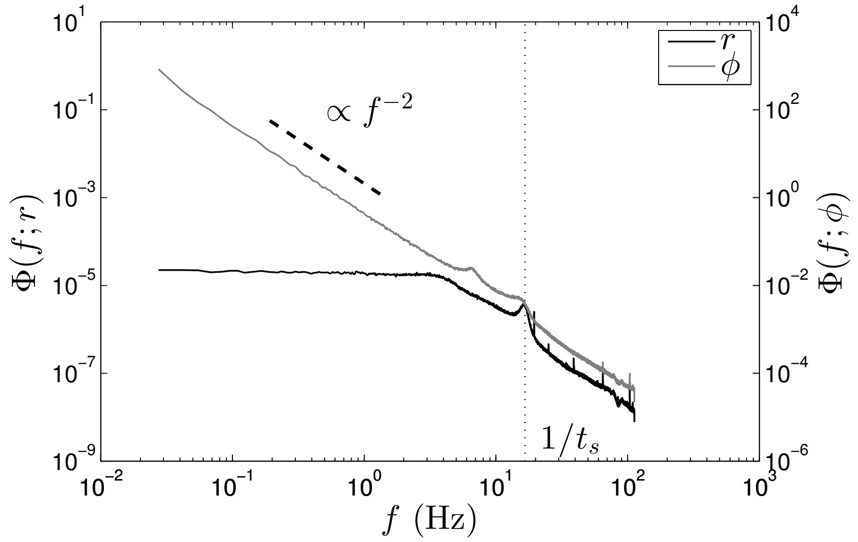

Figure 4.4.: Spectral density of the CoP location. An exponent of -2, consistent with free diffusive motion, is obtained for the azimuthal and radial components. At low frequencies, the PSD of the radial components is constant due to the spatial confinement imposed by the potential well, in accordance with the MSD results.

azimuthal direction, which determines the orientation of the wake, it can explore freely any azimuthal location resulting in unbounded reorientations. In the radial direction, the motion is restricted due to spatial constraints (confinement imposed by the potential well) resulting in a constant MSD at large timescales.

In figure 4.3 the MSD from the experimental results is plotted together with the numerically calculated MSD from the Langevin model. Direct numerical integration of equation (4.3) was performed using an Euler-Maruyama scheme. The dynamics of the CoP can be described over all the time scales from the Langevin model.

α	λ	$D = \sigma^2/2$ (s^{-1})	H^2	t_s(s)
3.81	-5604	0.0028	2.95e-4	0.0527

Table 4.1.: Coefficient values of the Langevin model obtained experimentally.

4.3.3. Power spectral density

The diffusive dynamics of the turbulent wake are also depicted in the power spectral density of the CoP, plotted in figure 4.4. The spectral density is closely related to the MSD: in general, for a power law behaviour of the MSD, $\langle[\Delta\mathbf{x}(\tau)]^2\rangle \propto \tau^\alpha$, the asymptotic form of the power spectral density is $\Phi(f) \propto f^{-(1+\alpha)}$. An exponent of -2 is observed in the spectrum of the angular component consistent with Brownian motion. A similar decay is observed for the radial component when $f > 1/t_s$. However, at low frequencies corresponding to $f \to 0$, or equivalently large timescales, it reaches a plateau and levels off, in accordance with the MSD measurements for $\tau \to \infty$.

4.3.4. Reorientations

An important feature of the axisymmetric turbulent wake is the reorientations of the symmetry plane that were addressed in chapter 3. The derived stochastic models, in combination with the experimental results provide deep insight to the characteristics of this feature.

The dynamics associated with the radial and angular motion of the CoP have been analysed independently so far. Here, the coupled dynamics predicted by the model are analysed and are linked to the dynamics of reorientations. Specifically the coupling arises as an inverse relationship between $\dot{\phi} = \Delta\phi/\Delta t$ and r for the angular component, as described by equation (4.3). The model suggests that the conditional PDF of $\dot{\phi}$ for a given r follows a Gaussian distribution with variance inversely proportional to r^2, that is

$$P(\dot{\phi}|r) = \mathcal{N}\left(0, \frac{\sigma^2}{r^2}\right) = \frac{r}{\sigma\sqrt{2\pi}}\, e^{-\frac{1}{2}\left(\frac{r\dot{\phi}}{\sigma}\right)^2}. \tag{4.6}$$

Indications of the inverse relationship can be found in the time series of the CoP in figure 4.2. One observes that for small values of the radial component, abrupt changes of the azimuthal orientation occur. The inverse relation is further validated from the joint PDF of the angular variation and radial location, $p(r, \Delta\phi)$, shown in figure 4.5, where large reorientations are more probable to occur at small radii. The conditional PDFs of the reorientations $\Delta\phi$, $p(\Delta\phi|r) = p(r, \Delta\phi)/P(r)$ collapse to a zero-mean Gaussian distribution with variance σ^2, when scaled by $1/r$ and plotted against $r\dot{\phi}$. This can be seen by multiplying each side of equation (4.6) by r:

$$\frac{P(\dot{\phi}, r)}{rP(r)} = \frac{1}{\sigma\sqrt{2\pi}}\, e^{-\frac{1}{2}\left(\frac{r\dot{\phi}}{\sigma}\right)^2}. \tag{4.7}$$

The collapse of the curves based on equation (4.7)*, confirms the inverse radial dependence of the reorientations. Most importantly the collapse on the Gaussian curve justifies also here the choice of zero mean Gaussian noise as forcing parameter, a heuristic assumption made during the formulation of the model.

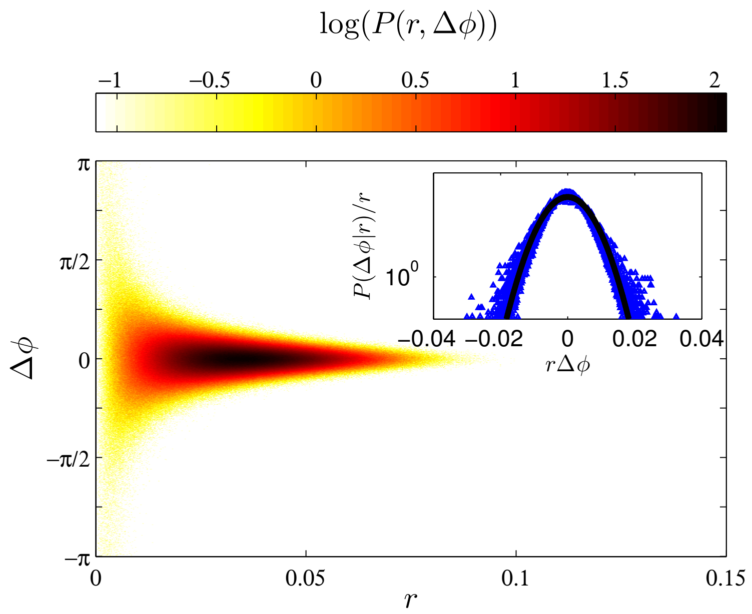

Figure 4.5.: Joint PDF of angular variation and radial position of the CoP as measured from the experiment. Inset shows the normalised probability. Data collapse on a Gaussian distribution, as described by the model.

In the limit of small radii values, $r \to 0$, angular rotations with an almost uniform PDF are observed in the joint PDF. This situation of small r corresponds to large variance and therefore a very broad Gaussian that, over the finite measurable window of $-\pi$ to π, will appear uniform. This is analogous to the cessation events observed by Brown *et al.* (2005) for the large-scales of

*Equation (4.7) can be obtained alternatively from equation (4.3) by multiplying each side with r. Then, the probability function of the product $r\dot{\phi}$ is equal to

$$P(r\dot{\phi}) = \mathcal{N}(0, \sigma^2) = \frac{1}{\sigma\sqrt{2\pi}}\, e^{-\frac{1}{2}\left(\frac{r\dot{\phi}}{\sigma}\right)^2} \tag{4.8}$$

Rayleigh-Bénard convection but can be understood without specifying arbitrary thresholds for a small r.

4.4. The physical picture

The physical picture that can be drawn for the turbulent axisymmetric wake based on the above is as follows. The laminar large scale structures, associated with spatially broken symmetries, persist at high Reynolds numbers. In the turbulent regime, these structures undergoes diffusive motion (random walk) in a two-dimensional Mexican-hat-shaped potential well, restoring statistically the broken symmetries.

Two slow diffusion timescales emerge from this process and can be described from the derived model: one associated with the free diffusion in the azimuthal direction and one with the confined diffusion in the radial direction. Specifically they are associated with the added stochastic terms $\sigma\xi$ and $\frac{\sigma}{r}\xi$ for the radial and angular components, respectively. These two timescales explain for the first time important features of the turbulent wake, which were identified in chapter 3.

The radial diffusive timescale is identified in the PSD of the CoP at a dimensional frequency f_s, and at the MSD at $t_s = 1/f_s$ Hz. In both graphs, this time scale is identified as a change of slope of each quantity, when plotted on a log-log plot, due to the spatial constraints in the radial direction. If expressed as Strouhal number, it gives $St \approx 0.05$ which is close to the frequency of the "bubble pumping" mode. In the premultiplied CoP spectra, see figure 3.7, it is associated with a broad region of energy around that frequency.

The same conclusions can be drawn for the angular component. However the motion in the azimuthal direction is not restricted by spatial constraints and all the time scales can be explored in this direction. The average time scale is given given by the diffusion coefficient $1/D$.

4.5. Concluding remarks

In this chapter it was shown that turbulent dynamics can be described by deterministic equations derived from symmetry arguments with stochastic forcing terms that give rise to turbulent behaviour. The spatial dynamics of a turbulent axisymmetric-body wake have been addressed and modelled using a simple nonlinear and stochastic model. The model consists of two coupled stochastic differential equations, the deterministic part of which accounts for the spatial broken symmetries observed in the laminar regime and gives rise to large scale structures, and the stochastic part that models in a phenomenological sense the turbulence fluctuations acting on the large scale structures.

The model shows good agreement with the experimental observations and is able to capture important quantities (mean square displacement, probability density function, power spectral density) of macroscopic variables and dynamics. The dynamics are associated with VLF reorientations of the wake in the azimuthal direction and oscillations in the radial direction. The latter explains and predict the origin of a well-reported mode in three-dimensional wake flows known as 'bubble pumping'.

The diffusive dynamics of the large scale structures presented here and in chapter 3 show striking similarities with the diffusive dynamics of the large-scale circulation observed in the turbulent Rayleigh-Bénard convection (Brown *et al.*, 2005) and the turbulent von Kármán swirling flow (de La Torre & Burguete, 2007). However, this is not surprising if somebody accounts for the symmetries of the problem: rotational symmetry which is broken en route to turbulence.

5. The forced axisymmetric bluff-body wake

In this chapter, the effect of flow-forcing using axisymmetric ZNMF slot jet actuation on the predominant modes present in the unforced flow is examined. Measurements to characterise the forced flow were obtained in the form of pressure on the base of the model, both mean and fluctuating.

5.1. Flow response to forcing

The turbulent wake was excited driving the ZNMF actuator with a harmonic voltage signal, $v_{in} = |v_{in}| \sin(2\pi f t)$. A wide range of forcing amplitudes and frequencies was explored during the experiments and the results are presented here.

The unforced wake has been characterised in chapter 3 using the pressure obtained from the 64 static pressure taps. Here the analysis is performed also based on the 8 Endevco pressure transducers measurements. See appendix B for a discussion of the observable modal dynamics from the Endevco transducers. These sensors, as discussed in § 2.3, are ideal for implementing in feedback control schemes in real-time. The results presented here are precursory results for feedback control strategies and the characterisation of the forced wake response based on these sensors is necessary.

5.1.1. Vortex shedding response

The forced spectra of the azimuthally decomposed base pressure were inspected for changes and they were compared to the unforced ones. During all forcing conditions, the flow responds at the forcing wavenumber, $m_f = 0$, and frequency ω_f, as expected in a linear framework. In the base pressure spectra, a sharp peak appears in the $m = 0$ mode. However, a pronounced change is

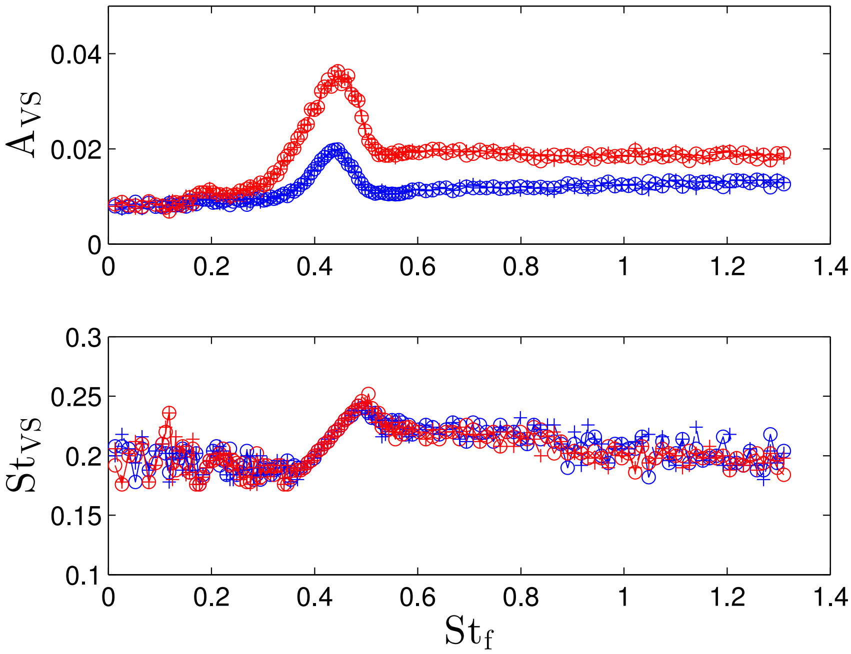

Figure 5.1.: The response of the amplitude and frequency of the $|m| = 1$ global vortex shedding mode to axisymmetric forcing ($m = 0$) at different forcing frequencies.

also observed in the spectra of the $m = \pm 1$ mode, near $St = 0.2$, which coincides with the frequency of the global vortex shedding mode as identified in figure 3.2. This behaviour is indicative of the inherent nonlinearity of the fluid system. The steady-state amplitude and frequency response of the $m = \pm 1$ global mode to axisymmetric forcing over different forcing frequencies and amplitudes are shown in figure 5.1. The amplitude of the vortex shedding mode was estimated by integrating the $m = \pm 1$ pressure spectra around the frequency of the shedding mode (St_{VS}, $\Delta St = 0.04$), that is

$$A_{VS}^2 = \int_{f_{VS-\Delta f}}^{f_{VS+\Delta f}} \Phi_m(f)\,\mathrm{d}f, \quad m = \pm 1. \tag{5.1}$$

Due to the fact that the frequency of the shedding mode varies depending on the forcing amplitude and frequency, its frequency was estimated as the frequency of the maximum amplitude close to $St = 0.2$.

The amplitude response is indistinguishable for the $m = +1$ and $m = -1$ modes at the VS frequency, meaning $A_{VS} \equiv A_{VS_+} = A_{VS_-}$ for the entire frequency and amplitude range of the forcing. Since the amplitudes of the two counte-rotating decomposed waves is the same, it is concluded that the shedding mode is a standing wave.

5.1.2. Parametric subharmonic resonance

A strong resonance in the response occurs when the forcing is close to twice the global mode frequency, $St \approx 2St_{VS} = 0.4$, as shown in figure 5.1. Near this forcing frequency, the frequency of the global mode "locks-in" to one-half the forcing frequency, as shown in the same graph. The lock-in region depends on the forcing amplitude; increasing amplitude results in a wider lock-in region. Similar frequency "lock-in" behaviour was found by Kim & Durbin (1988) in the wake of a sphere under acoustic excitation for Reynolds number 3700. In their experiments, the shedding frequency also locked-in to one-half the forcing frequency, with no such effect when forcing near to the shedding frequency. Also, Bigger *et al.* (2009) examined the forced wake of a disk under helical and symmetric actuation, finding that the most effective frequency to reduce the length of the recirculation zone corresponds to the natural shedding frequency and twice that, for the two types of actuation, respectively.

"Lock-in" phenomena point to nonlinear oscillator behaviour forcing past a suspected global-mode frequency or its rational multiples (Huerre & Monkewitz, 1990). Hence, a nonlinear coupling between the forcing ($m = 0$) and the global ($|m| = 1$) modes must exist.

The results show that the dominant interaction is a parametric resonance mechanism between the fundamental forcing and the subharmonic modes which leads to a pronounced growth of the subharmonic. This parametric subharmonic instability (PSI), is a resonant wave-triad interaction characterised by transfer of energy from a parent wave to two daughter waves of half frequency and higher wavenumber (Craik, 1988). The resonant conditions are

$$m_f = m_{VS}^{+} + m_{VS}^{-}, \tag{5.2a}$$

$$\omega_f = \omega_{VS}^{+} + \omega_{VS}^{-}. \tag{5.2b}$$

The above spatial and temporal resonace conditions are met here since $m_f = +1 + (-1) = 0$ and $St_f = 0.2 + 0.2 = 0.4$.

The resonant interaction between axisymmetric forcing and antisymmetric vortex shedding is depicted in the spectra of the decomposed pressure in fig-

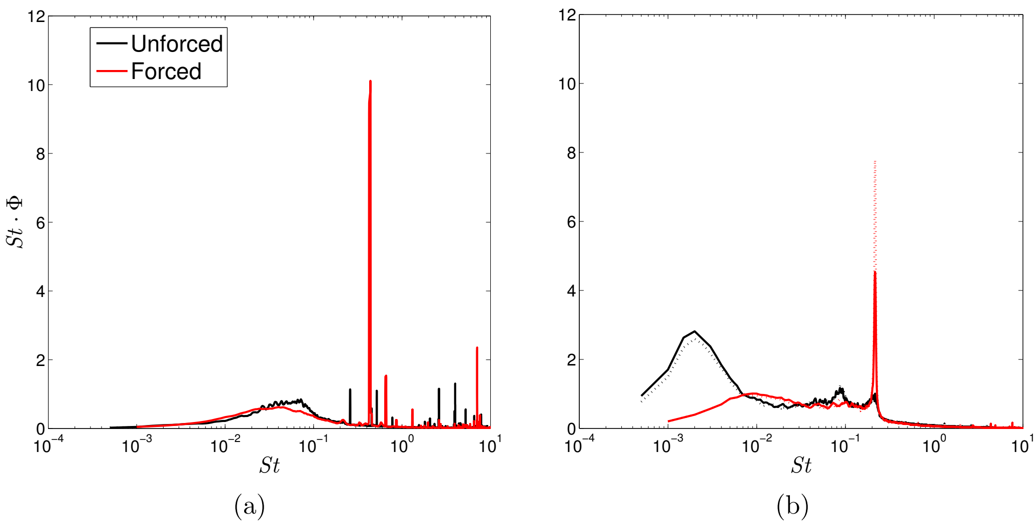

Figure 5.2.: The effect of axisymmetric forcing at $St_f = 2St_{VS} = 0.4$ on the spectra of $m = 0$ (a) and $m = \pm 1$ (b) modes, showing parametric subharmonic resonance in $m = \pm 1$.

ure 5.2, where the results of a specific forcing frequency and amplitude are presented. Forcing at a frequency of 0.4, the spectra of the pressure are dominated by the linear response of the axisymmetric mode at the forcing frequency ($St = 0.4$) and the nonlinear subharmonic response of the global mode at half the forcing frequency ($St = 0.2$). Interestingly, all the other spectral peaks observed in the unforced case have been suppressed except the broadband axisymmetric mode at $St \approx 0.06$, “bubble pumping mode”, which is still present at the base pressure measurements. The suppressed modes of the wake are the VLF mode ($St \approx 0.002$) and the subharmonic of the VS mode ($St \approx 0.1$), both appearing at $m = \pm 1$.

The amplitude and frequency response of the vortex shedding mode, as a function of the forcing amplitude u_{jet}, are shown in figure 5.3. The response of the shedding amplitude for a fixed forcing frequency follows a non-linear trend as the forcing amplitude increases. Also, at low forcing amplitudes the shedding mode appears to be insensitive to forcing, meaning that a minimum forcing amplitude is required to excite parametrically the VS. This threshold, when forcing at $St_f = 0.4$, is $U_{jet} \approx 0.05U_\infty$. The same forcing amplitude threshold exists in order to lock in the frequency of the VS mode.

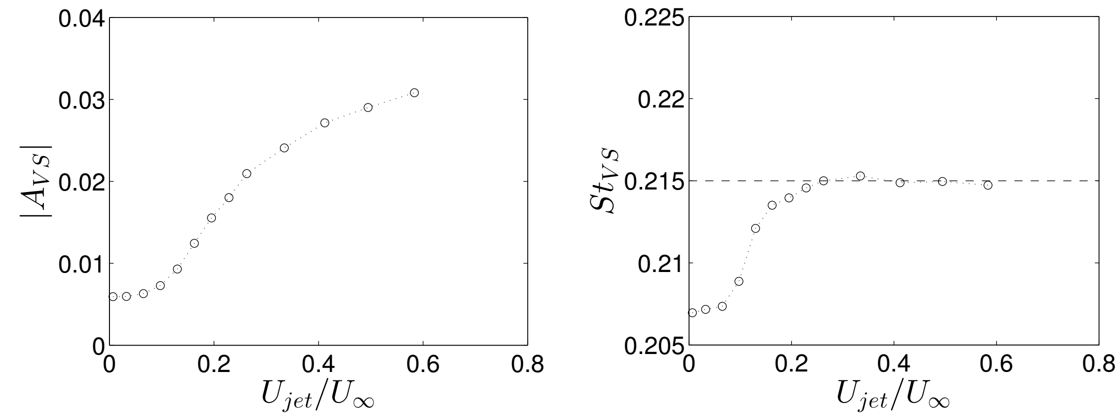

Figure 5.3.: Steady-state response of the global vortex shedding mode to ZNMF forcing with azimuthal wavenumber $m = 0$ and frequency close to twice the global mode frequency; amplitude (left) and frequency (right).

5.1.3. Mean base pressure

During the subharmonic resonant forcing of the vortex shedding mode, it was shown that an increase in the forcing amplitude is associated with an increase of the vortex shedding amplitude. This trend was found to be associated with a decrease of the area-weighted mean base pressure. The mean base pressure (area-weighted and time-averaged pressure coefficient) is defined as

$$\overline{P} = \frac{1}{T}\frac{1}{A}\int\int\int p(r,\phi,t)r\ drd\phi dt, \tag{5.3}$$

where T is the duration of averaging and A the area of the base of the body.

The steady state mean base pressure response is shown is figure 5.4 obtained from the 64 static taps. An almost linear decrease is observed as a function of the control parameter (u_{jet}) and thus the form drag exerted on the axisymmetric body increases. It follows that the mean pressure increases due to the amplification of the vortex shedding mode.

Also here the same forcing amplitude threshold has to be reached in order to achieve a decrease in the mean base pressure coefficient.

5.1.4. Symmetries of the forced flow

Here the symmetry of the flow is examined during the PSI. A similar analysis to the one applied for the unforced case is applied and the results are compared.

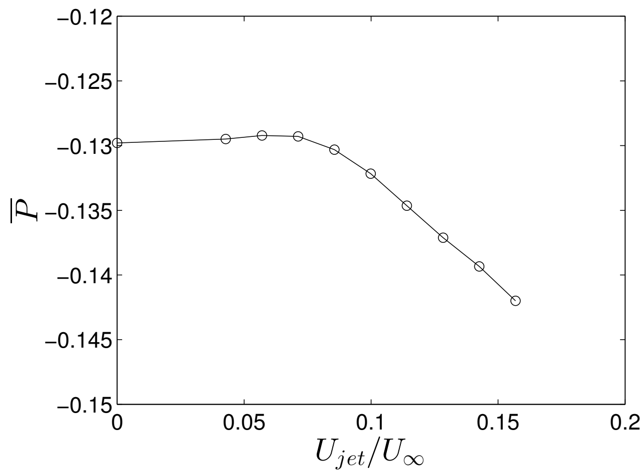

Figure 5.4.: Mean base pressure coefficient as a function of the forcing amplitude for the subharmonic resonance case ($St_f = 2St_{vs}$, $m_f = 0$).

The mean and rms pressure distributions on the base of the body for the forced case are shown in figure 5.5. Both distributions have an $m = 1$-like shape and are reflectionally symmetric. For the forced case, the rotational symmetry observed during the unforced case is broken. The shapes of the distributions are similar to the ones found for the unforced flow on the rotating reference frame of the CoP.

Further insight into the symmetry of the flow is obtained from the CoP. Time series of the radial and angular components of the CoP over a short time period are shown in figure 5.6. Also, in the same figure the corresponding PDFs calculated from a long time sample are plotted. Similar to the unforced case, the radial component is non-zero indicating broken rotational symmetry for a fixed angle of the symmetry plane. However, in contrast to the unforced case for which the angular component is uniformly distributed in the range $[-\pi, \pi]$, the forced wake shows a preference to a specific angular position. The preferred angle for the present set of experimental measurements was found to be approximately $-130°$ and remained constant during the measurements.

The joint PDF is shown in figure 5.7. In accordance with the mean pressure distribution, the rotational symmetry observed in the unforced case is lost. The joint PDF has a circular shape centred off-axis of the body. The azimuthal location of the symmetry plane is fixed on the base of the body, compared to the uniform distribution of it for the unforced case. The suppression of the random variation due to the forcing is confirmed from the pressure spectra of

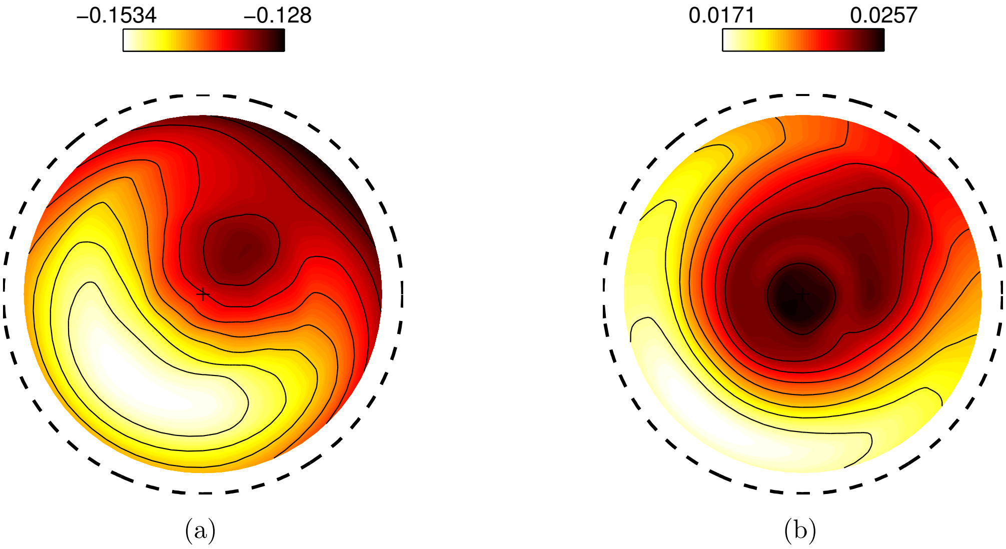

Figure 5.5.: Pressure distribution on the base of the body: (a) mean and (b) root-mean-square for the forced case ($St_f = 2St_{vs}$, $m_f = 0$).

the $m = 1$ mode, see figure 5.2.

It is concluded that axisymmetric resonant forcing locks the symmetry plane in a fixed angle and the wake does not explore an infinite number of azimuthal angles in order to restore the rotational symmetry.

Interestingly, similar symmetry properties were observed for all the other forcing frequencies where ω_f is not close to $2\omega_{VS}$. This has been observed by Oxlade (2013) examining the high-frequency forcing of the axisymmetric bluff body wake.

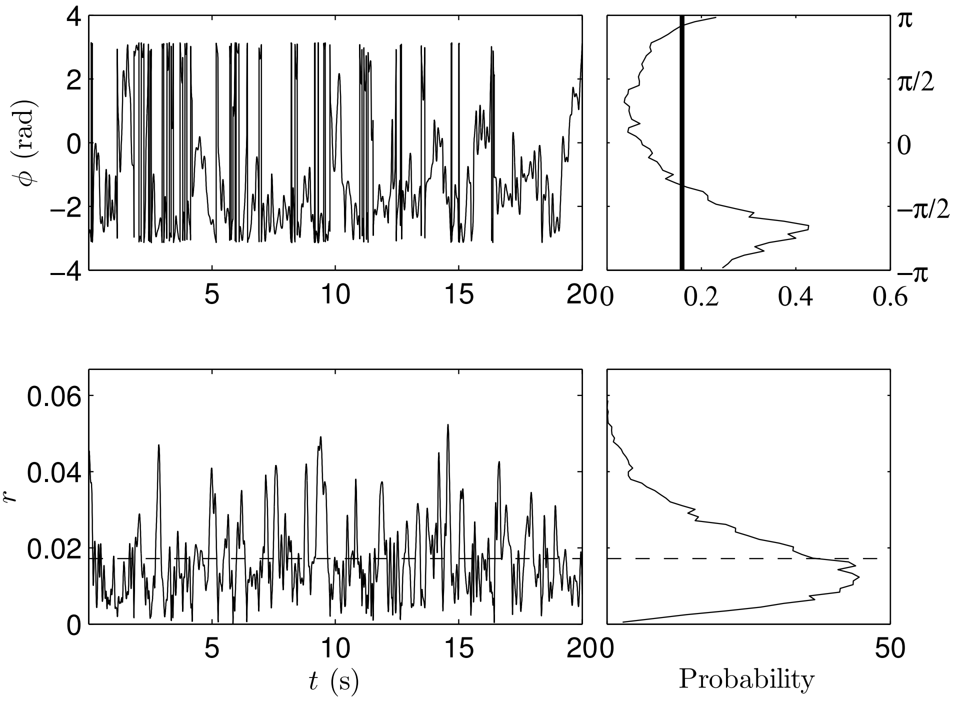

Figure 5.6.: A time series (short sample) and probability density (long sample) of the Centre-of-Pressure. Radial (lower) and azimuthal (upper) positions.

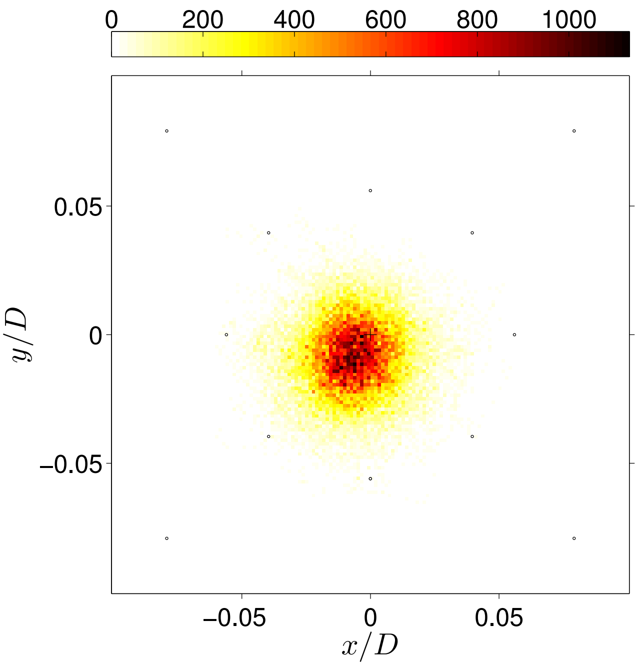

Figure 5.7.: Joint Probability density of Center-of-Pressure position.

5.2. Concluding remarks

In this chapter, the forced response of the turbulent wake behind an axisymmetric bluff-body was examined through experiments. Forcing was applied using axisymmetric ZNMF actuation located on the base of the body. It was shown that axisymmetric forcing couples non-linearly with the global shedding mode, with azimuthal wavenumbers $m = \pm 1$ and frequency $St \approx 0.2$, with this coupling being the main factor that determines the nonlinear flowfield response.

The nonlinear nature of the mechanism arises from the coupling between waves of different azimuthal wavenumbers and frequencies, which form wave triads. The dominant interaction is a parametric resonance mechanism between the forcing and the global shedding mode, when forcing is applied close to twice the shedding frequency, termed *Parametric Subharmonic Instability*. At these forcing conditions, a pronounced growth of the shedding mode amplitude was observed, simultaneously with a frequency lock in to half the forcing frequency. That reveals a nonlinear mechanism that allows the frequency of the global shedding mode to be controlled through forcing. The response of the shedding amplitude at the PSI region was found to increase approximately quadratically as a function of the forcing amplitude, whereas the mean base pressure decreased almost linearly.

The symmetry of the wake changes when forcing is applied. When the PSI conditions are met, the mean and rms pressure distributions on the base of the body are characterised by reflectional symmetry due to the fixation of the symmetry plane at a constant angular position.

The subharmonic of the global mode, and the very low frequency rotation which were present in the unforced spectra are suppressed on applying forcing. It is concluded that any mathematical attempt to predict the effect of forcing on the flowfield must retain at least the global $m = \pm 1$ modes, along with their coupling with the axisymmetric $m = 0$ forcing.

6. Weakly nonlinear modelling of the forced flow

In this chapter, amplitude equations governing the forced amplitude evolution of the vortex shedding global mode of the turbulent flow for the turbulent axisymmetric wake are derived. The analysis is based on the weakly nonlinear analysis proposed by Sipp (2012), in which the forcing enters the amplitude equations. The analysis is extended in the turbulent flow and the model coefficients are obtained from experimental results. We find that the derived model can accurately describe the forced response of vortex shedding mode.

6.1. Dynamic modelling of vortex shedding

We consider the flow behind the axisymmetric bluff-body. The governing equations are the incompressible Navier-Stokes equations

$$\mathbf{u}_t + \mathbf{u} \cdot \nabla \mathbf{u} = -\nabla p + \mathrm{Re}^{-1} \nabla^2 \mathbf{u} \quad \text{and} \quad \nabla \cdot \mathbf{u} = 0, \tag{6.1}$$

with $Re = U_\infty D/\nu$, $\mathbf{u} = (u, v, w)$ the velocity vector of the radial, azimuthal and streamwise components in the cylindrical coordinate system $\mathbf{x} = (r, \phi, z)$ and p the pressure.

6.1.1. Flow decomposition

For a large departure from criticality, where $Re \gg 1$, the separating boundary layer and the near wake are turbulent resulting in the generation of small scale incoherent motion in localised regions in space and time. Since the near-wake turbulent flow contains structures of widely varying time and length scales, which may interact despite their large scale separation, we consider a model employing scale subdivision with the large scales accounting for the coherent structures and the small scales involving the incoherent background. Then, the instantaneous flow quantities $\mathbf{q} = (\mathbf{u}, p)^T$ can be decomposed as:

$$\mathbf{q}(x,t) = \mathbf{q_0}(\mathbf{x}) + \tilde{\mathbf{q}}(\mathbf{x},t) + \mathbf{q}'(\mathbf{x},t), \tag{6.2}$$

where $\mathbf{q_0}$ is a laminar base flow at Re_c, $\tilde{\mathbf{q}}$ the contribution of the quasi-periodic modes (coherent part) and $\mathbf{q}'$ the turbulence (incoherent part). The base flow modifications due to departure from Re_c and the nonlinear interactions of the waves are given from the mean component of the coherent wave whereas the turbulence is considered of random nature with zero mean. The time-independent base flow is a steady solution of the Navier-Stokes equations at $Re = Re_c$:

$$\mathbf{u_0} \cdot \nabla \mathbf{u_0} + \nabla p_0 - \frac{1}{Re_c} \Delta \mathbf{u_0} = 0 \quad \text{and} \quad \nabla \cdot \mathbf{u_0} = 0. \tag{6.3}$$

We define time averaged and the phase averaged quantities as

$$\bar{\mathbf{q}}(x) = \lim_{T \to \infty} \frac{1}{T} \int_0^T \mathbf{q}(x,t)\, dt \quad \text{and} \quad \langle\, \mathbf{q}(x,t)\, \rangle = \lim_{N \to \infty} \frac{1}{N} \sum_{n=0}^{N} \mathbf{q}(x, t + n\tau)\, d\tau \tag{6.4}$$

with τ being the period of the waves (here vortex shedding mode). Applying (6.4), the time and phase averaged flow quantities are:

$$\bar{\mathbf{q}}(x,t) = \mathbf{q_0}(\mathbf{x}) + \bar{\tilde{\mathbf{q}}}(\mathbf{x},t), \tag{6.5}$$

$$\langle \mathbf{q}(x,t) \rangle = \mathbf{q_0}(\mathbf{x}) + \tilde{\mathbf{q}}(\mathbf{x},t). \tag{6.6}$$

Both averaging operations remove the incoherent contribution of turbulence. Then the mean flow is given as the superposition of a laminar base flow and the mean flow modification of the coherent waves.

6.1.2. Governing equations for the turbulent flow

Substituting (6.2) into (6.1) and phase averaging, one finds the following equations:

$$\tilde{\mathbf{u}}_t + (\mathbf{u_0} + \tilde{\mathbf{u}}) \cdot \nabla (\mathbf{u_0} + \tilde{\mathbf{u}}) + \nabla (p_0 + \tilde{p}) - \frac{1}{Re} \Delta (\mathbf{u_0} + \tilde{\mathbf{u}}) = -\nabla \cdot \langle \mathbf{u}'\mathbf{u}' \rangle. \tag{6.7}$$

Or equivalently:

$$\langle \mathbf{u}_t \rangle + \langle \mathbf{u} \rangle \cdot \nabla \langle \mathbf{u} \rangle + \nabla \langle p \rangle - \frac{1}{Re} \Delta \langle \mathbf{u} \rangle = -\nabla \cdot \langle \mathbf{u}' \mathbf{u}' \rangle. \tag{6.8}$$

The right hand side term of equation (6.8) involves the contribution of the Reynolds stress of the phase-averaged random turbulence. For laminar flows which are close to the threshold of the instability, the amplitude evolution of the unstable global modes (coherent waves in the turbulent case) can be approximated using a weakly nonlinear expansion (Meliga *et al.*, 2009); in this case $\mathbf{u}' \equiv 0$ since the flow is laminar.

The phase-averaged form of the Navier-Stokes equations cannot by themselves determine the phase-averaged quantities; one must also provide a relation between the random fluctuating and averaged quantities. The weakly nonlinear analysis can be extended also in the turbulent flow introducing an eddy viscosity closure for the incoherent Reynolds stresses:

$$\langle \mathbf{u}' \mathbf{u}' \rangle = -\nu_t \nabla (\mathbf{u_0} + \tilde{\mathbf{u}}) \tag{6.9}$$

Also, a time-averaging of equation (6.9) gives

$$\overline{\mathbf{u}' \mathbf{u}'} = -\nu_t \nabla \bar{\mathbf{u}} \tag{6.10}$$

Under this assumption, equation (6.8) becomes:

$$\langle \mathbf{u}_t \rangle + \langle \mathbf{u} \rangle \cdot \nabla \langle \mathbf{u} \rangle + \nabla \langle p \rangle - \frac{1}{Re_T} \Delta \langle \mathbf{u} \rangle = 0. \tag{6.11}$$

Here, $Re_T = (U_\infty D)/(\nu + \nu_t)$, where ν is the kinematic viscosity and ν_t a turbulent eddy viscosity. We expect that the eddy viscosity will be much greater than the kinematic viscosity since turbulence enhances diffusion.

6.1.3. Weakly nonlinear analysis

The turbulent wake exhibits global modes with azimuthal wavenumbers $+1$ and -1. It therefore has at least a pair of complex eigenvalues with azimuthal wavenumbers $+1$ and -1, which manifest as organized waves in the turbulent flow. In the present analysis, we are focused on deriving the response of the global unsteady shedding mode to external forcing. The weakly nonlinear analysis can be applied to derive the amplitude equations of the unstable modes. For this, we follow the analysis proposed by Sipp (2012) for the laminar open-cavity flow but now for the three dimensional turbulent wake.

The departure from the critical Reynolds number, Re_c, where the stability is lost, can be expressed as:

$$\frac{1}{Re_T} = \frac{1}{Re_c + \Delta Re} = \frac{1}{Re_c}\left(1 - \frac{\Delta Re}{Re_c} + \ldots\right). \tag{6.12}$$

Assuming that the turbulent Reynolds number is close and slightly above the critical one, we can write

$$\mathrm{Re}_T^{-1} = \mathrm{Re}_c^{-1} - \varepsilon. \tag{6.13}$$

We introduce a *fast* time scale t and a *slow* time scale $t_1 = \varepsilon t$. Then, the turbulent phase-averaged field $\langle \mathbf{q} \rangle$ can be expanded around the laminar base flow at criticality as

$$\langle \mathbf{q} \rangle(t, t1) = \mathbf{q_0} + \sqrt{\varepsilon}^1 \tilde{\mathbf{q}}_1(t, t1) + \sqrt{\varepsilon}^2 \tilde{\mathbf{q}}_2(t, t1) + \sqrt{\varepsilon}^3 \tilde{\mathbf{q}}_3(t, t1) + \cdots \tag{6.14}$$

Introducing (6.13) and (6.14) into (6.11), and equating coefficients of the nth power of $\sqrt{\varepsilon}$ to zero, a series of equations is obtained at various orders (see appendix C).

For non-resonant forcing at order $\sqrt{\varepsilon}$, the solution of the equations is sought in the form

$$\tilde{\mathbf{q}}_1 = A_+ e^{i\theta} e^{i\omega_c t} \tilde{\mathbf{q}}_1^A + A_- e^{-i\theta} e^{i\omega_c t} \tilde{\mathbf{q}}_1^A + E e^{i\omega_f t} \tilde{\mathbf{q}}_1^E + c.c. \tag{6.15}$$

and consists of the superposition of the global mode and the forcing response, with amplitudes $A_\pm = A_+ = A_-$ and E and spatial structures $q_1^A = q_1^A(r, z)$ and $q_1^E = q_1^E(r, z)$, respectively. At order $\sqrt{\varepsilon}^3$, compatibility conditions have to be imposed for the solvability of the equations, which yield the following equation governing the complex amplitude $A_\pm$ of the global mode:

$$\frac{dA_\pm}{dt} = \alpha A_\pm + \lambda |A_\pm|^2 A_\pm + g(A_\pm, E) \tag{6.16}$$

where the function g contains all the secular terms that stem from the interaction of the global mode with the forcing at third order. In the absence of external forcing, the function g is zero.

When ω_f is close to twice the global shedding mode frequency, we have seen in figure 5.2 that the flow responds significantly in azimuthal wavenumber $|m| = 1$ at half the forcing frequency, due to the parametric subharmonic instability. Thus forcing at frequencies close to twice the shedding frequency (i.e. $St \approx 0.4$) will be termed "resonant forcing". For resonant forcing, we have the superimposition of two counter-rotating spiralling modes (standing wave) of same amplitude $A_\pm$, and (6.16) has the following form:

$$\frac{dA_\pm}{dt} = \alpha A_\pm + \lambda |A_\pm|^2 A_\pm + \mu E A_\pm^*. \tag{6.17}$$

The last term in eq. (6.17) results from the nonlinear coupling between the conjugate of the global mode $A_\pm^*$ and the axisymmetric perturbation E, when forcing is applied resonantly near twice the global mode frequency.

6.1.4. Mean flow

For an arbitrary Reynolds number of the flow, the mean turbulent flow is given by a time-average of the phase-avergaed equation (6.8). That is

$$\bar{\mathbf{u}} \cdot \nabla \bar{\mathbf{u}} + \nabla \bar{p} - \Delta \bar{\mathbf{u}}/Re = -\nabla \cdot \overline{\mathbf{u}'\mathbf{u}'} \tag{6.18}$$

The right-hand side of the mean equation contains the mean contribution of the Reynolds stresses of the turbulence (random structures). Using the eddy viscosity closure, see equation (6.10), the mean flow equation is

$$\bar{\mathbf{u}} \cdot \nabla \bar{\mathbf{u}} + \nabla \bar{p} - \Delta \bar{\mathbf{u}}/Re_T = 0. \tag{6.19}$$

In the conceptual model proposed here, the mean flow is viewed as the nonlinear modification of the laminar base flow due to the action of the nonlinear Reynolds stresses for $Re > Re_c$. The mean flow modification of the laminar base flow due to the coherent waves arising due to the nonlinear interaction of the coherent waves stemming from $\nabla \cdot \overline{\tilde{\mathbf{u}}\tilde{\mathbf{u}}}$, is taken explicitly into account through the weakly nonlinear expansion up to second order. The nonlinear modification due to the random turbulence due to $\nabla \cdot \overline{\mathbf{u}'\mathbf{u}'}$ is modelled through the eddy viscosity.

Based on the weakly nonlinear analysis, the mean flow is given by the steady part of equation (C.31). That is

$$\overline{\mathbf{q}} = \mathbf{q}_0 + \varepsilon\left(\delta\mathbf{q}_2^1 + |A_\pm|^2\mathbf{q}_2^{|A_\pm|^2}\right). \tag{6.20}$$

This description provides the global mean flow. It consists of the superposition of the laminar base flow $\mathbf{q}_0$ at Re_c, the modification of it due to the departure from criticality $\delta\mathbf{q}_2^1$, and the second order nonlinear modification due to the unstable modes $|A_\pm|^2\mathbf{q}_2^{|A_\pm|^2}$. Substitution of the amplitude of the global mode given by (6.17), gives the response of the mean flow as a function of the forcing amplitude $|E|$ and the departure from criticality ε, that is

$$\overline{\mathbf{q}} = \mathbf{q}_0 + \varepsilon\left(\delta\mathbf{q}_2^1 - \frac{\alpha_r + \mu_r|E|}{\lambda_r}\mathbf{q}_2^{|A|^2}\right). \tag{6.21}$$

For a fixed departure from criticality, the above equation can be used to describe the response of the mean flow as a function of the forcing amplitude for the PSI when forcing is applied exactly at twice the critical frequency. It has to be noticed that for the PSI, based on the weakly nonlinear analysis, although the steady state amplitude of the global mode varies quadratically as a function of the forcing amplitude, the mean flow varies linearly.

6.2. Identification of model parameters

In order to identify the unknown complex parameters, α, α and μ, in equation (6.17), further forced experiments are performed. The system is subject to harmonic excitation, modelled through the forcing term E, and the transient and steady-state response of the unsteady global mode $A_\pm$ is measured to verify equation (6.17) and identify the unknown complex parameters. The non-dimensional centreline velocity of the jet output is used to quantify the forcing amplitude E, that is $E = U_{jet}/U_\infty$.

Substituting $A_\pm = |A_\pm|e^{i\omega t}$ and $E = |E|e^{i\omega_f t}$, for $\omega_f = 2\omega_c$, yields the following equations for the modulus and phase of the unsteady global mode:

$$\frac{1}{|A_\pm|}\frac{d|A_\pm|}{dt} = \alpha_r + \lambda_r|A_\pm|^2 + \mu_r|E| \tag{6.22a}$$

$$\omega = \frac{d\phi}{dt} = \alpha_i + \lambda_i|A_\pm|^2 + \mu_i|E| \tag{6.22b}$$

where $\phi = \omega t = 2\pi f t$. Notice the above set of equations is valid when the forcing frequency is exactly twice the critical frequency*. Instantaneous growth rates and frequencies of the response $A_\pm$ are obtained experimentally using the following procedure:

- The measured pressure signals on the base of the body are decomposed in the azimuthal direction using to obtain the first azimuthal Fourier components.
- The signal is then filtered in the spectral domain with a window centered on the frequency of the vortex shedding mode.
- The instantaneous complex amplitude $(A_r + A_i)(t)$ of the filtered signal is built from the Hilbert transform.
- Then, the instantaneous amplitude and phase are given by $|A| = \sqrt{A_r^2 + A_i^2}$ and $\phi = \tan^{-1}(A_r/A_i)$.
- The growth rate $d|A_\pm|/dt$ and frequency ω are calculated differentiating in time the instantaneous amplitude and phase. Time derivatives are evaluated by finite differences.

A similar procedure to the one described above for the identification of the Landau coefficients has been applied close to the threshold of bifurcation for the velocity signal in the wake of a cylinder (Schumm *et al.*, 1994). When transients are contaminated by noise, the instantaneous growth rates and frequencies determined in this fashion are only reliable where the signal-to-noise ratio is significantly above unity. This problem is tackled here by phase averaging over a number of experiments using as a reference signal the forcing signal. In effect, the phase-averaging procedure rejects the background turbulence and extracts only the organized motions from the total signal (Reynolds & Hussain,

*The same procedure can be followed for investigating forcing frequencies which are near the critical frequency by introducing a small detuning frequency Ω. Then, for $\omega_f = 2\omega_c + \Omega$, the evolution of the global mode in amplitude and frequency is given by

$$\frac{1}{|A_\pm|}\frac{d|A_\pm|}{dt} = \alpha_r + \lambda_r|A_\pm|^2 + \mu_r|E|\cos\Omega t - \mu_i|E|\sin\Omega t \tag{6.23a}$$

$$\omega = \frac{d\phi}{dt} = \alpha_i + \lambda_i|A_\pm|^2 + \mu_i|E|\cos\Omega t + \mu_r|E|\sin\Omega t \tag{6.23b}$$

1972). Averaging here is performed over 50 transient data sets to obtain an average of the amplitude $|A(t)|$ and the instantaneous frequency $\omega(t)$.

After computing the above instantaneous quantities and their derivatives for the exact forcing case, $\omega_f = 2\omega_c$, the identification of the unknown coefficients can be done by data fitting. Specifically, inspection of (6.22a) and (6.22b) reveals that the solutions of the equations lie on a plane, $y = c_0 + c_1 x_1 + c_2 x_2$. The fitted parameters are given in table 6.1.

Parameter	α_r	λ_r	μ_r	α_i	λ_i	μ_i
Value	0.005	-219.861	0.38	1.29	70.141	0.158

Table 6.1.: Values of model parameters obtained from data fitting.

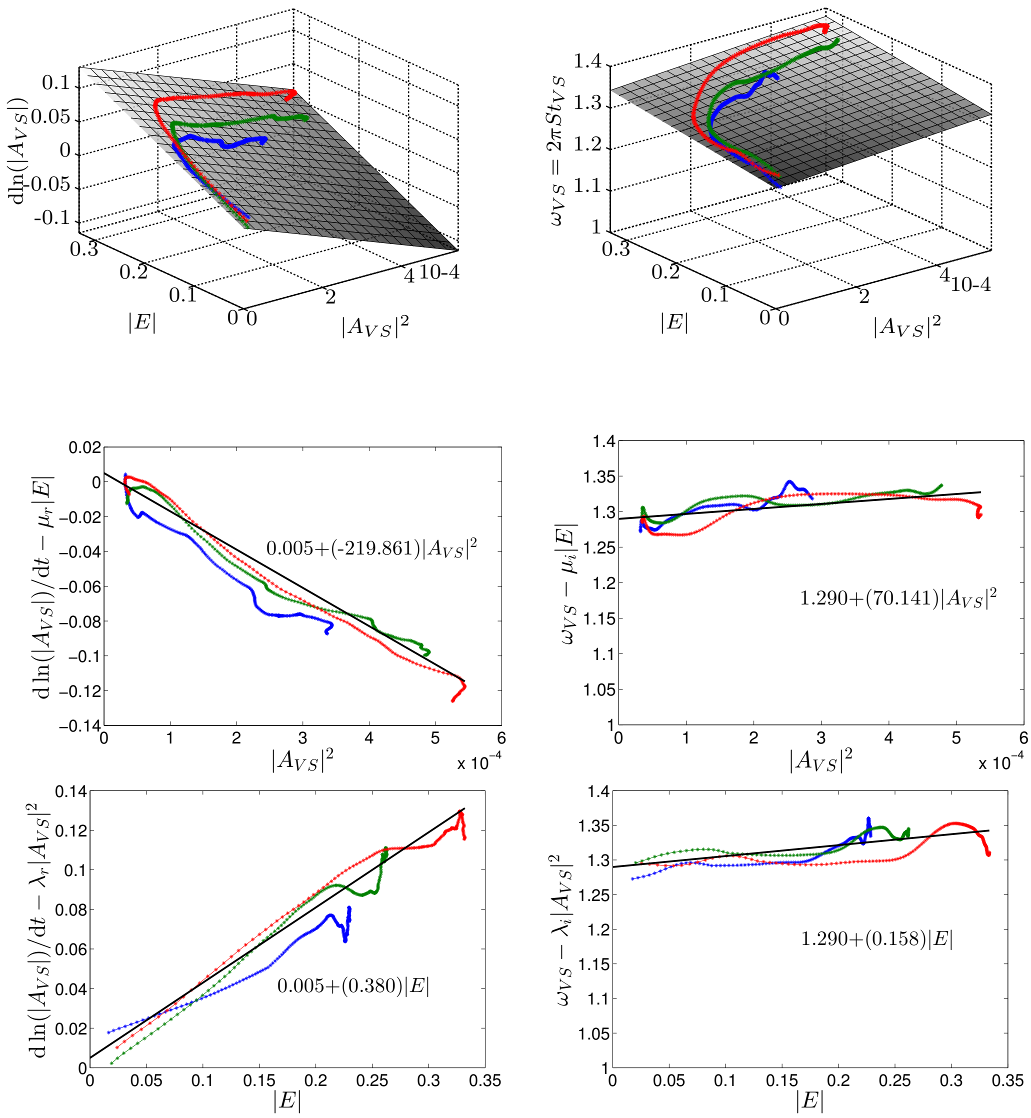

Figure 6.1.: Fitting of model coefficients for $\omega_f = 2\omega_c$. Each fitted plane is presented as $y - c_2x_2 = c_0 + c_1x_1$ and $y - c_1x_1 = c_0 + c_2x_2$. Left: real part. Right: imaginary part.

6.3. Model Predictions

The weakly nonlinear analysis yielded models describing the response of the global shedding mode to axisymmetric forcing. The unknown parameters of the model were determined from experimental measurements. As a last step, the predictions of the model will now be compared to the experimental measurements presented in chapter 5.

6.3.1. Global mode response to forcing

In order to validate the coupled Stuart-Landau equations that resulted from the weakly nonlinear analysis, including the constant coefficient values obtained from experiments, the version of the equation valid for near resonant forcing, equation (6.17), is now used to predict dominant features of the forced response.

We begin by revisiting figure 5.1, in which the response of the global $m = \pm 1$ shedding mode to axisymmetric forcing was presented for a range of frequencies and two forcing amplitudes, exhibiting the well-known “lock-in” phenomenon when forcing was applied near twice the global mode frequency. The model predictions, are shown in figure 6.2. The steady-state amplitude and frequency response obtained from the model are shown as a function of forcing frequency for two forcing amplitudes. It is clear that the model captures accurately the frequency lock-in effect and the parametric subharmonic resonance, as observed in the wind tunnel measurements.

The effect of forcing amplitude on the shedding mode response is now considered for the PSI. Forcing is applied at $St_f = 2St_{VS} + 0.03 = 0.43$, with a small detuning from twice the natural shedding frequency. The model predictions are compared with the experimental results in figure 6.3. The response in $|m| = 1$ is non-linear; when a certain forcing amplitude is reached, frequency “lock-in” occurs and the amplitude rises sharply. This effect is also well-predicted by the model.

6.3.2. Mean Pressure

The effect of axisymmetric forcing on the fluctuating component of the base pressure has been considered in the paper. The effect of forcing on the mean base pressure is also of interest, particularly in pressure-drag reduction applications. It is insightful to consider the response of the mean base pressure here,

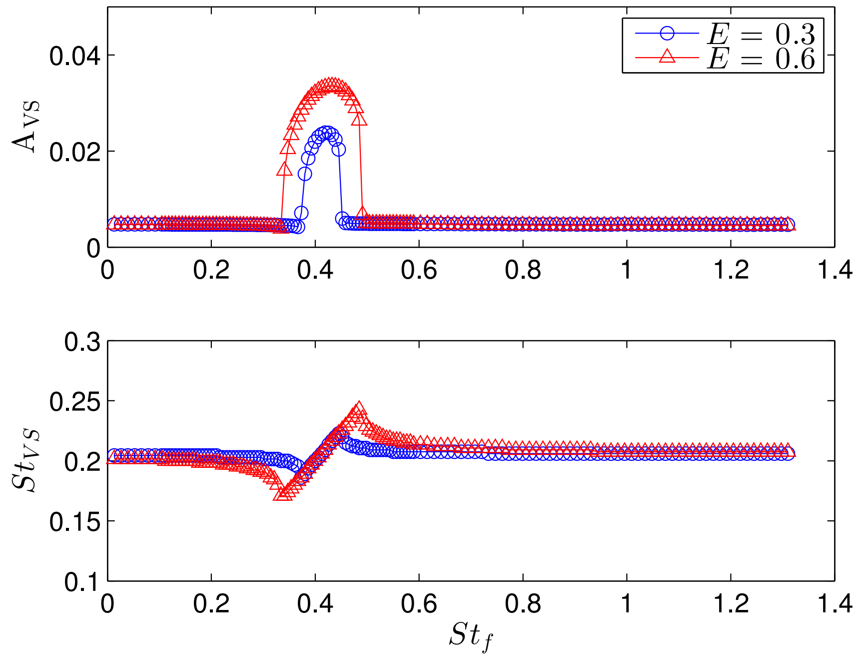

Figure 6.2.: Model simulation: the response of the amplitude and frequency of the $m = \pm 1$ global shedding mode to axisymmetric forcing at different frequencies given by equation (6.17), for two forcing amplitudes.

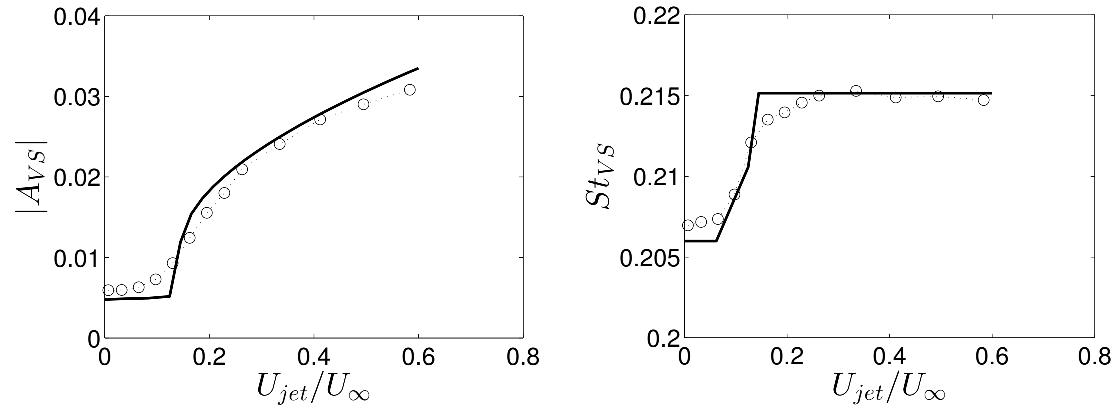

Figure 6.3.: Validation of the model predictions given by equation (6.17) (solid lines) against experimental data (symbols) as a function of the forcing amplitude. Steady-state response of the global vortex shedding mode to ZNMF forcing with azimuthal wavenumber $m = 0$ and frequency close to twice the global mode frequency; amplitude (left) and frequency (right).

and to show that the weakly non-linear model can explain the main features of the changes.

Based on the weakly nonlinear analysis, the mean flow over the entire flow field (r, ϕ, z) is approximated by equation (6.21). This equation is also valid at a fixed downstream location, i.e. on the (r, ϕ) plane that coincides with the base of the body at $z = 0$. If the pressure component p of the flowfield $\mathbf{q}$ is chosen, and integration is performed on the base of the body, this gives the mean base pressure:

$$\overline{p} = \int_0^R \int_0^{2\pi} (\mathbf{p}_0 + \delta \mathbf{p}_2^1 - \frac{\alpha_r}{\lambda_r} \mathbf{q}_2^{|A|^2}) r dr d\phi - |E| \int_0^R \int_0^{2\pi} \frac{\mu_r}{\lambda_r} \mathbf{q}_2^{|A|^2} r dr d\phi \tag{6.24}$$

$$= c_1 - c_2 |E|$$

where c_1 and c_2 are constant and real coefficients determined by the values of the above two double spatial integrals. Hence, for a fixed Reynolds number, a linear change of the mean base pressure is predicted as a function of the forcing amplitude. This linear relation can be seen and validated in figure 5.4, where the experimentally obtained mean base pressure is plotted, as a function of the forcing amplitude (jet velocity). The experimental data show that after a region of low forcing amplitudes that the mean pressure remains constant, an almost linear decrease is observed. The constant slope is well explained for low forcing amplitudes from the response of the vortex shedding mode. In order lock-in to be achieved when axisymmetric forcing is applied close to twice the shedding frequency, a minimum threshold is required depending on the detuning frequency; for both the mean base pressure response and the shedding mode response this threshold appears to coincide.

Thus it is clear that the low-dimensional, weakly non-linear model is accurately capturing the main features of the response of the global shedding mode.

6.4. Concluding remarks

Landau-like models that capture the weakly nonlinear interaction between the global shedding mode and axisymmetric forcing have been derived. The unknown coefficients were determined from transient forced experiments and the model predictions were validated performing experiments on the three dimensional wake of an axisymmetric bluff body, incorporating an axisymmetric ZNMF actuator on the base of the body.

With the present analysis it was demonstrated that the concept of weakly nonlinear global modes can be extended to a fully turbulent flow, far from the critical bifurcation Reynolds number. The Landau-like models derived here capture accurately the forced response by means of measured base pressure of the dominant coherent structures manifesting in a three dimensional turbulent wake.

The models were derived and validated for specific forcing conditions $(\omega_f, m_f) = (2\omega_{VS} + \Omega, 0)$, that is the PSI region. Key factor for the specific choice was the high sensitivity of the global mode close to this forcing frequency due to the PSI, which could be beneficial if the models are used in a feedback control design. The modelling framework presented here can be extended to describe the response of the flow for different forcing frequency ranges (resonant and not) and forcing azimuthal wavenumbers.

7. Conclusions

In this thesis the dynamics of the turbulent three-dimensional wake generated by an axisymmetric bluff body with blunt trailing edge are experimentally and theoretically investigated in an attempt to advance the current understanding and low-dimensional modelling of turbulent flows behind bluff bodies. The main results of this investigation are summarised here together with suggestions for future work.

A finding of great importance in this thesis is that the large scale structures of the turbulent three-dimensional wake retain the structure of the laminar instabilities observed in the transitional regimes, in a statistical sense. Despite the relatively high Reynolds number of the flow under investigation, $Re_D = 188,000$, it is shown that the large scale coherent structures are reminiscent of the two well-documented in the literature steady and unsteady bifurcations observed recently in DNS of axisymmetric bodies at low Reynolds numbers of $\mathcal{O}(100)$. The laminar instabilities are associated with spatial and temporal symmetry breaking, giving rise to spatial reflectional symmetry and periodic vortex shedding. The quasi-periodic vortex shedding is clearly identified at the turbulent regime through spectral analysis and POD decomposition of the base pressure. Interestingly, the reflectional symmetry in the turbulent regime is also clearly revealed by performing averaging on the rotating reference frame of the CoP. A statistical analysis of the CoP showed that the reflection symmetry plane rotates randomly in the azimuthal direction and the turbulent wake is characterised by rotational symmetry in the long time average.

The persistence of the laminar structures at the turbulent regime, allowed us to propose a simple mode for the macroscopic description of the flow. We focused only on the dynamics associated with the spatial symmetry break. The model consists of two coupled stochastic differential equations, the deterministic part of which accounts for the spatial broken symmetries observed in the laminar regime and gives rise to steady large scale structures through a supercritical pitchfork bifurcation, and the stochastic part modelling in a phenomenological sense the turbulent fluctuations acting on the large scale structures. The stochastic model captures important dynamics of the flow. Specifically, predicts the random reorientations of the reflection symmetry plane (VLF mode) and the 'bubble pumping' mode, as random displacements of the CoP in the azimuthal and radial direction due to the presence of noise (turbulence). Similar behavior is observed in a wide range of dynamical systems having rotational symmetry when pertrubed by random noise, usually associated with diffusive processes. The analysis presented here suggests that stochastic dynamics in the presence of symmetry are universal and therefore the method can be applied to other turbulent systems (i.e. Rayleigh-Bénard convection, von Kármán flow), provided that their specific symmetries are taken into account.

It has to be noted that the unsteady bifurcation, responsible for the vortex shedding (limit cycle), has not been considered in the above stochastic analysis. This could be done by adding an extra equation accounting for the temporal broken symmetries due to a Hopf bifurcation. A rich behavior is observed in limit cycling systems under the influence of noise (Newby & Schwemmer, 2014).

As a next step, the effect of flow-forcing using axisymmetric ZNMF slot jet actuation on the predominant modes present in the unforced flow has been examined. It is shown that axisymmetric forcing couples non-linearly with the global shedding mode with this coupling being the main factor that determines the nonlinear flowfield response. The dominant interaction is a parametric resonance mechanism between the forcing and the global shedding mode, when forcing is applied close to twice the shedding frequency (PSI). At these forcing conditions, a pronounced growth of the shedding mode amplitude is observed, simultaneously with a frequency lock in to half the forcing frequency. That reveales a nonlinear mechanism that allows the frequency of the global shedding mode to be controlled through forcing.

Finally, Landau-like models that capture the weakly nonlinear interaction between the global shedding mode and axisymmetric forcing have been derived. The unknown coefficients were determined from transient forced experiments and the model predictions were validated against the experimental measurements. The Landau-like models capture accurately the forced response by means of measured base pressure of the global vortex shedding mode. With the present analysis it is demonstrated that the concept of weakly nonlinear global modes can be extended to a fully turbulent flow, far from the critical bifurcation Reynolds number. These ideas have previously been applied only to laminar wakes.

The Landau models were derived and validated for specific forcing conditions, that is the PSI region. Key factor for the specific choice was the high sensitivity of the global mode close to this forcing frequency due to the PSI, which could be beneficial if the models are used in a feedback control design. Also, a model for the actuator has been derived based on first principles, which in combination with the wake dynamics given by the Landau models, provide the full transfer function between physical input to the actuator and measured output of the system. These low-order models can be used for designing robust closed-loop control strategies (Barbagallo *et al.*, 2009; Sipp & Schmid, 2013) for the suppression of the large scale shedding observed in the turbulent wake of bluff bodies.

Despite the fact that the analysis performed in this thesis was performed solely on pressure data obtained on the base of the axisymmetric body, it is reasonable to expect that due to the global nature of the dynamics of the large scale structures, the same analysis and dynamic modelling should hold for the near-wake velocity field. Thus, it would be interesting to investigate in future experiments the global/local nature of the dynamic characteristics and quantify the observability of the velocity field in the near wake from pressure measurements. This could be achieved by simultaneous measurements of the velocity field using time-resolved particle image velocimetry techniques and of the pressure field.

Finally, it is well-known that the symmetries of the experimental set-up play an important role in the theoretical bifurcation scenario in the transitional regimes of wakes produced by three-dimensional bodies. For axisymmetric body wakes, the rotational symmetry, $O(2)$, observed at low Reynolds numbers is broken through a steady bifurcation and the resulting flow has reduced symmetry. The weakly nonlinear concepts should be applicable in other three-dimensinal wakes. For instance, these ideas could be applicable in bodies with $D(2)$ symmetry, i.e. the Ahmed body, as suggested by experimental data at low Reynolds numbers (Grandemange *et al.*, 2012*a*), provided the specific symmetry is taken into account as well as the presence of the ground effect. A weakly nonlinear analysis close to the threshold of bifurcations could potentially explain and model the transitional dynamics. Also, strong evidence exists that supports the extension of the models presented here in turbulent regime. The bistability observed in the Ahmed body turbulent wake results from the random exploration of two symmetry broken laminar-like states in the lateral direction (Grandemange *et al.*, 2013). The two-dimensional stochastic model presented in chapter 3, describing the restoration of broken symmetries in the axisymmetric wake, if used only in one dimensional, is a typical bistable system that explains and models the above behaviour.

Bibliography

Achenbach, E. 1974 Vortex shedding from spheres. *J. Fluid Mech.* **62**, 209–221.

Ahmed, S. R., Ramm, G. & Faitin, G. 1984 Some salient features of the time-averaged ground vehicle wake. *SAE Tech. Rep.* (840300).

Barbagallo, A., Sipp, D. & Schmid, P. 2009 Closed-loop control of an open cavity flow using reduced-order models. *J. Fluid Mech.* **641**, 1–50.

Barkley, D. 2006 Linear analysis of the cylinder wake mean flow. *Europhys. Lett.* **75** (5), 750.

Berger, E., Scholz, D. & Schumm, M. 1990 Coherent vortex structures in the wake of a sphere and a circular disk at rest and under forced vibrations. *J. Fluids Struct.* **4**, 231–257.

Bigger, R. P., Higuchi, H. & Hall, J. W. 2009 Open-loop control of disk wakes. *AIAA J.* **47** (5), 1186–1194.

Bobinski, T., Goujon-Durand, S. & Wesfreid, J. E. 2014 Instabilities in the wake of a circular disk. *Phys. Rev. E* **89**, 053021.

Bohorquez, P., Sanmiguel-Rojas, E., Sevilla, A., Jiménez-González, J. I. & Martínez-Bazán, C. 2011 Stability and dynamics of the laminar wake past a slender blunt-based axisymmetric body. *J. Fluid Mech.* **676**, 110–144.

Brown, E. & Ahlers, G. 2006 Rotations and cessations of the large-scale circulation in turbulent Rayleigh-Bénard convection. *J. Fluid Mech.* **568**, 351–386.

Brown, E. & Ahlers, G. 2007 Large-scale circulation model for turbulent Rayleigh-Bénard convection. *Phys. Rev. Lett.* **98** (13), 134501.

Brown, E., Nikolaenko, A. & Ahlers, G. 2005 Reorientation of the large-scale circulation in turbulent Rayleigh-Bénard convection. *Phys. Rev. Lett.* **95** (8), 084503.

Brown, G. L. & Roshko, A. 1974 On density effects and large structure in turbulent mixing layers. *J. Fluid Mech.* **64** (04), 775–816.

Bury, Y. & Jardin, T. 2012 Transitions to chaos in the wake of an axisymmetric bluff body. *Phys. Lett. A* **376**, 3219–3222.

Chaudhari, M., Verma, G., Puranik, B. & Agrawal, A. 2009 Frequency response of a synthetic jet cavity. *Exp. Thermal Fluid Sci.* **33**, 439–438.

Choi, H., Jeon, W.-P. & K., J. 2008 Control of flow over a bluff body. *Ann. Rev. Fluid Mech.* **40**, 113–139.

Chomaz, J.-M. 2005 Global instabilities in spatially developing flows: non-normality and nonlinearity. *Annu. Rev. Fluid Mech.* **37**, 357–392.

Craik, A. D. D. 1988 *Wave interactions and fluid flows*. Cambridge University Press.

Drazin, P. G. & Reid, W. H. 2004 *Hydrodynamic stability*. Cambridge University Press.

Dušek, J., Le Gal, P. & Fraunié, P. 1994 A numerical and theoretical study of the first hopf bifurcation in a cylinder wake. *J. Fluid Mech.* **264**, 59–80.

Einstein, A. 1905 Über die von der molekularkinetischen theorie der wärme geforderte bewegung von in ruhenden flüssigkeiten suspendierten teilchen. *Ann. Phys.* **322** (8), 549–560.

Fabre, D., Auguste, F. & Magnaudet, J. 2008 Bifurcations and symmetry breaking in the wake of axisymmetric bodies. *Phys. Fluids* **20** (5), 051702.

Frisch, U. 1996 Turbulence. *Cambridge University Press, Cambridge, UK* .

Fuchs, H. V., Mercker, E. & Michel, U. 1979 Large-scale coherent structures in the wake of axisymmetric bodies. *J. Fluid Mech.* **93**, 185–207.

Gardiner, C. 1985 *Stochastic methods*. Springer-Verlag.

Ghidersa, B. & Dušek, J. 2000 Breaking of axisymmetry and onset of unsteadiness in the wake of a sphere. *J. Fluid Mech.* **423**, 33–69.

Grandemange, M. 2013 *Analysis and control of three-dimensional turbulent wakes: from axisymmetric bodies to real road vehicles*. PhD Thesis, ENSTA ParisTech.

Grandemange, M., Cadot, O. & Gohlke, M. 2012*a* Reflectional symmetry breaking of the separated flow over three-dimensional bluff bodies. *Phys. Rev. E* **86** (3), 035302.

Grandemange, M., Gohlke, M. & Cadot, O. 2013 Turbulent wake past a three-dimensional blunt body. Part 1. Global modes and bi-stability. *J. Fluid Mech.* **722**, 51–84.

Grandemange, M., Gohlke, M., Parezanović, V. & Cadot, O. 2012*b* On experimental sensitivity analysis of the turbulent wake from an axisymmetric blunt trailing edge. *Phys. Fluids* **24**, 035106.

Gad-el Hak, M. 2000 *Flow control: passive, active, and reactive flow management*. Cambridge University Press.

Ho, C.-M. & Huerre, P. 1984 Perturbed free shear layers. *Ann. Rev. Fluid Mech.* **16** (1), 365–422.

Holmes, P., Lumley, J. L., Berkooz, G. & Rowley, C. W. 2012 *Turbulence, Coherent Structures, Dynamical systems and Symmetry; 2nd ed.*. Cambridge University Press.

Hucho, W.-H. (ed.) 1998 *Aerodynamics of road vehicles*, 4th edn. Society of Automotive Engineers, SAE.

Huerre, P. & Monkewitz, P. A. 1990 Local and global instabilities in spatially developing flows. *Ann. Rev. Fluid Mech.* **22** (1), 473–537.

Kim, H. J. & Durbin, P. A. 1988 Observations of the frequencies in a sphere wake and of drag increase by acoustic excitation. *Phys. Fluids* **31** (11), 3260–3265.

de La Torre, A. & Burguete, J. 2007 Slow dynamics in a turbulent von Kármán swirling flow. *Phys. Rev. Lett.* **99** (5), 054101.

Landau, L. D. 1944 On the problem of turbulence. *C.R. Acad. Sci. URSS* **44** (31), 1–314.

Landau, L. D. & Lifshitz, E. M. 1959 *Fluid Mechanics: Course of Theoretical Physics*, , vol. 6. Pergamon.

Lin, N., Reed, H. L. & Saric, W. S. 1992 Effect of leading-edge geometry on boundary-layer receptivity to freestream sound. In *Instability, Transition, and Turbulence*, pp. 421–440. Springer.

Ljung, L. 1998 *System identification*. Springer.

Lumley, J. L. 1970 *Stochastic tools in turbulence*. Academic Press, New York.

Mair, W. A. 1965 The effect of a rear mounted disc on the drag of a blunt-based body of revolution. *Aeronaut. Quarterly* **16**, 350–360.

Meliga, P., Chomaz, J.-M. & Sipp, D. 2009 Global mode interaction and pattern selection in the wake of a disk: a weakly nonlinear expansion. *J. Fluid Mech.* **633**, 159–189.

Meliga, P., Pujals, G. & Serre, É. 2012 Sensitivity of 2-D turbulent flow past a D-shaped cylinder using global stability. *Phys. Fluids* **24** (6), 061701.

Monkewitz, P. A. 1988 A note on vortex shedding from axisymmetric bluff bodies. *J. Fluid Mech.* **192**, 561–575.

Natarajan, R. & Acrivos, A. 1993 The instability of the steady flow past spheres and disks. *J. Fluid Mech.* **254**, 323–344.

Newby, J. M. & Schwemmer, M. A. 2014 Effects of moderate noise on a limit cycle oscillator: Counterrotation and bistability. *Phys. Rev. Lett.* **112**, 114101.

Noack, B. R., Afanasiev, K., Morzynski, M., Tadmor, G. & Thiele, F. 2003 A hierarchy of low-dimensional models for the transient and post-transient cylinder wake. *J. Fluid Mech.* **497**, 335–363.

Ormières, D. & Provansal, M. 1999 Transition to turbulence in the wake of a sphere. *Phys. Rev. Lett.* **83** (1), 80.

Oxlade, A. R. 2013 *High-frequency periodic jet forcing of a turbulent axisymmetric wake*. PhD Thesis, Imperial College.

Oxlade, A. R., Morrison, J. F., Qubain, A. & Rigas, G. 2015 High-frequency forcing of a turbulent axisymmetric wake. *In press, Journal of Fluid Mechanics* .

Pastoor, M., Henning, L., Noack, B. R., King, R. & Tadmor, G. 2008 Feedback shear layer control for bluff body drag reduction. *J. Fluid Mech.* **608**, 161–196.

Persoons, T. 2012 General reduced-order model to design and operate synthetic jet actuators. *AIAA J.* **50** (4), 916–927.

Persoons, T. & O'Donovan, T. S. 2007 A pressure-based estimate of synthetic jet velocity. *Phys. Fluids* **19** (12), 128104.

Pier, B. 2008 Local and global instabilities in the wake of a sphere. *J. Fluid Mech.* **603**, 39–62.

Pope, S. B. 2000 *Turbulent flows*. Cambridge University Press.

Procaccia, I. 1988 Universal properties of dynamically complex systems-the organization of chaos. *Nature* **333**, 618–623.

Provansal, M., Mathis, C. & Boyer, L. 1987 Bénard-von kármán instability: transient and forced regimes. *J. Fluid Mech.* **182**, 1–22.

Qubain, A. 2009 *Active control of a turbulent bluff body wake*. PhD Thesis, Imperial College.

Reynolds, W. C. & Hussain, A. K. M. F. 1972 The mechanics of an organized wave in turbulent shear flow. part 3. theoretical models and comparisons with experiments. *J. Fluid Mech.* **54**, 263–288.

Risken, H. 1984 *Fokker-Planck Equation*. Springer.

Ruelle, D. & Takens, F. 1971 On the nature of turbulence. *Comm. Mathematical Phys.* **20** (3), 167–192.

Sanmiguel-Rojas, E., Jiménez-González, J. I., Bohorquez, P., Pawlak, G. & Martínez-Bazán, C. 2011 Effect of base cavities on the stability of the wake behind slender blunt-based axisymmetric bodies. *Phys. Fluids* **23**, 114103.

Sanmiguel-Rojas, E., Sevilla, A., Martínez-Bazán, C. & Chomaz, J.-M. 2009 Global mode analysis of axisymmetric bluff-body wakes: Stabilization by base bleed. *Phys. Fluids* **21**, 114102.

Schumm, M., Berger, E. & Monkewitz, P. A. 1994 Self-excited oscillations in the wake of two-dimensional bluff bodies and their control. *J. Fluid Mech.* **271**, 17–53.

Sevilla, A. & Martínez-Bazán, C. 2004 Vortex shedding in high Reynolds number axisymmetric bluff-body wakes: Local linear instability and global bleed control. *Phys. Fluids* **16**, 3460–3469.

Sipp, D. 2012 Open-loop control of cavity oscillations with harmonic forcings. *J. Fluid Mech.* **1** (1), 1–30.

Sipp, D. & Lebedev, A. 2007 Global stability of base and mean flows: a general approach and its applications to cylinder and open cavity flows. *J. Fluid Mech.* **593**, 333–358.

Sipp, D. & Schmid, P. 2013 Closed-loop control of fluid flow: a review of linear approaches and tools for the stabilization of transitional flows.

Sreenivasan, K. R., Bershadskii, A. & Niemela, J. J. 2002 Mean wind and its reversal in thermal convection. *Phys. Rev. E* **65**, 056306.

Taneda, S. 1978 Visual observations of the flow past a sphere at Reynolds numbers between 10^4 and 10^6. *J. Fluid Mech.* **85**, 187–192.

Tomboulides, A. G. & Orszag, S. A. 2000 Numerical investigation of transitional and weak turbulent flow past a sphere. *J. Fluid Mech.* **416**, 45–73.

Van Dyke, M. 1982 An album of fluid motion .

Vilaplana, G., Grandemange, M., Gohlke, M. & Cadot, O. 2013 Global mode of a sphere turbulent wake controlled by a small sphere. *J. Fluids Struct.* **41**, 119–126.

Weickgenannt, A. & Monkewitz, P. A. 2000 Control of vortex shedding in an axisymmetric bluff body wake. *Eur. J. Mech. B-Fluids* **19**, 789–812.

A. Stochastic Differential Equations

A.1. Langevin equation

The simple Langevin equation that turns up most often can be written in the form

$$\frac{dx}{dt} = a(x,t) + b(x,t)\xi(t), \tag{A.1}$$

where x is the variable of interest, $a(x,t)$ and $b(x,t)$ are certain known functions and $\xi(t)$ is the randomly fluctuating random term with

$$\langle \xi(t)\xi'(t) \rangle = \delta(t - t'), \tag{A.2}$$

Above, $\delta(t)$ is the Dirac delta function, t and t' are distinct times. If the $b(x,t)$ is constant, i.e. $b(x,t) = \sigma$, the system is said to be subject to additive noise, otherwise it is said to be subject to multiplicative noise.
An alternative formulation of A.3 is

$$dx = a(x,t)dt + b(x,t)dW, \tag{A.3}$$

where W denotes a Wiener process (standard Brownian motion).

A.2. Fokker-Planck equation

The probability density $P(x,t)$ for the random variable x satisfies the FokkerPlanck equation

$$\frac{\partial P}{\partial t} = \frac{1}{2}\frac{\partial^2}{\partial x^2}[b^2(x)P] - \frac{\partial}{\partial x}[a(x)P], \tag{A.4}$$

or

$$\frac{\partial P}{\partial t} = \frac{1}{2}\nabla^2[b^2(x)P] - \nabla \cdot [a(x)P]. \tag{A.5}$$

A.3. Change of variables

Consider an arbitrary function $x : f(x)$. We use Ito's formula for change of variables and expand $df(x)$ to second order in dW:

$$\begin{aligned} df(x) &= f(x+dx) - f(x) \\ &= f'(x)dx + 0.5f''(x)dx^2 + \dots \\ &= f'(x)\left\{[a(x,t)]dt + b[x,t]dW\right\} + 0.5f''(x)b(x,t)^2[dW]^2 + \dots \\ &= \left\{[a(x,t)]f'(x) + 0.5f''(x)b(x,t)^2\right\}dt + b[x,t]f'(x)dW \end{aligned} \tag{A.6}$$

A.4. Pitchfork bifurcation in the presence of noise

In Cartesian coordinates, the system undergoing a pitchfork bifurcation in the presence of additive noise reads:

$$\dot{\mathbf{x}} = \alpha\mathbf{x} + \lambda\mathbf{x}|\mathbf{x}|^2 + \sigma\xi, \tag{A.7}$$

where $\mathbf{x} = (x, y)$ and $\xi = (\xi_x, \xi_y)$.

A.4.1. Fokker-Planck

The Fokker–Plank for the joint PDF $P(x, y, t)$ in Cartesian rectangular variables is:

$$\frac{\partial P}{\partial t} = D\left(\frac{\partial^2 P}{\partial x^2} + \frac{\partial^2 P}{\partial y^2}\right) - \frac{\partial}{\partial x}\{[\alpha x + \lambda x(x^2+y^2)]P\} - \frac{\partial}{\partial y}\{[\alpha y + \lambda y(x^2+y^2)]P\}. \tag{A.8}$$

We look for a stationary solution $P_s(x, y)$ for $t \to \infty$:

$$D\left(\frac{\partial^2 P}{\partial x^2} + \frac{\partial^2 P}{\partial y^2}\right) = \frac{\partial}{\partial x}\{[\alpha x + \lambda x(x^2+y^2)]P\} + \frac{\partial}{\partial y}\{[\alpha y + \lambda y(x^2+y^2)]P\}. \tag{A.9}$$

Integrating:

$$\frac{\partial P_s}{\partial x} + \frac{\partial P_s}{\partial y} = [\alpha(x+y) + \lambda(x+y)(x^2+y^2)]P_s/D + C_1 \tag{A.10}$$

and $C_1 = 0$ because of the boundary conditions as $(x, y) \to \pm\infty$. So the stationary joint probability density function is given by

$$P_s(x,y) = C \exp\left\{\frac{1}{D}\left[\frac{\alpha}{2}(x^2+y^2) + \frac{\lambda}{4}(x^2+y^2)^2\right]\right\} \tag{A.11}$$

and the potential $U(x, y)$

$$U(x,y) = -\left[\frac{\alpha}{2}(x^2+y^2) + \frac{\lambda}{4}(x^2+y^2)^2\right] \tag{A.12}$$

such that

$$P_s(x,y) = C \exp\left[-\frac{1}{D}U(x,y)\right]. \tag{A.13}$$

The constant C is found by the normalization requirement $\int_{-\infty}^{+\infty}\int_{-\infty}^{+\infty} P_s(x,y)dxdy = 1$. Also, the one dimensional components of the 2D PDF can be calculated by integration.

A.4.2. Coordinate transformation: Cartesian to polar

The system (A.7) is transformed from $(x, y) \to (r, \phi)$. We have $x = r\cos\phi$ and $y = r\sin\phi$. Also, we define $\mu(t) = \log r$, so that

$$\mu + i\phi = \log(x+iy). \tag{A.14}$$

We expand $d(\mu + i\phi)$ to second order in dW

$$\begin{aligned} d(\mu+i\phi) &= [\log(x+iy)]'d(x+iy) + 0.5[\log(x+iy)]''[d(x+iy)]^2 \\ &= \frac{d(x+iy)}{x+iy} - 0.5\frac{d(x+iy)^2}{(x+iy)^2} \\ &= \frac{a(x+iy) + \lambda(x+iy)(x^2+y^2)}{x+iy}dt + \frac{\sigma(dW_x(t) + idW_y(t))}{x+iy} \\ &\quad - 0.5\frac{\sigma^2(dW_x(t)+idW_y(t))^2}{(x+iy)^2} \end{aligned} \tag{A.15}$$

and noting $dW_x dW_y = 0$ and $dW_x^2 = dW_y^2 = dt$, the last term vanishes, so we find

$$d(\mu + i\phi) = (a + \lambda r^2)dt + \sigma \exp(-\mu - i\phi)(dW_x(t) + idW_y(t)). \tag{A.16}$$

Setting $r = \exp \mu$, and separating real and imaginary parts we have

$$dr = (ar + \lambda r^3 + 0.5\sigma^2/r)dt + \sigma(dW_x \cos\phi + dW_y \sin\phi), \tag{A.17}$$

$$d\phi = \sigma/r(dW_x \sin\phi + dW_y \cos\phi). \tag{A.18}$$

We now define

$$dW_r = (dW_x \cos\phi + dW_y \sin\phi), \tag{A.19a}$$

$$dW_\theta = (dW_x \sin\phi + dW_y \cos\phi). \tag{A.19b}$$

The above is an orthogonal transformation so that we may take dW_r and dW_θ as increments of independent Wiener processes. Hence, we have

$$dr = ar + \lambda r^3 + 0.5\sigma^2 \frac{1}{r} + \sigma dW_r, \tag{A.20a}$$

$$d\phi = \frac{\sigma}{r} dW_\theta. \tag{A.20b}$$

Probability Density Function The Fokker–Plank for the joint PDF $P(r, \phi, t)$ in polar variables is:

$$\frac{\partial P}{\partial t} = D\left(\frac{1}{r}\frac{\partial}{\partial r}\left(r\frac{\partial P}{\partial r}\right) + \frac{1}{r^2}\frac{\partial^2 P}{\partial \phi^2}\right) - \frac{1}{r}\frac{\partial}{\partial r}[(ar + \lambda r^3 + \frac{D}{r})rP]. \tag{A.21}$$

Note: for polar coordinates:

$$\nabla \cdot \mathbf{F} = \frac{1}{r}\frac{\partial}{\partial r}(rF_r) + \frac{1}{r}\frac{\partial F_\phi}{\partial \phi}$$

$$\nabla^2 f = \frac{1}{r}\frac{\partial}{\partial r}\left(r\frac{\partial f}{\partial r}\right) + \frac{1}{r^2}\frac{\partial^2 f}{\partial \phi^2}, = \frac{1}{r}\frac{\partial f}{\partial r} + \frac{\partial^2 f}{\partial r^2} + \frac{1}{r^2}\frac{\partial^2 f}{\partial \phi^2}.$$

We look for a stationary solution $P_s(r, \phi)$ for $t \to \infty$:

$$D\left(\frac{1}{r}\frac{\partial}{\partial r}\left(r\frac{\partial P_s}{\partial r}\right) + \frac{1}{r^2}\frac{\partial^2 P_s}{\partial \phi^2}\right) = \frac{1}{r}\frac{\partial}{\partial r}[(ar + \lambda r^3 + \frac{D}{r})rP_s] \tag{A.22}$$

and for ϕ-independent solution, since the drifts and diffusivities are ϕ-independent, so we set

$$\frac{\partial P_s}{\partial \phi} = 0. \tag{A.23}$$

This reduces the equation to one-variable problem (ODE):

$$D\frac{1}{r}\frac{\partial}{\partial r}\left(r\frac{\partial P_s}{\partial r}\right) = \frac{1}{r}\frac{\partial}{\partial r}[(ar + \lambda r^3 + \frac{D}{r})rP_s]. \tag{A.24}$$

Integrating:

$$\frac{\partial P_s}{\partial r} = [ar + \lambda r^3 + \frac{D}{r}]P_s/D + C_1 \tag{A.25}$$

and $C_1 = 0$. So the stationary joint probability density function is given by

$$P_s(r) = C\exp\left\{\frac{1}{D}\left[\frac{\alpha r^2}{2} + \frac{\lambda r^4}{4} + D\ln r\right]\right\} \tag{A.26}$$

and the potential $U(r)$

$$U(r) = -\left[\frac{\alpha r^2}{2} + \frac{\lambda r^4}{4} + D\ln r\right]. \tag{A.27}$$

B. Unforced base pressure modes from Endevco

The spectra of the base-pressure fluctuations obtained from the 8 pressure transducers, decomposed into azimuthal modes, are shown in figure B.1. The radially averaged spectra of the same quantity obtained from the 64 pressure taps on the base of the body are potted in figure 3.2.

Qualitatively the same information is obtained here from both measurements regarding the large scale structures. Among the peaks in the premultiply spectra, we identify the global vortex shedding mode ($|m| = 1$, $St_{VS} = 0.2$) and the subharmonic of the shedding mode ($|m| = 1, 2$, $St_{VS} = 0.2$). Also two broader regions of energy are distinguishable and are associated with the VLF mode ($|m| = 1$, $St_{VLF} = 0.002$) and the bubble pumping mode ($m = 0$, $St = 0.06$). Based on the spectral information obtained from the Endevco transducers, we conclude the modal information is observable and can be obtained from the 8 transducers EDV. The modes obtained from the radially averaged base pressure fluctuations are equally observable from measurements performed in one radial position. The radial position of the Endevco transducers is near to the location of maximum rms pressure, $r = 0.3D$.

The use of only 8 transducers strategically located at the location of maximum rms pressure offers the advantage of keeping low the instrumention cost as well as the computational cost. The latter is of paramount importance in feedback control schemes where processing of data has to be performed on real-time.

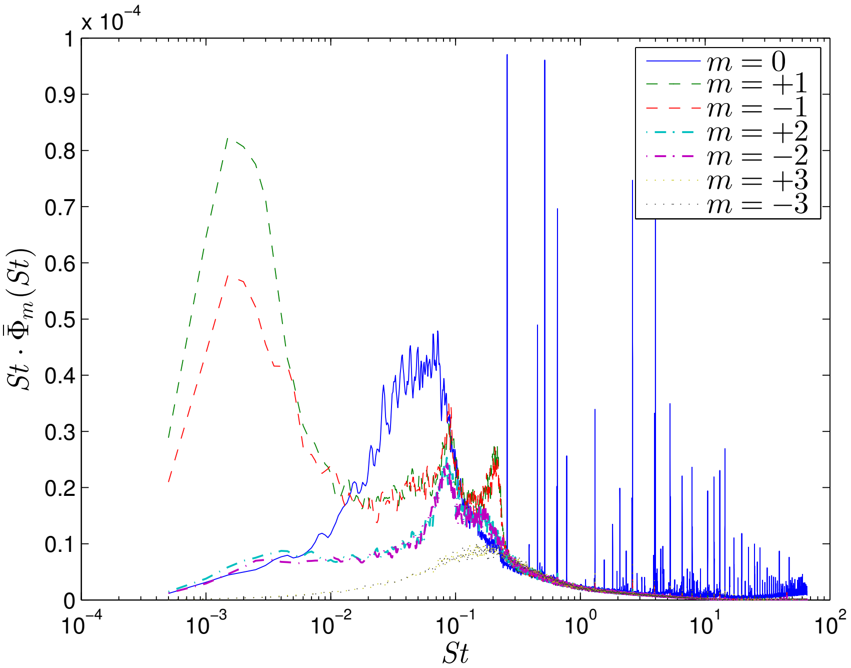

Figure B.1.: Premultiplied spectra of the base pressure fluctuations obtained from the 8 pressure transducers, decomposed in azimuthal modes.

C. Weakly nonlinear analysis

Here, the equations governing the forced amplitude evolution of the unstable global modes of the turbulent flow for the turbulent axisymmetric wake are derived. The analysis is based on the weakly nonlinear analysis proposed by Sipp (2012), in which the forcing enters the amplitude equations.
The analysis distinguishes between two cases depending on the forcing frequency; non-resonant case (ω_f is not close to $2\omega_0$) and resonant case (ω_f is close to $2\omega_0$).

C.1. Non-resonant case

C.1.1. Order $\sqrt{\varepsilon}^1$

$$\partial_t \mathbf{u_1} + \mathbf{u_0} \cdot \nabla \mathbf{u_1} + \mathbf{u_1} \cdot \nabla \mathbf{u_0} + \nabla p_1 - \mathrm{Re}_\mathrm{c}^{-1} \nabla^2 \mathbf{u_1} = 0 \quad \text{and} \quad \nabla \cdot \mathbf{u_1} = 0 \tag{C.1}$$

The above set of equations can also be written in a more elegant way as

$$\left(\partial_t \mathcal{P}\mathcal{P}^T + \mathcal{M}\right) \mathbf{q}_1 = 0 \tag{C.2}$$

with $\mathcal{M}$ being the linearized Navier-Stokes operator, $\mathcal{P}$ a prolongation operator which transforms $\mathbf{u}$ into $(\mathbf{u}, 0)^T$ and $\mathcal{P}^T$ a restriction operator which transforms $(\mathbf{u}, p)^T$ quantity into $\mathbf{u}$:

$$\mathcal{M} = \begin{pmatrix} \mathbf{u_0} \cdot \nabla() + () \cdot \nabla \mathbf{u_0} - \mathrm{Re}_\mathrm{c}^{-1} \nabla^2 & \nabla \\ \nabla^T & 0 \end{pmatrix}, \quad \mathcal{P} = \begin{pmatrix} \mathcal{I} \\ 0 \end{pmatrix} \tag{C.3}$$

The solution is sought in the form

$$\begin{aligned} \mathbf{q}_1 &= A_+ e^{i\phi} e^{i\omega t} \mathbf{q}_1^A + A_- e^{-i\phi} e^{i\omega t} \mathbf{q}_1^A + E e^{i\omega_f t} \mathbf{q}_1^E + c.c. \\ &= A_\pm (e^{i\phi} + e^{-i\phi}) e^{i\omega t} \mathbf{q}_1^A + E e^{i\omega_f t} \mathbf{q}_1^E + c.c. \end{aligned} \tag{C.4}$$

and consists of the superposition of the global mode and the forcing response.

The eigenfunctions $\mathbf{q}_1^A$ and $\mathbf{q}_1^E$ can be found from:

$$\left(i\omega_c \mathcal{P}\mathcal{P}^T + \mathcal{M}\right) \mathbf{q}_1^A = 0 \tag{C.5}$$

$$\left(i\omega_f \mathcal{P}\mathcal{P}^T + \mathcal{M}\right) \mathbf{q}_1^E = 0 \tag{C.6}$$

with $\mathbf{u} = \mathbf{u}_C$ on some given forcing boundary Γ_C for (C.6). Equation (C.6) defines $\mathbf{q}_E$ as the linear response of the flow to the forcing $\mathbf{f}_E$. Notice that, in order to invert (C.6), the value $i\omega_f$ cannot belong to the eigenvalue spectrum at $\mathrm{Re_c}$.

C.1.2. Order $\sqrt{\varepsilon}^2$

$$\partial_t \mathbf{u}_2 + \mathbf{u}_0 \cdot \nabla \mathbf{u}_2 + \mathbf{u}_2 \cdot \nabla \mathbf{u}_0 + \nabla p_2 - \mathrm{Re_c^{-1}} \nabla^2 \mathbf{u}_2 = -\nabla^2 \mathbf{u}_0 - \mathbf{u}_1 \cdot \nabla \mathbf{u}_1 \tag{C.7}$$

Considering equation (C.4), the above system becomes:

$$\begin{aligned}\left(\partial_t \mathcal{P}\mathcal{P}^T + \mathcal{M}\right) \mathbf{q}_2 = & \mathbf{F}_2^1 + |A_\pm|^2 \mathbf{F}_2^{|A_\pm|^2} + [A_\pm^2 (e^{2i\phi} + e^{2i\phi}) e^{2i\omega_c t} \mathbf{F}_2^{A_\pm^2} + c.c.] \\ & + [A_\pm E (e^{i\phi} + e^{i\phi}) e^{i(\omega+\omega_f)t} \mathbf{F}_2^{A_\pm E} + A_\pm E^* (e^{i\phi} + e^{i\phi}) e^{i(\omega-\omega_f)t} \mathbf{F}_2^{A_\pm E^*}] \\ & + (E^2 e^{2i\omega_f t} \mathbf{F}_2^{E^2} + c.c.) + |E|^2 \mathbf{F}_2^{|E|^2}\end{aligned} \tag{C.8}$$

where

$$\mathbf{F}_2^1 = \mathcal{P}\left(-\nabla^2 \mathbf{u}_0\right) \tag{C.9}$$
$$\mathbf{F}_2^{|A|^2} = \mathcal{P}\left(-\mathbf{u}^{*A}_1 \cdot \nabla \mathbf{u}_1^A - \mathbf{u}_1^A \cdot \nabla \mathbf{u}^{*A}_1\right) \tag{C.10}$$
$$\mathbf{F}_2^{A^2} = \mathcal{P}\left(-\mathbf{u}_1^A \cdot \nabla \mathbf{u}_1^A\right) \tag{C.11}$$
$$\mathbf{F}_2^{|E|^2} = \mathcal{P}\left(-\mathbf{u}^{*E}_2 \cdot \nabla \mathbf{u}_2^E - \mathbf{u}_2^E \cdot \nabla \mathbf{u}^{*E}_2\right) \tag{C.12}$$
$$\mathbf{F}_2^{AE} = \mathcal{P}\left(-\mathbf{u}_2^E \cdot \nabla \mathbf{u}_2^A - \mathbf{u}_2^A \cdot \nabla \mathbf{u}_2^E\right) \tag{C.13}$$
$$\mathbf{F}_2^{AE^*} = \mathcal{P}\left(-\mathbf{u}^{*E}_2 \cdot \nabla \mathbf{u}_2^A - \mathbf{u}_2^A \cdot \nabla \mathbf{u}^{*E}_2\right) \tag{C.14}$$
$$\mathbf{F}_2^{E^2} = \mathcal{P}\left(-\mathbf{u}_2^E \cdot \nabla \mathbf{u}_2^E\right) \tag{C.15}$$

The terms on the right-hand side of (C.8) are forcing terms. The velocity fields involved in these expressions have been determined at lower order. Since (C.8) is linear, we may write the solution as the superposition of $\mathbf{q}_2^1$, $\mathbf{q}_2^{|A|^2}$ and $\mathbf{q}_2^{A^2}$ corresponding to the response of the linear system to $\mathbf{F}_2^1$, $\mathbf{F}_2^{|A|^2}$ and $\mathbf{F}_2^{A^2}$, respectively, *i.e.*

$$\begin{aligned}\mathbf{q}_2 =&\mathbf{q}_2^1 + |A_\pm|^2\mathbf{q}_2^{|A|^2} + [A_\pm^2(e^{2i\phi} + e^{2i\phi})e^{2i\omega_c t}\mathbf{q}_2^{A^2} + c.c.]\\ &+ [A_\pm E(e^{i\phi} + e^{i\phi})e^{i(\omega+\omega_f)t}\mathbf{q}_2^{AE} + A_\pm E^*(e^{i\phi} + e^{i\phi})e^{i(\omega-\omega_f)t}\mathbf{q}_2^{AE^*}]\\ &+ (E^2 e^{2i\omega_f t}\mathbf{q}_2^{E^2} + c.c.) + |E|^2\mathbf{q}_2^{|E|^2}\end{aligned} \tag{C.16}$$

where

$$\mathcal{M}\mathbf{q}_2^1 = \mathcal{P}\left(-\nabla^2\mathbf{u}_0\right) \tag{C.17}$$
$$\mathcal{M}\mathbf{q}_2^{|A|^2} = \mathcal{P}\left(-\mathbf{u}^{*A}_1 \cdot \nabla\mathbf{u}_1^A - \mathbf{u}_1^A \cdot \nabla\mathbf{u}^{*A}_1\right) \tag{C.18}$$
$$(2i\omega_c\mathcal{P}\mathcal{P}^T + \mathcal{M})\mathbf{q}_2^{A^2} = \mathcal{P}\left(-\mathbf{u}_1^A \cdot \nabla\mathbf{u}_1^A\right) \tag{C.19}$$
$$\mathcal{M}\mathbf{q}_2^{|E|^2} = \mathcal{P}\left(-\mathbf{u}^{*E}_2 \cdot \nabla\mathbf{u}_2^E - \mathbf{u}_2^E \cdot \nabla\mathbf{u}^{*E}_2\right) \tag{C.20}$$
$$(i(\omega_c + \omega_f)\mathcal{P}\mathcal{P}^T + \mathcal{M})\mathbf{q}_2^{AE} = \mathcal{P}\left(-\mathbf{u}_2^E \cdot \nabla\mathbf{u}_2^A - \mathbf{u}_2^A \cdot \nabla\mathbf{u}_2^E\right) \tag{C.21}$$
$$(i(\omega_c - \omega_f)\mathcal{P}\mathcal{P}^T + \mathcal{M})\mathbf{q}_2^{AE^*} = \mathcal{P}\left(-\mathbf{u}^{*E}_2 \cdot \nabla\mathbf{u}_2^A - \mathbf{u}_2^A \cdot \nabla\mathbf{u}^{*E}_2\right) \tag{C.22}$$
$$(2i\omega_f\mathcal{P}\mathcal{P}^T + \mathcal{M})\mathbf{q}_2^{E^2} = \mathcal{P}\left(-\mathbf{u}_2^E \cdot \nabla\mathbf{u}_2^E\right) \tag{C.23}$$

These are non-degenerate systems that may be readily inverted when the values 0, $i(\omega_c + \omega_f)$, $i(\omega_c + \omega_f)$ and $2i\omega_f$ do not belong to the eigenvalue spectrum. These conditions, together with the one obtained from (C.6), define the resonant cases.

C.1.3. Order $\sqrt{\varepsilon}^3$

The third-order equation is:

$$\partial_t\mathbf{u}_3+\mathbf{u}_0\cdot\nabla\mathbf{u}_3+\mathbf{u}_3\cdot\nabla\mathbf{u}_0+\nabla p_3-\mathrm{Re}_c^{-1}\nabla^2\mathbf{u}_3 = -\partial_{t_1}\mathbf{u}_1-\nabla^2\mathbf{u}_1-\mathbf{u}_1\cdot\nabla\mathbf{u}_2-\mathbf{u}_2\cdot\nabla\mathbf{u}_1 \tag{C.24}$$

Using (C.4) and (C.16), the forcing terms of the right-hand side can be written as

$$\begin{aligned}\left(\partial_t\mathcal{P}\mathcal{P}^T + \mathcal{M}\right)\mathbf{q}_3 = (e^{i\phi} + e^{-i\phi})e^{i\omega_c t}(\mathbf{G}\partial_{t_1} A_\pm + A\mathbf{F}_3^A + A_\pm|A_\pm|^2\mathbf{F}_3^{A|A|^2} +\\ A_\pm|E|^2\mathbf{F}_3^{A|E|^2} + c.c.) + \dots\end{aligned} \tag{C.25}$$

where

$$\begin{aligned}
\mathbf{G} &= \mathcal{P}\left(-\mathbf{u}_1^A\right) && \text{(C.26)}\\
\mathbf{F}_3^A &= \mathcal{P}\left(-\mathbf{u}_1^A \cdot \nabla \mathbf{u}_2^1 - \mathbf{u}_2^1 \cdot \nabla \mathbf{u}_1^A - \nabla^2 \mathbf{u}_1^A\right) && \text{(C.27)}\\
\mathbf{F}_3^{A|A|^2} &= \mathcal{P}\left(-\mathbf{u}_1^A \cdot \nabla \mathbf{u}_2^{|A|^2} - \mathbf{u}_2^{|A|^2} \cdot \nabla \mathbf{u}_1^A - \mathbf{u^*}_1^A \cdot \nabla \mathbf{u}_2^{A^2} - \mathbf{u}_2^{A^2} \cdot \nabla \mathbf{u^*}_1^A\right) && \text{(C.28)}\\
\mathbf{F}_3^{A|E|^2} &= \mathcal{P}(-\mathbf{u}_1^A \cdot \nabla \mathbf{u}_2^{EE^*} - \mathbf{u}_2^{EE^*} \cdot \nabla \mathbf{u}_1^A - \mathbf{u}_2^{AE} \cdot \nabla \mathbf{u^*}_1^E - \mathbf{u^*}_1^E \cdot \nabla \mathbf{u}_2^{AE}\\
&\quad -\mathbf{u}_1^E \cdot \nabla \mathbf{u}_2^{AE^*} - \mathbf{u}_2^{AE^*} \cdot \nabla \mathbf{u}_1^E) && \text{(C.29)}
\end{aligned}$$

Elimination of the secular terms yields the following equation governing the amplitude $A'_\pm = \sqrt{\varepsilon} A_\pm$ of the global mode:

$$\frac{dA_\pm}{dt} = (\alpha - \mu(\omega_f)E^2)A - \lambda A_\pm |A_\pm|^2 \tag{C.30}$$

C.2. Resonant case $\omega_f \approx 2\omega_c$

The scaling is $\omega_f = 2\omega_c + \Omega'$, $E' = \sqrt{\varepsilon}^2 E$, $\Omega' = \varepsilon\Omega$. At order $\sqrt{\varepsilon}^2$ the solution is sought in the form

$$\begin{aligned}
\mathbf{q} = \mathbf{q}_0 &+ \sqrt{\varepsilon}[A_\pm(e^{i\phi} + e^{-i\phi})e^{i\omega t}\mathbf{q}_1^A + c.c.]\\
&+ \sqrt{\varepsilon}^2[\delta \mathbf{q}_2^1 + |A_\pm|^2 \mathbf{q}_2^{|A|^2} + (A_\pm^2(e^{2i\phi} + e^{-2i\phi})e^{2i\omega_c t}\mathbf{q}_2^{A^2} + c.c.)] \qquad \text{(C.31)}\\
&+ \sqrt{\varepsilon}^2[E e^{2i\omega_f t}\mathbf{q}_2^E + c.c.]
\end{aligned}$$

where

$$\left(2i\omega_c \mathcal{P}\mathcal{P}^T + \mathcal{M}\right)\mathbf{q}_1^E = \mathcal{P}(\mathbf{f}_E) \tag{C.32}$$

The amplitude equation reads

$$\frac{dA_\pm}{dt} = (\alpha - i\Omega/2)A_\pm - \lambda A_\pm |A_\pm|^2 + \mu E A_\pm^* \tag{C.33}$$